DISSERTATION

NOVEL TECHNIQUES OF RF HIGH POWER MEASUREMENT

Submitted by

Ovidiu Daniel Stan

Department of Electrical and Computer Engineering

In partial fulfillment of the requirements

For the Degree of Doctor of Philosophy

Colorado State University

Fort Collins, Colorado

Spring 2007

ProQuest Information and Learning Company
300 North Zeeb Road
P.O. Box 1346
Ann Arbor, MI 48106-1346

COLORADO STATE UNIVERSITY

February 22, 2007

WE HEREBY RECOMMEND THAT THE DISSERTATION PREPARED UNDER OUR SUPERVISION BY OVIDIU DANIEL STAN ENTITLED NOVEL TECHNIQUES OF RF HIGH POWER MEASUREMENT BE ACCEPTED AS FULFILLING IN PART REQUIREMENTS FOR THE DEGREE OF DOCTOR OF PHILOSOPHY.

Committee on Graduate Work

Thomas Chen

Peter Young

Hiroshi Sakurai

Hiroshi Sakurai

Adviser George Collins

Department Head

ABSTRACT OF DISSERTATION

NOVEL TECHNIQUES OF RF HIGH POWER MEASUREMENT

RF diagnostic systems provide essential parameters for both statistical process control (SPC) and automated process control (APC) in plasma based semiconductor and flat panel processing driven at RF frequencies. To achieve repeatability and control of RF plasma processes such as plasma-enhanced chemical vapor deposition (PECVD) and plasma etching (PE) it has become necessary to accurately (<1 %) monitor and control the actual plasma impedance and RF power delivered to the plasma. This thesis is based on the design and test of novel RF power instrumentation that is accurate even with RF powers in the range of tens of kilowatts.

The trend in RF process is to go to two extremes: very high frequency (>200 MHz) and high power (>50 KW) (large area flat panels). Industry requirements are already 50kW at 13.56 MHz and up to 200 MHz in frequency. There are emerging applications reported at even higher frequency (915 MHz ISM band).

Today's state of the art instruments can measure RF power with 1% accuracy at its best; typical accuracy is around 3% and it is rapidly degrading with the increase in Voltage Standing Wave Ratio (VSWR) due to unmatched loads. My thesis research proved that by using a proper digital correction algorithm better then 1% RF measurement accuracy could be obtained. An improved power measurement technique for real impedance lines and loads is presented along with test results at powers up to 3kW. For the case of RF power measurements into complex impedances I tested an entirely novel direct digital sampling method that is frequency agile.

Finally I contributed to the art of RF calorimeters as well as more accurate RF measurements. Absolute accuracy of the RF metrology is compounded by errors introduced primarily from the measurement system, the chosen calibration method and power references. RF high power standards are not traceable directly to primary metrology references provided by NIST. In order to improve the calibration accuracy of the instruments, I researched novel calibration techniques and determined the errors involved in the RF high power calibration methods.

Ovidiu Daniel Stan
Department of Electrical and Computer Engineering
Colorado State University
Fort Collins, CO 80523
Spring 2007

Acknowledgements

My family and friends supported and motivated me during my graduation studies at Colorado State University.

George Collins, my advisor, kept me going and guided me along.

I would like to thank Advanced Energy for the chance to work in such an exciting environment, for the technical support and generosity. Troy Mai believed in me and gave me the opportunity to be more than an engineer. Don Van Zyl and Victor Brouk were real technical role models for me. David Christie kept me focused on my goal and showed me that becoming a PhD is more than the research.

Many thanks to all the people I was in contact with (for technical support or just for philosophical discussions) for their understanding and patience; you made me better.

Dedication

I dedicate this work to my Mother, Victoria, for the “perseverance gene” and to my Father, Ion, for the love of engineering.

TABLE OF CONTENTS

CHAPTER 1

INTRODUCTION

1.1 History and Background

Radio frequency (RF) technology has been around since the beginnings of early broadcast communication. In fact, the use of RF in the first half of the 20th century centered on radio communication, as the very name implies. Electronic engineers and physicists began using RF power in semiconductor and thin-film processes in the early 1970's.

RF has assumed a dominant role in the plasma market in the 1990s with elaborate component configurations used in critical high-density CVD and PECVD deposition, etch, and PVD processes for applications including semiconductor manufacture, IC fabrication, thin-film heads for disks, CDs, hard disk coatings, and other industrial uses.

The increasing requirements for semiconductor and flat panel industry are pushing the limits of accuracy for RF power delivery. A repeatable process is a must when high yield is required.

Typical RF measurement system accuracy was for many years at 3% into a real impedance load (a load matched to the generator which is most often 50Ω). Data was reported at the output of the RF power supply (see Fig.1.1) while other system components – like an impedance match - were altering the RF before reaching the chamber.

Fig.1.1 illustrates the block diagram for an RF plasma system.

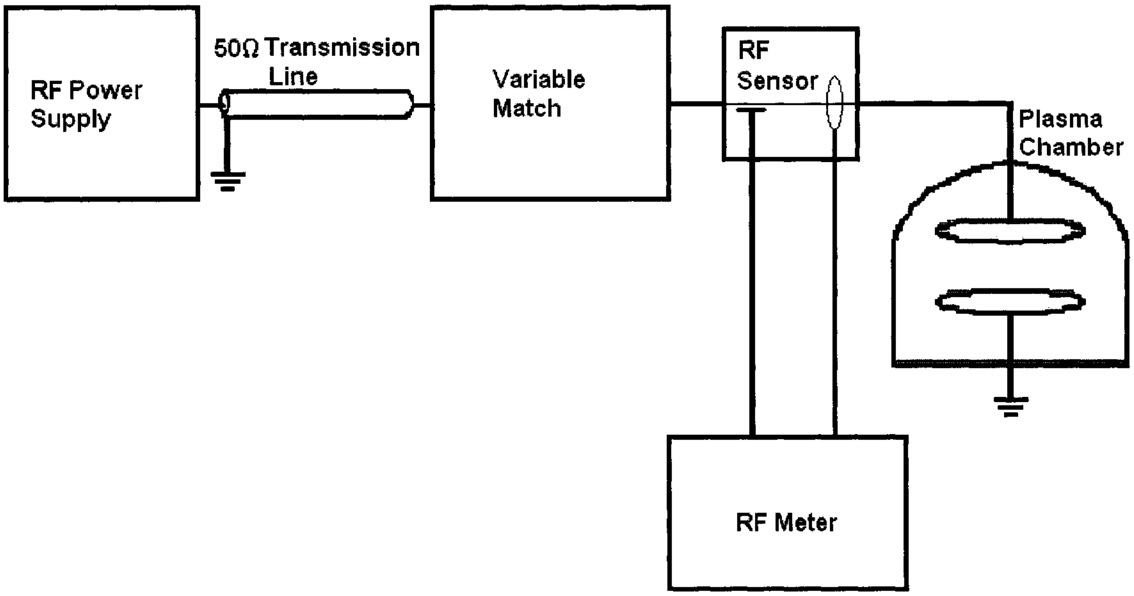

Fig. 1.1 RF Plasma delivery system – General schematic

The RF diagnostic for what is happening in the plasma chamber processes was rudimentary and in many cases was simply measuring the DC bias voltage level and RF peak voltage. There was no information related to the power transferred to the chamber or what kind of plasma mode transitions takes place during the process as you change gas mixes and chamber pressures. Keep in mind that RF powers were often below the kW level. As wafer and flat panel dimensions have increased the RF power levels are now in the tens of kilowatts and thermal drifts are an increasing barrier to accurate measurement.

The setup of the plasma chamber requires measurement of the impedance before and after striking plasma. Any changes in plasma impedance will result in changes in the process[1, 2].

In high power RF instrumentation, the needs were outlined by Sematech[3] and the quest began for creating a standard RF metrology device that would require minimum calibration. My thesis research proved that is not practical to create such an ideal device because of the electrical and thermal imperfection of the components. I judge that a better solution is to work toward correcting these imperfections using software as described and detailed herein. Moreover, the progress made in high-speed high bit micro controllers and digital signal processors allows fast signal processing and enables new approaches as well as on line correction of the RF measurements.

Another dimension of the problem is the state of RF calibration sources and RF references[4-18]. Most of the RF calibration efforts are done at microwave frequency[19-35] and at mW level[36-50]. Some of the methods can be extrapolated down in frequency to 1-50 MHz, but the high power levels (hundreds to thousands of Watts) introduce element variations and heat induced changes to all RF components.

The actual trend[51-53] in RF instrumentation process is to go to high Frequency and high power (large area flat panels) encounters the problem of no traceable RF high power standard. Rather all the RF references are only traceable to DC current and DC volt standards. Moreover, all the calibration methods introduce an uncertainty factor into the accuracy of the RF instrument. In addition, the three most reliable means of calibration I researched had significant errors involved; therefore in my thesis I present also new high power RF calibration methods.

1.2 References

[1] Lensing, K., Singh, B., Cain, J. and Purdy, M., Beyond the Algorithms: Better Process Control Through Advanced Measurement Technology, AEC/APC XVII Symp., (Sept. 26 - 28, 2005).
[2] Kamlet, L., Tongol, M. and Gunn, J., Improved Predictive Endpoint of Etch and Clean Processes, AEC/APC XVII Symp., (Sept. 26-28, 2005).
[3] Jeanne Cranford & team, Sematech, Radio Frequency (RF) Measurement and Control Project Report (TECQ001) (September 10, 1998).
[4] Fantom, A. E., Power and energy: National standards, Proceedings of the IEEE Volume 74, Issue 1, 94 – 101, (Jan. 1986).
[5] Larsen, N. T., IEEE Trans. on Instrum. and Meas., v. IM-25, No. 4, 343-347 (1976).
[6] Larsen, N. T., Rev. Science Instrum., v.39, No. 1,1-12 (1968).
[7] Harvey, M. E., Rev. Science Instrum., v. 39, No. 1, 13-18 (1968).
[8] Engen, G. F., J. Nat. Bureau of Standards-C, v. 63C, No. 1, p. 77-82 (1959).
[9] Ginley, R. A., A Direct Comparison System for Measuring Low Frequency Power (100 KHz to 18 GHz), (March 01, 2006).
[10] Clague, F. R., Voris, P. G., Coaxial Reference Standard for Microwave Power, NIST Technical Note 1357, (April 1993).
[11] Clague, F. R., Microcalorimeter for 7 mm Coaxial Transmission Line, NIST Technical Note 1358, (August 1993).
[12] Clague, F. R., A Calibration Service for Coaxial Reference Standards for Microwave Power, NIST Technical Note 1374, (May 1995).
[13] Brady, M. M., Correction to In-line waveguide calorimeter for high-power measurement – accounting for transverse waveguide wall currents, IEEE Trans. Microwave Theory Tech. MTT-11: 152, (March, 1963).
[14] Taylor, B. N., Kuyatt, C. E., Guidelines for evaluating and expressing the uncertainty of NIST measurement results, Nat. Bur. Stand. (U.S.) Tech. Note 1297 (1994 edition), (September 1994).

[15] Remley, K. A., Williams, D. F., Analytic Sampling-Circuit Model, IEEE Transactions on Microwave Theory and Techniques, (June 01, 2001).
[16] Engen, G. F., A bolometer mount efficiency measurement technique, J.Res. Nat. Bur. Stand. (U.S.) 65C(2): 113-124, (April-June, 1961).
[17] Larsen, N. T., 50 microedge temperature controller, Rev. Science Instrum. 39(1), 1-12, (January, 1968).
[18] Harvey, M. E., Precision temperature-controlled water bath, Rev. Science Instrum. 39(1), 13-18, (January, 1968).
[19] Clark, R. F, The microcalorimeter as a national microwave power standard, Proceedings of the IEEE Volume 74, Issue 1, 102 – 104, (Jan. 1986).
[20] Allen, J. W., Clague, F. R., Larsen, N. T., and Weidman, M. P., NIST Microwave Power Standards in Waveguide, NIST Technical Note 1511 (1999).
[21] Clague, F. R., A Calibration Service for Coaxial Reference Standards for Microwave Power, NIST Technical Note 1374 (1995).
[22] Clement, T. S. Hale, P. D., Williams, D., Calibrated 200 GHz Waveform Measurement, IEEE Photonics Technology Letters, (April 01, 2005).
[23] Myslinski, M., Nauwelaers, B. Schreurs, D. Remley, K. A., Wideband Large Signal RF Measurements Applied to Behavioral Model Extraction
European Microwave Conference, Manchester, England, (September 10-15, 2006).
[24] Cox, A. Janezic, M. D., Preliminary Studies of Electromagnetic Properties of Microwave Absorbing Materials used in Calibration Targets, IEEE Geoscience and Remote Sensing Symposium, (July 31-August 3).
[25] Yates, B. C., Counas, G. J., Summary of WR15 Flange Evaluation at 60 GHz, Nat. Bur. Stand. (U.S.) Tech. Note 642, (October, 1973).
[26] Fantom, A., Radio Frequency and Microwave Power Measurement, IEE Electrical Measurement Series 7, Peter Peregrinus Ltd., (1990).
[27] Larsen, N. T., Weidman, M. P., Allen, J. W., Clague, NIST Microwave Power Standards in Waveguide, NIST Technical Note (TN 1511), (February 01, 1999)
Conn, T., Muth, L. A., Phase-Dependent RCS Measurements, AMTA Digest, (November 4-8, 2002).
[28] IEEE Electromagnetic Compatibility Symposium, (September 01, 2002).
[29] Williams, D. F., Alpert, B. K., Characteristic Impedance, Causality, and Microwave Circuit Theory, IEEE Workshop on Signal Propagation on Interconnects, (May 19-21, 1999).
[30] Clague, F. R., A calibration service for coaxial reference standards for microwave power, Natl. Inst. Stand. Technology, Tech. Note 1347, (May, 1995).
[31] Maury, M. A., Simpson, G. R., Improved millimeter waveguide flanges improve components and measurements, Microwave J. 29(5): 337-346, (May, 1986).
[32] Crawford, M. L., Koepke, G. H., Design, evaluation, and use of a reverberation chamber for performing electromagnetic susceptibility/vulnerability measurements. Nat. Bur. Stand. (U.S.) Tech. Note 1092, (April, 1986).
[33] Clague, F. R., Voris, P. G., Coaxial reference standards for microwave power, Nat. Bur. Stand. (U.S.) Tech. Note 1357, (April, 1993).
[34] Brady, M. M., In-line waveguide calorimeter for high-power measurement, IRE
[35] Trans. Microwave Theory Tech. MTT-10: 356-359, (September, 1962).

[36] NPL Measurement Services, http://www.npl.co.uk/measurement_services/

[37] Akhiezer, A. N. Senko, A. P., Seredniy, V. P., Power standards in millimeter range, Conference on Precision Electromagnetics Measurements Digest, 378-379, (June 1996).

[38] Marks, R. B., IEEE Standardization for the Wireless Engineer, IEEE International Microwave Symposium Digest, (June 01, 2001).

[39] Gupta, K. C., Cidronali, A., DeGroot, D. C., Jargon, J. A., Expanding Definitions of Gain by Taking Harmonic Content into Account, International Journal of RF and Microwave Computer-Aided Engineering, (September 01, 2003).

[40] Juroshek, J. R., NIST 0.05-50 GHz Direct-Comparison Power Calibration System, CPEM Conference Digest, May 14-19, 2000, Sydney, Australia, (May 01, 2000).

[41] Johnk, R. T., Novotny, D., Ondrejka, A., Weil, C. M., Calibration of Broadband RF Field Probes Using a Coaxial conical Transmission Line, International Conference on Microwaves, Radar and Wireless Communications, (May 20-22, 2002).

[42] Lyons, R., Metrology for Radio Frequency Technology: A Bibliography of NIST Publications (NISTIR 5075).

[43] Clague, F. R., Crowley, T. P., A 2.4 mm Coaxial Power Standard at NIST British Electromagnetics Conference, (November 6-8, 2001).

Hoer, Cletus A., Engen, Glenn F., Vector voltmeter, US Pat. No. 4,001,681, (January 4, 1977).

[44] Adamian, Vahe A., Falcinelli, Michael T., Phillips, Peter V., Electronic microwave calibration device, US Pat. No. 5,434,511, (July 18, 1995).

[45] Adamian, Vahe A., Falcinelli, Michael T., Phillips, Peter V., Calibration method and apparatus, US Pat. No. 5,467,021, (November 14, 1995).

[46] Taub et al, Cryogenic Probe Station for use in Automated Microwave and Noise Figure Measurements, NASA Technical Memorandum 106560, 1-9, (May 1994).

[47] Mejia et al, A Single-Block TRL Test Fixture for the Cryogenic Characterization of Planar Microwave Components, Advances in Cryogenic Engineering, vol. 41, , 1731-1738, (1996).

[48] Smuk et al, S-Parameter Characterization and Modeling of Three-Terminal Semiconductive Devices at Cryogenic Temperatures, IEEE Microwave and Guided Wave Letters, vol. 2, No. 3, 111-113, (Mar. 1992).

[49] Gronau, Scattering-Parameter Measurement of Microstrip Devices, Microwave Journal, 82, 84, 86 and 89-92, (Nov. 1992).

[50] van Zyl et al, A Simplified Calibration Procedure for Cryogenic Microwave Measurements, IEEE MTT-S Digest, 1403-1406, (1996).

[51] de Vreede, J. P. M., Korfage, W., Persson, P., Brunetti, L., Lopez, V., Petras, I., Morard, P., Hejsek, F., Torok, A., Ruhaak, J., Ascroft, J., DressLer, E., Celep, M., Lapuh, R., Achkar, J., International comparison for RF power in the frequency range up to 18 GHz, Transactions on Instrumentation and Measurement, Volume 50, Issue 2, 409 – 413, (April 2001).

[52] Donley, E. A., Crowley, T. P., Juroshek, J. R., Riddle, B. F., Heavner, T. P., Development of a Quantum Based Microwave Power Measurement

[53] IEEE International Microwave Symposium Digest, (June 8-13, 2003). Crowley, T., Microwave Power Measurements, NIST/ARFTG Short Course on Microwave Measurements and Instrumentation, (Nov. 29, 2005).

CHAPTER 2

RF Measurement Building Blocks

2.1 Background

The block diagram of an RF instrument has changed very little since its inception in the early radio arena. Measurements of the forward and reflected power from antennas were enough to characterize the RF emission level and efficiency of the RF amplifier stage, quantifying how adapted or matched it is to the chosen antenna.

The advantages of RF plasma applications pushed the RF instrumentation requirements toward more accurate power and impedance measurements in an arena with very non-linear loads and very high standing wave ratios that vary with time. While impedance measurements at low power can be done with off the shelf instruments[1, 2] (Agilent, Yokogawa), characterization of plasma impedance under tens of kilowatts RF Power is far more difficult.

Technological progress made the blocks of the RF instrumentation more accurate, smaller and intelligent, as I will discuss herein. With the increase in chip processing power, new pathways in mathematical processing of measurements are open, which correct for non-ideal effects real time.

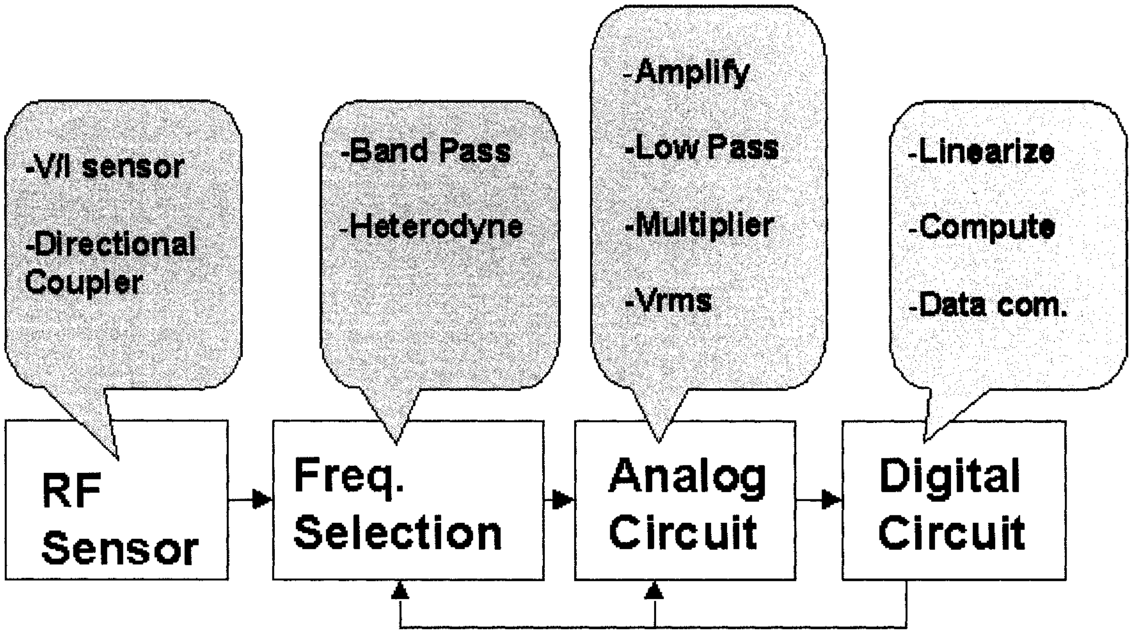

Fig. 2.1 Anatomy of an RF Measurement System –General Schematic

Fig. 2.1 contains the schematic block of a traditional RF Measurement System. Its main components are:

- **The RF Sensor** has to accurately sample the applied fundamental RF frequency signal. The generated sensor signal must be proportional in every aspect with: voltage amplitude, current amplitude and the phase between current and voltage. The role of harmonics should then be considered

- **The frequency selection circuit** function is to segregate the sensor signal that we are interested in from the high level RF signals. During RF processing, the plasma chamber has complex, non-linear impedance, generating a lot of harmonic signals. In addition many processes employ two of more RF signals at different frequencies. Hence a frequency agile sensor is sought to measure the strength of a variety of generated signals. Nevertheless the RF behavior of the plasma chamber today, in practice, is still characterized by analyzing the main frequency signal alone.

- **The analog circuit that interfaces with the RF sensor** is used to do the signal conditioning (auto-gain control or scaling) or to calculate the actual power via an analog multiplier, or a RF diode rectifier characteristic as presented herein. Early designs were analog only and achieved 3% accuracy on power measurement into 50Ω and around 5% accuracy on selected mismatched impedances (other than 50Ω). I will show herein how modern digital devices allow for real time correction of power measurements to achieve accuracy well below 1 %.

- **The digital circuit** can perform all the necessary calibration through lookup tables, power triangle and impedance calculations and corrections, data communication, user interface, data display. Finally, my thesis shows to what extent I have been successful to replace the traditional analog electronics interfaces by novel digital mixers, digital filters and digital correction algorithms.

Above I summarized the block diagram for the RF power measurement system from a traditional mixed analog and digital point of view. To properly understand the source of measurement errors in the traditional RF measurement systems, I analyzed all the components as outlined below and determined the necessary corrections for the new digital correction via lookup tables.

2.2 V/I Sensor

V/I (voltage/current) sensor pairs are still widely used for low frequency applications (KHz-MHz range). The advantage of the V/I sensor is low loss, especially at high RF currents; therefore is the main choice for applications in which the load is low impedance. In the high frequency region above 3 MHz the RF V/I (Voltage/Current) sensor pair is, at first glance, the easiest technique used to measure RF power. Fig. 2.2 illustrates four transformer coupled V/I probes that attempt to isolate the power path from the measurement path. Briefly, the main advantages of the RF V/I sensor are:

- Less expensive then a strip-line design. The V/I sensor can be designed with off the shelf components, no custom parts required.

- Smaller size at low frequencies. As a rule of thumb the strip-line sensors size is proportional to the wavelength. Below frequencies of 1MHz the size of a strip-line RF sensor is impractical, it is over 4 inch long.
- Higher current capability then a strip-line. A deposited strip-line RF sensor would require a large size central strip to handle large currents. However, there are air directional couplers designs that can handle high currents.
- Very good isolation between the main line and measurement block.

There are a lot of design efforts[3-11] geared towards the ideal V/I sensor that does not need correction or calibration, but as I will prove later, for the case of high power RF sensors there is a set of required correction factors that must be accounted for to compensate for known and measurable errors.

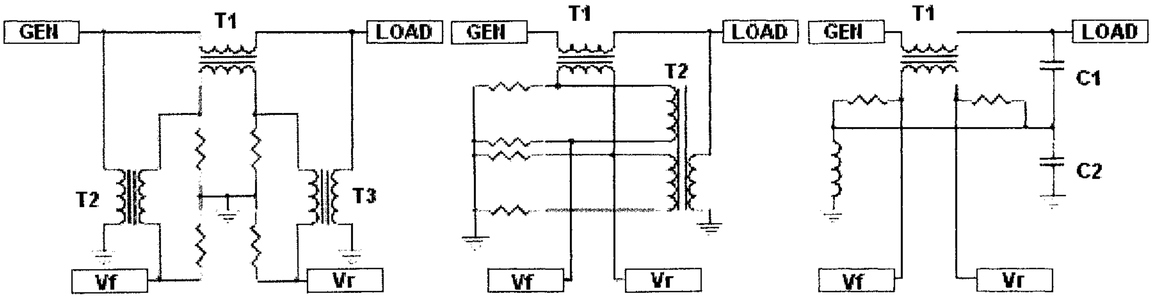

Fig. 2.2 Examples of V/I Sensor Topologies

The RF current transformer (T1 in Fig 2.2) is often a 1: N type while the voltage sensor is either a N_1/N_2 transformer[6] (T2 and T3 in Fig. 2.2) that also employs a capacitive voltage divider[7] (C1/C2 in Fig. 2.2).

In both cases magnetic core coupling requires use of magnetic materials that bring frequency, temperature and signal amplitude and saturation limitations. Fortunately, as I will show below all these effects can be parsed, quantified and accounted for in the linear operating region.

The mathematical equations behind the RF V/I sensor are discussed below.

2.2.1 Transmission Line Based V/I Sensor Analysis

From directional coupled based transmission line sensors and transmission line equations one is able to measure both V_f, the forward voltage wave amplitude and V_r, the reflected voltage wave amplitude and thereby derive expressions for P_f, the forward RF power and P_r, the reflected power as well as all elements of the power and impedance triangles.

The current on the transmission line[12-16] measured by a sensor placed at the unmatched load depends on the forward voltage, reflected voltage and the line impedance as summarized by the mathematical relations below.

$$I = \frac{V_f - V_r}{Z_0} \tag{2.1}$$

$$V = V_f + V_r \tag{2.2}$$

$$Z_0 = \frac{V}{I} \tag{2.3}$$

The equations governing the V/I sensor are:

$$V_f = \frac{V + Z_0 * I}{2} \qquad (2.4)$$

$$P_f = \frac{|V_f|^2}{Z_0} \qquad (2.5)$$

$$V_r = \frac{V - Z_0 * I}{2} \qquad (2.6)$$

$$P_r = \frac{|V_r|^2}{Z_0} \qquad (2.7)$$

As it shown in Fig. 2.2 the measurement of both the forward voltage V_f and reflected voltage V_r is done by analog circuits often transformer isolated. There are several variations of these circuits involving operational amplifiers as a sum, difference or phase shift.

$$P_{load} = \left[\frac{|V_f|^2}{Z_0} - \frac{|V_r|^2}{Z_0} \right] \qquad (2.8)$$

$$P_{load} = V * I = |V||I| \cos\theta \qquad (2.9)$$

If more than basic signals are required, then more complex mathematical functions have to be implemented:

$$R = Z_0 \cos\theta \qquad (2.10)$$

$$X = Z_0 \sin\theta \qquad (2.11)$$

Sampling a tens kilowatt power level RF voltage or current accurately is not trivial due to RF component imperfections as well as parasitic elements. Most resistors and capacitors have parasitic impedances associated with them, as well as voltage and power limits. Smaller components have less parasitic impedance, but also have power and voltage limitations.

The basic topologies for RF voltage dividers[7] are analyzed below, neglecting high power effects to illustrate basic concepts.

An ideal case would be if the voltage divider was made only from ideal lumped parameter capacitive impedances with no parasitic elements varying versus frequency (Fig. 2.3).The voltage division is scaled to match detection electronics input voltage and impedance levels.

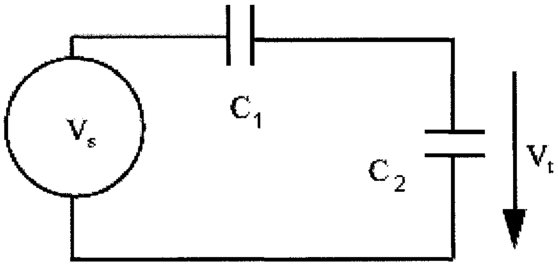

Fig. 2.3 Schematic Illustration of Ideal Capacitive Voltage Sensor

$$V_t = \frac{V_s \dfrac{1}{j\omega C_2}}{\dfrac{1}{j\omega C_1} + \dfrac{1}{j\omega C_2}} \tag{2.12}$$

$$V_t = V_s \frac{C_1}{C_1 + C_2} \tag{2.13}$$

In the case of the cap divider (Fig. 2.3) the output sensor signal is in phase with the input. The amplitude of the output signal depends only on the values of the frequency matched capacitor pairs (output is not dependent on the frequency). This is an ideal case and due to imperfections in the components it has only academic and introductory value.

The R-C configuration (Fig 2.4) avoids the need for a high impedance amplifier after the voltage divide because we can choose R small compared to the amplifier input impedance.

The voltage sensing arrangement then became a C-R differentiator circuit (Fig 2.4) where V_s is the voltage being sensed.

$$V_t = \frac{V_s R}{R + \frac{1}{j\omega C}} = V_s \frac{j\omega RC}{1 + j\omega RC} \tag{2.14}$$

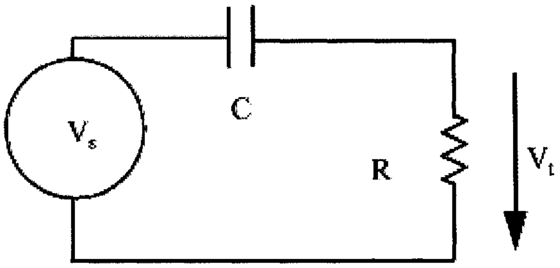

Fig. 2.4 **Schematic Illustration of Differentiator Voltage Sensor**

$$\|V_t\| = \frac{\omega}{\omega_0} \frac{\|V_s\|}{\sqrt{1 + \left(\frac{\omega}{\omega_0}\right)^2}} \tag{2.15}$$

Where we define:

$$\omega_0 = \frac{1}{RC} \tag{2.16}$$

To match RF cables R=50Ω and C is in the range of pF. This is placing f_0 in the range of 1GHz. The phase angle of the output is then:

$$V_t phase = \tan^{-1}\left(\frac{\omega_0}{\omega}\right) \tag{2.17}$$

If $\frac{1}{\omega c} >> R$ then we can simplify the expression 2.17 to:

$$V_t = j\omega RCV_s \tag{2.18}$$

but this is a large approximation for our purposes. The observation is that at frequencies below f_0 the amplitude and phase depends also on the applied signal frequency, f.

$$V_t = K_v V_s f \sin(\tan^{-1}\left(\frac{\omega_0}{\omega}\right)) \tag{2.19}$$

K_v is a constant depending on the load. This derivative configuration of the voltage divider is of interest because the transfer function is similar with the one from the current sensor, therefore phase and frequency correction are easy to implement.

The ideal RF voltage divider contains only a capacitor divider but real applications require further processing (like gain scaling or signal filtering) that involves a R-C load (Fig. 2.5).

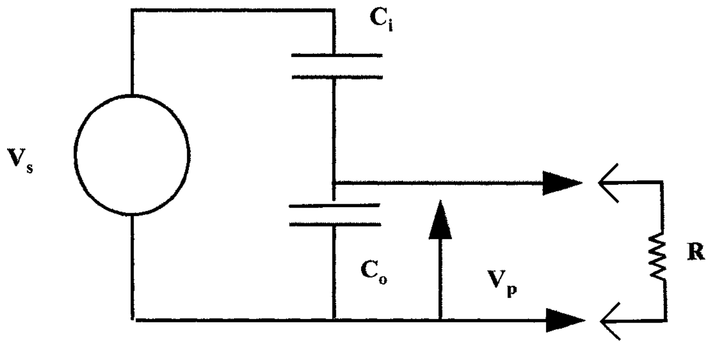

Fig. 2.5 **Real Capacitor Divider has a Resistive Load**

The real case of the RC load capacitive voltage divider is represented in Fig. 2.6.

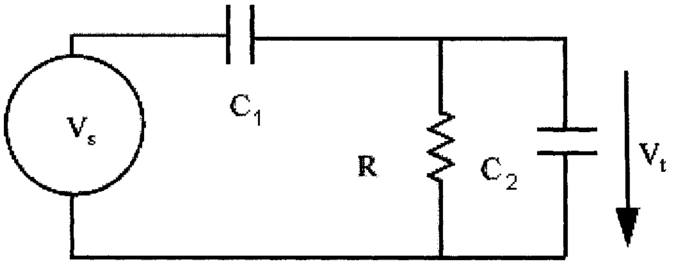

Fig. 2.6 **Schematic Illustration of Voltage Sensor**

$$V_t = \frac{V_s \dfrac{1}{j\omega c_2} \| R}{\dfrac{1}{j\omega c_1} + \dfrac{1}{j\omega c_2} \| R} = \frac{V_s \dfrac{R}{1 + j\omega R c_2}}{\dfrac{1}{j\omega c_1} + \dfrac{R}{1 + j\omega R c_2}} \tag{2.20}$$

$$V_t = V_s \frac{j\omega R c_1}{1 + j\omega R (c_1 + c_2)} \tag{2.21}$$

I define ω_0 as in expression 2.22, for $C_2 >> C_1$:

$$\omega_0 = \frac{1}{R(c_1 + c_2)} \approx \frac{1}{R c_2} \tag{2.22}$$

The approximation for ω_0 works because $C_1 << C_2$. The term ω_1 is defined as:

$$\omega_1 = \frac{1}{Rc_1} \tag{2.23}$$

Substituting the expressions for ω_0 and ω_1 in the 2.21 formula the output voltage V_t will be simply expressed as:

$$V_t = V_s \frac{j\frac{\omega}{\omega_1}}{1 + j\frac{\omega}{\omega_0}} \tag{2.24}$$

Using some algebraic manipulation[17] of the terms (multiplying with the complex conjugate) we can obtain the expressions for the amplitude and phase of V_t.

$$V_t = V_s \frac{\frac{\omega}{\omega_1}(\frac{\omega}{\omega_0} + j)}{1 + \left(\frac{\omega}{\omega_0}\right)^2} \tag{2.25}$$

$$\|V_t\| = \|V_s\| \frac{\frac{\omega}{\omega_1}\sqrt{1 + \left(\frac{\omega}{\omega_0}\right)^2}}{1 + \left(\frac{\omega}{\omega_0}\right)^2} \tag{2.26}$$

Expression 2.27 is the amplitude of the output voltage for the more practical R-C load capacitive divider circuit of Fig. 2.6:

$$\|V_t\| = \|V_s\| \frac{\omega}{\omega_1} \frac{1}{\sqrt{1 + \left(\frac{\omega}{\omega_0}\right)^2}} \tag{2.27}$$

Note however that the phase of the circuit from Fig. 2.6 sensor signal is going to vary according to expression 2.28:

$$V_t\,phase = \tan^{-1}\left(\frac{\omega_0}{\omega}\right) \tag{2.28}$$

Current sensors relay on Faraday's law[18] that states that the electromotive force (EMF) (voltage) induced in a conducting loop is the negative of the time derivative of the magnetic flux enclosed by the loop. The signal level is set by the RF current being measured and by the designed geometry of the sense loop.

$$emf = \frac{-d\phi}{dt} \tag{2.29}$$

This approach is typically used at low frequencies by employing an high permeability iron core to totally capture the flux and routing it through a remote sense winding having multiple turns so the flux is linked enough times to provide a usable voltage. The same approach has also been used in RF current sensors using high frequency ferrite toroids. However, varying core losses versus frequency and core non-linearities, as well as high winding inductance and distributed capacitance, obfuscates a direct first principle link to the sensed voltage of the RF current being sensed. The changes in the magnetic flux are due to variations in the magnetic field[19]. The magnetic field is also determined by changes in the RF current.

$$emf = K\frac{dI}{dt} \tag{2.30}$$

The important conclusion is that the current sensor is reporting the derivative of the current. Coefficient K is a coupling coefficient.

The presence of a core also adds inductance to the conductor carrying the current making the sensor obtrusive. There are several designs that are using a one loop current sensor; a good example is in Fig. 2.7.

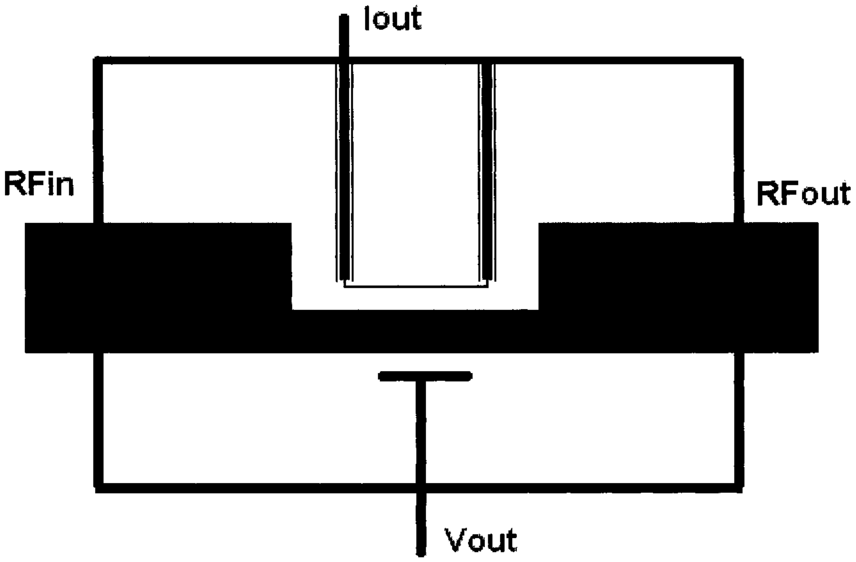

Fig. 2.7 **Cross Section of V/I Sensor to Show Current Pickup Loop and Voltage Pickup Probe Placement**

The RF current pickup loop is also subject to inadvertent capacitive coupling to the inner conductor if proper shielding is not employed. This problem is mitigated by using a coaxial pickup loop so that the outer conductor of the pickup loop is grounded to the outer conductor of the power carrying coax at both ends. A small cut in the pickup loop's shield shown in the center of Fig. 2.7 allows it to act as a Faraday shield, effectively keeping the electric field from reaching the center conductor of the pickup loop while allowing the magnetic field, which is only proportional to the current, to be completely linked. The split in the pickup coaxial outer conductor prevents the flow of inductively driven current in the shield so that the magnetic flux is not excluded from the center conductor of the loop. For applications using ferrite transformers as current sensors, to reduce the capacitive coupling, the portion of the RF line (one turn "primary winding") is shielded.

Furthermore, subtle considerations about magnetic coupling are discussed in the strip line directional coupler section 2.3, below, where advantages and disadvantages of different geometries are outlined. Quantitative analysis is discussed in section 2.4.

2.3 Strip-line Based Directional Coupler

When two transmission lines [20-22] are spatially designed to be physically close together power can be coupled between the lines due to the interaction of the electromagnetic fields from each line. Those coupled lines are used to distinguish RF power flow in the forward direction (from generator to load) as compared to reflected direction (from the load towards the generator). Generally, microstrip (Fig. 2.8) and stripline forms are used[23] in designing the directional couplers.

The typical RF applications are using the directional coupler to sample Vf – forward voltage and Vr –reflected voltage from the main RF line. The design of the directional coupler[24-30] is not trivial; it requires computer aided finite element analysis and is beyond the purpose of this dissertation. Nevertheless, the basics can be found in the literature[31-33].

The use of flat printed circuits strip-lines at microwave frequencies was first reported by Barrett & Barnes[34] in 1951. One of the contractors was Airborne Instruments Laboratory, where researchers developed a printed line on a thin dielectric support suspended between two plates using air as the dielectric. They called it Stripline and registered that name as a trademark. Since then a lot of research and progress was done regarding RF hybrids, splitters and dividers [35-45].

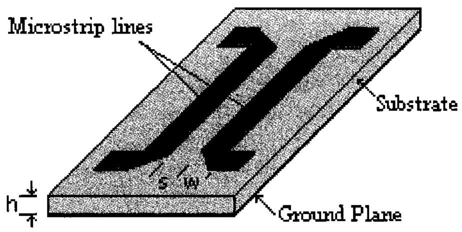

Fig. 2.8 **Schematic Illustration of a Directional Coupler**

As a general rule, the size of the directional coupler is proportional to the wavelength of the RF signal; therefore below a certain frequency the size of the directional coupler would be too large. Because of physical limitations the use of a compact directional coupler is practical only for frequencies above 1MHz. Directional couplers are also characterized by the available bandwidth, coupling factor, RF insertion loss (which is critical at high RF power levels) and directivity (or isolation of RF forward waves from RF reflected waves). The bandwidth is relatively large and is affected by non-linearities at both frequency ends;

therefore in practice a directional coupler is “optimized” for a specific frequency range by the use of additional reactive elements.

The RF coupling coefficient is a measure of the signal amplitude on the output port as compared to the input port in dB units.

$$CouplingFactor = -10 * \log \frac{P_{out}}{P_{in}} (dB) \tag{2.31}$$

The coupling factor is not constant, but varies with applied RF frequency; hence, a perfectly flat frequency response coupler cannot be built. Therefore directional couplers are specified in terms of the coupling accuracy at the frequency band center.

In an ideal directional coupler the RF insertion loss is mainly due to power coupled and it is expressed in dB:

$$InsertionLoss = -10 * \log(1 - \frac{P_{out}}{P_{in}})(dB) \tag{2.32}$$

Again, due to the presence of tens of kilowatts of RF power flow, insertion loss can create thermal issues.

Coupling dB	Insertion Loss - dB
3	3.00
6	1.25
10	0.458
20	0.0436
30	0.00435

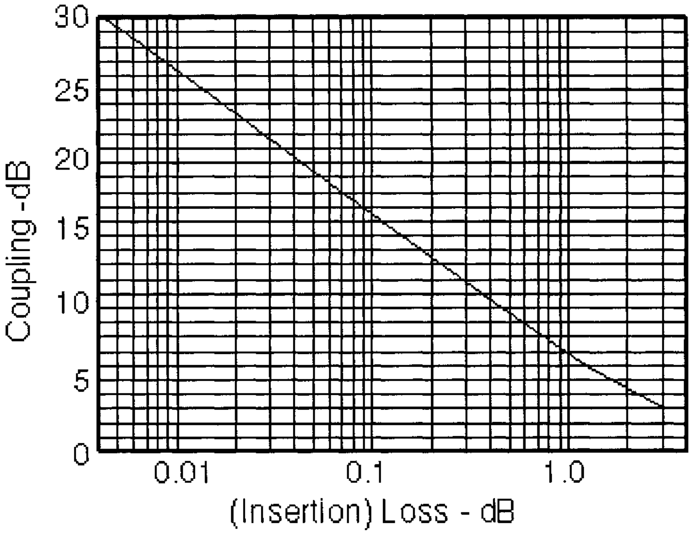

Fig. 2.9 **Directional Coupler Insertion Loss vs. Coupling Factor**

The directivity of the directional coupler is defined as the ratio between the forward and reflected channel outputs when connected to an adapted load, expressed in dB.

$$Directivity = 10 * \log \frac{P_{FWD}}{P_{RFL}} (dB) \qquad (2.33)$$

The directivity should be as high as possible. Four typical examples of directional coupler topologies are in Fig 2.10.

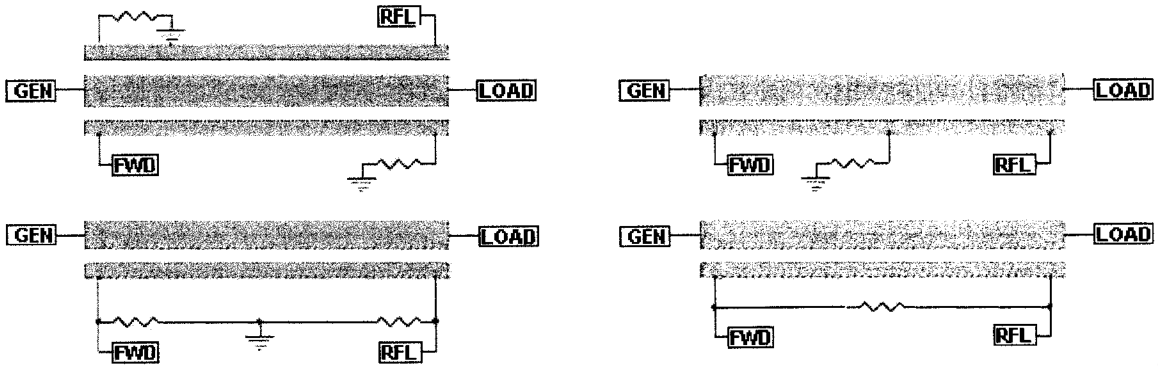

Fig. 2.10 **Common Topologies for the Microstrip Directional Couplers**

From the application and geometry point of view there are no differences in the topologies from Fig. 2.10; all of them are providing the same output signals V_f and V_r. Geometrically, the example that is using 3 strip-lines (instead of two); will have an advantage regarding the isolation between the forward and reflected voltage signals.

In summary the qualitative advantages of the directional coupler (as an RF sensor) are: simplicity, repeatability and stability in time. Some of the disadvantages are the fact that is a custom device and that the output varies with applied frequencies and has bandwidth limitations. Many applications involve two closely spaced RF frequencies driving the same load so bandwidth can be crucial to limiting accurate measurement for two frequencies operation. The heterodyne approach discussed later eliminates these issues. If the directional coupler is build in the micro-strip technique it is worth mentioning that there are also limitations regarding the current capacity of the main strip (difficult to use at high currents).

2.3.1 Directional Coupler RF Sensor Quantitative Analysis

Next, I am going to restrict the size of the directional coupler to be much smaller than the wavelength of the RF signal to be measured, therefore the voltage and current spatial distributions along the directional coupler does not change over the length of the strip-line. Keep in mind that while the forward and reflected voltage waveforms are positive standing waves, the RF currents are 180 degrees out of phase and will induce voltages in magnetic loops that are opposite in sign, to distinguish forward from reflected currents.

Total output voltages (V_f and V_r) are the sum of capacitive and inductive terms. The electrical induced voltage is due to capacitive coupling (Fig. 2.11) so that allowable parasitic capacitance is below several pF.

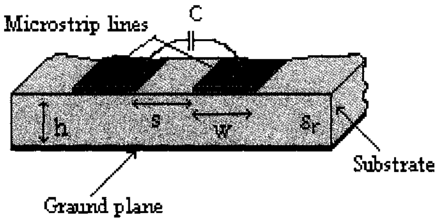

Fig. 2.11 Capacitive Coupling Between Coupled Strip-lines

The central strip-line (main RF line) in which RF current flows develops a RF magnetic field that is in turn inducing an EMF into the forward and reflected current loops. The forward and reflected magnetic/current loops, shown in red in Fig 2.12, are separated from each other by the strip-lines unique grounding paths plus the walls of the directional coupler shown in blue in Fig. 2.12.

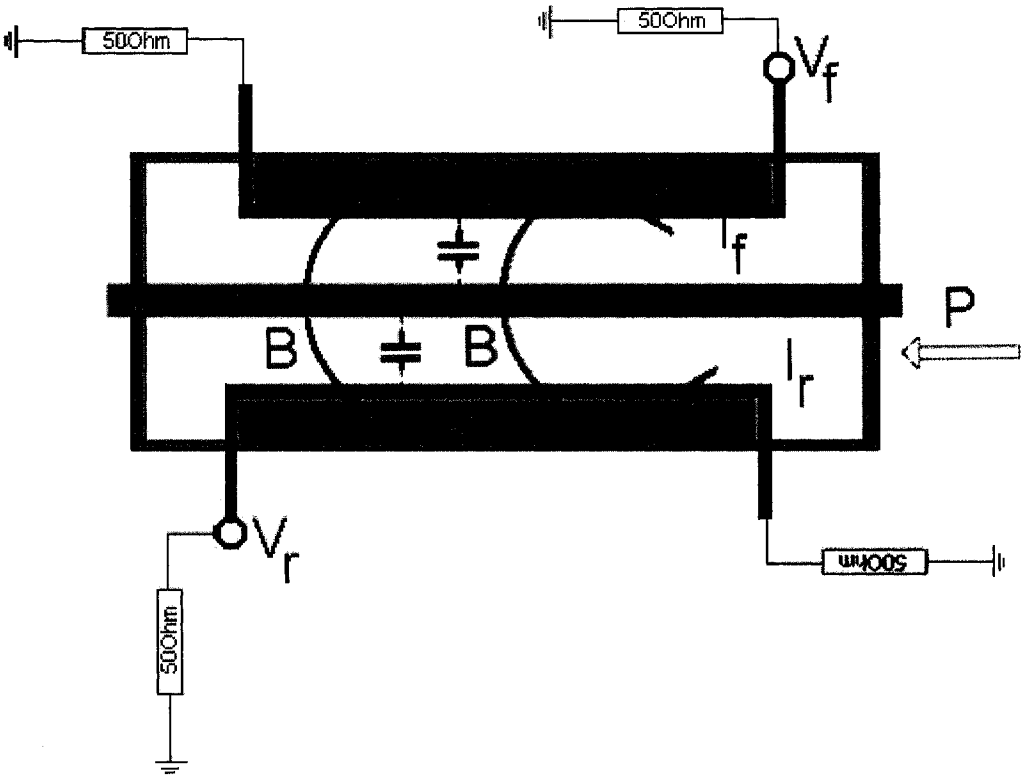

Fig. 2.12 V_f and V_r are generated by electrical and magnetic RF coupling

In a coaxial transmission line, in which the RF currents on the inner and outer conductors are equal and opposite, the RF magnetic flux is zero outside the outer conductor of the line. The construction of the directional coupler current sensing pickup loops are exposed only to the RF magnetic field driven by the RF current that flows though the central red colored conductor in either of two directions. The capacitive coupling between red conductors of the strip line is termed V_e. V_m is the voltage induced by the RF current driven magnetic field. Then the total voltage output of the directional coupler will have the following pair of equations:

$$\begin{cases} V_f = V_e + V_m \\ V_r = V_e - V_m \end{cases} \tag{2.34}$$

Notice that the magnetic induced voltage term V_m has different signs because of the different direction of magnetic fields from forward and reflected currents as set by the left hand rule for electron flow.

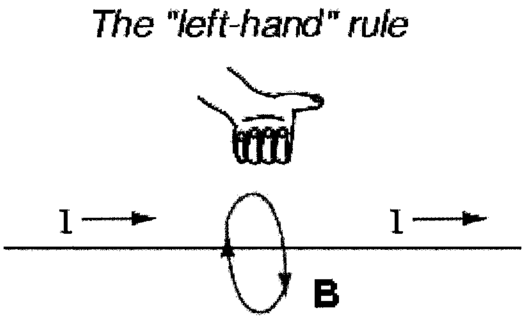

Fig. 2.13 **Left Hand Rule Specifies the Relation Between RF Vectors I and B**

One of the boundary conditions for the proper functioning of the directional is that reflected voltage V_r is zero when the line is adapted or matched to the generator and no reflected wave occurs. This electrical boundary on V_m is accomplished by balancing the ratio of V_m and V_e components (typically by tailoring the termination resistors).

For ease of understanding we consider a coaxial cable and its internal magnetic fields. The RF magnetic flux in a simple coaxial cable exists only between the inner conductor and outer enclosure (Fig. 2.14).

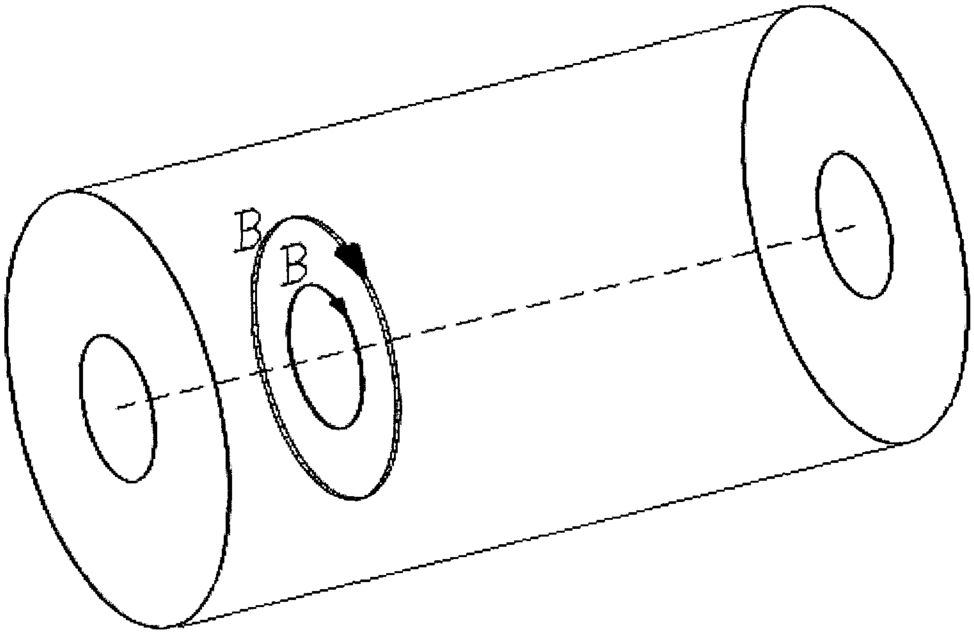

Fig. 2.14 **Magnetic Flux in a Coaxial Line**

If we pass a wire loop (Fig. 2.15) through the outer shield across the enclosure of the directional coupler and back out again, we link all the flux over a precisely known area (blue area in Fig. 2.12) associated with the current in the central conductor. The loop voltage can be analytically determined from fundamental laws.

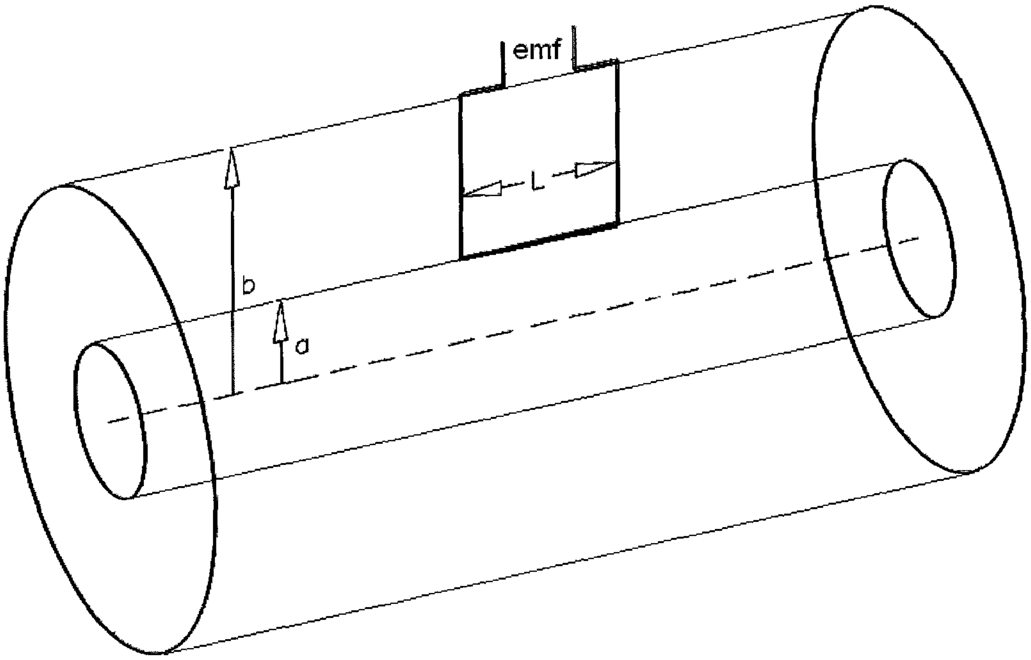

Fig. 2.15 A Wire Loop Placed in a Magnetic Field will Pick up a Voltage

For a long wire carrying a pure sinusoidal current “I”, the magnetic field “B” at a radius “r”, on a perpendicular plane is:

$$B = \frac{\mu_o I}{2\pi r} \tag{2.35}$$

To quantify the total flux Φ over a chosen square area of the current sensor pickup loop we integrate magnetic field “B” over a radius “a” to “b” from the outer edge of the inner conductor to the inner edge of the return path all along the length “L”.

$$\Phi = \int B_n dA = \int_a^b \int_0^L \frac{\mu o I}{2\pi r} dr dl \tag{2.36}$$

$$\Phi = \frac{\mu_0 I}{2\pi} \int_a^b \frac{dr}{r} [l] \tag{2.37}$$

$$\Phi = \frac{\mu_0 IL}{2\pi} \left[\ln r \Big|_a^b \right] = \frac{\mu_0 IL}{2\pi} \ln \frac{b}{a} \tag{2.38}$$

Applying Faraday's Law:

$$V_m = \frac{-d\phi}{dt} = \frac{-\mu_o L \ln(\frac{b}{a})}{2\pi} \frac{dI}{dt} \tag{2.39}$$

For a pure sinusoidal signal:

$$I = I_0 \sin(\omega t + \varphi) \tag{2.40}$$

ω is the radian frequency:

$$\omega = 2\pi f \tag{2.41}$$

φ is the phase between current and voltage. The sinusoidal voltage induced into a magnetic loop by a RF current flowing in the central conductor at r=0 is depicted in formula 2.42. Note that V_m may be positive or negative depending on the direction of the RF power flow measured by the current loop physical placement.

$$V_m = \frac{-\mu_0 L \ln(\frac{b}{a})}{2\pi} I_o \omega \cos(\omega t + \varphi) \tag{2.42}$$

$$V_m = -I_0 \mu_0 L \ln(\frac{b}{a}) f \cos(\omega t + \varphi) \tag{2.43}$$

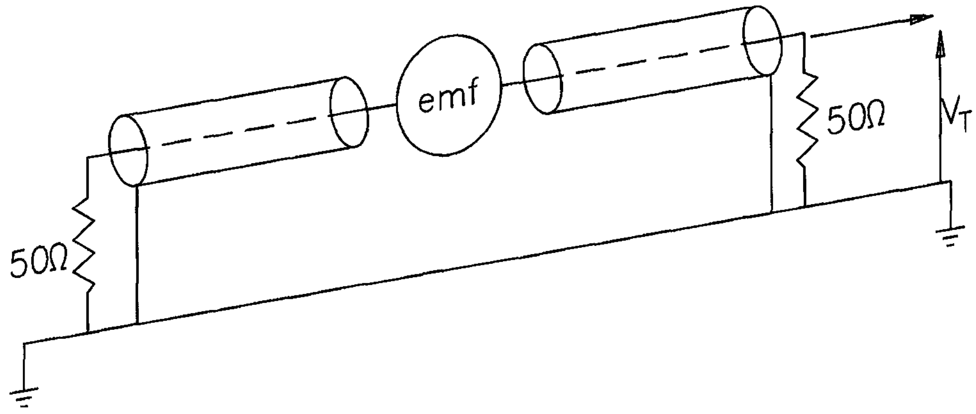

Fig. 2.16 Electrical Representation of a Current Pickup Loop

$$V_m = -I_0\mu_0 L \ln(\frac{b}{a}) f \cos(\omega t + \varphi) \tag{2.44}$$

In conclusion, the RF voltage generated by a directional coupler loop by a magnetic field will be expressed by the formula 2.45.

$$V_m = -K_I I_0 f \cos(\omega t + \varphi) \tag{2.45}$$

K_I is a constant that depends on the design geometry and near field patterns of the directional coupler.

2.4 RF Frequency Selection Circuits

When two or more RF power sources are used on a plasma process it is important to know the relative magnitude of RF and IF energy that is pumped into the chamber at each applied frequency, especially on the fundamentals. Two or more frequencies may deposit substantial energies into the process chamber. On frequency agile RF measurement systems, frequency selection is done using one of the following techniques:

- Analog filtering (low pass or band pass filter).
- Heterodyne mixing of the signal into a predetermined frequency range.

Bandwidth of the chosen RF signal and the associated frequency selective input filter must be matched and it will dictate the measurement frequency span available.

The RF sensor filter should reject any harmonics, but flat enough around the fundamental to measure frequencies of two signals very close to each other. Customer dual RF frequency drive applications are sometimes just off-fundamental by a tens to hundreds of kHz. Overly sharp transitions around fundamental in the RF sensor can cause inaccuracies by too sharp attenuation.

Analog filtering is a classic solution, easy to implement and can account for preservation and measurement of both amplitude and phase even at kW RF power levels. Accurate RF measurement systems require temperature stable RF components. Use of temperature insensitive Negative-Positive-Zero (NPO) capacitors is a must. The inductors should be mechanically stable and be selected with air core or some powder-iron core that is stable with temperature. With all this temperature precautions there still are some variations at temperature transitions (due to mechanical contractions/dilatations).

Problems with analog solutions may arise when the RF source contains two frequencies such as 100MHz and 13.56MHz both delivering large powers to the same process system. Frequency agile capabilities become required. An elegant solution to this need, for a frequency agile, is the heterodyne design scheme. The super-heterodyne principle is to down-frequency convert all signals we wish to measure into the same exact IF (Intermediate Frequency) frequency region allowing one identical IF amplifier for all RF frequencies measured.

Mathematically let's assume that we have two sinusoidal signals that we are going to combine in an analog mixer circuit:

$$S_1 = A_1 \sin(\omega_1 + \varphi_1) \tag{2.46}$$

$$S_2 = A_2 \sin(\omega_2 + \varphi_2) \tag{2.47}$$

The result of the two frequency mix can be obtained by using the 2.48 trigonometric formula below. Expression 2.48 will simplify the product of two sinusoidal signals into two components one at a higher and one at a lower frequency.

$$A_1 A_2 \sin(\omega_1 + \varphi_1)\sin(\omega_2 + \varphi_2) = \frac{A_1 A_2}{2}\cos[(\omega_1 + \omega_2)t + \varphi_1 + \varphi_2] + \frac{A_1 A_2}{2}\cos[(\omega_1 - \omega_2)t + \varphi_1 - \varphi_2] \tag{2.48}$$

We are interested in the difference signal at a fixed IF frequency set by bringing the probe mixing signal to within the IF frequency of the target RF frequency. Usually the IF signal is called intermediary frequency and, for radio frequencies, it is either 455 kHz or 10.7 MHz. Of keen interest is that the phase information of the target RF signal is preserved in this down shifting into a fixed IF band.

The benefits for the super-heterodyne circuits in RF measurements are summarized as:

- Excellent RF harmonic and spurious RF signal rejection.
- The tuned heterodyne amplifier circuit will require only low frequency. IF components rather than the RF frequency of the target frequency.

One disadvantage of the heterodyne is the complexity of the design. To implement such a solution we have to synthesize a variable frequency comparable with the frequency that we have to measure. The technology offers plenty of solutions but all of them involve extensive development resources.

A more complete description of how we employ a heterodyne circuit to accurately measure V, I, ϕ for RF target frequencies is described later in this dissertation.

2.5 Analog Circuit

The functions of the analog measurement circuit are amplification (gain scaling), low frequency filtering (smoothing the signal), multiplication, RMS calculations and A/D (Analog to Digital conversion)[46-50] as detailed below. No matter what kind of RF input sensor is used (directional coupler or simple V/I sensor circuits), the calculation of the RF power involves squaring the RF voltage or current signal. The analog multiplier or an RF diode circuit with a polynomial second-degree transfer function are both options that we describe below.

Typically, an analog multiplicator can achieve 1% accuracy. However, beside analog multiplication there are other errors occurring such as voltage offset and temperature drifts. I will propose later in the dissertation an auto-zero method and give test results justifying this choice. First let's examine the problems with commercial multiplier chips.

Some representative analog multipliers include: HS2556, AD734, AD835. Expression 2.49 is a typical transfer function for the AD835 multiplier whose simplified circuit diagram is given in Fig 2.17.

$$W = \frac{(X_1 - X_2)(Y_1 - Y_2)}{U} + Z \qquad (2.49)$$

Note that we obtain a scaled product capability as well as an arbitrary offset term Z.

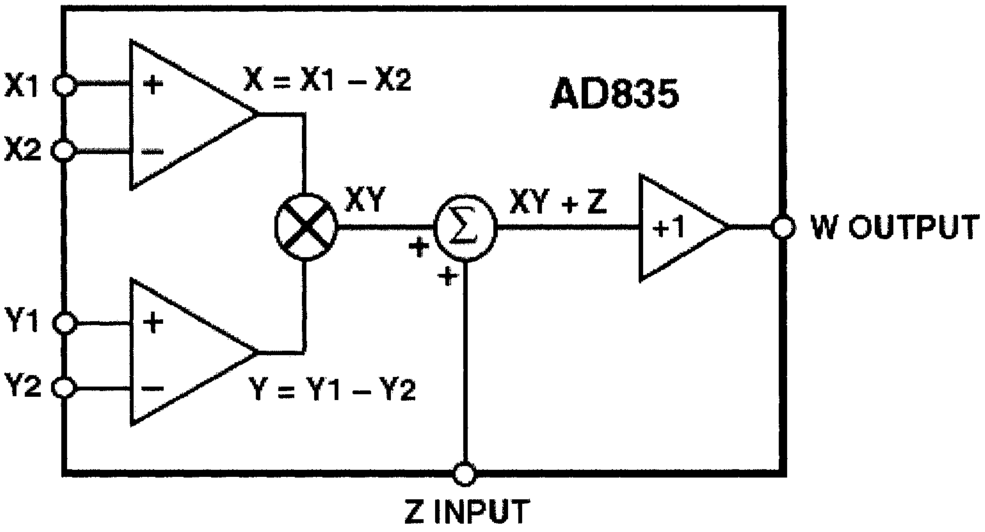

Fig. 2.17 **Analog Multiplier Schematic Block**

If the design will incorporate a digital circuit, a simple calculation of V_{rms} is enough. The digital circuit will have to do the conversion from peak voltage V_{pk} to average voltage V_{rms} as well as the multiplication. A simple approach to the peak voltage detector circuit is presented in Fig. 2.18.

Peak to RMS conversion is simply a matter of multiplying the peak voltage by 0.707:

$$V_{rms} = V_{pk} * \sqrt{2}/2 \tag{2.50}$$

A classic approach to the peak voltage detector circuit is presented in Fig. 2.18:

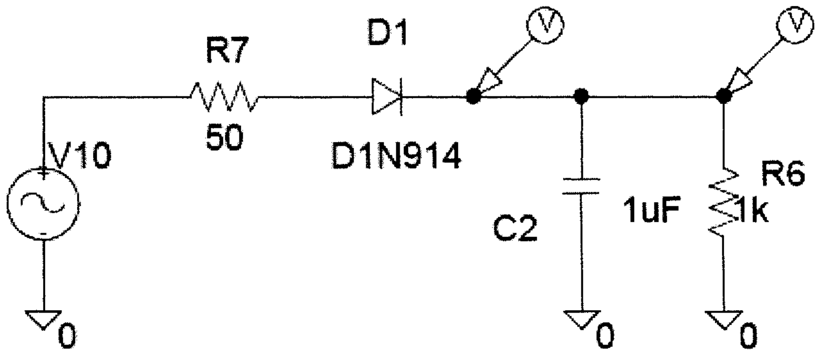

Fig. 2.18 Single RF Peak Voltage Diode Circuit

The advantage of this circuit is simplicity and extremely high frequency range by the availability of high frequency diodes. The drawbacks of single RF peak detection are the finite diode threshold voltage, the non-linear diode characteristic and the temperature drift.

Diode threshold limitations of this circuit are addresses by dual diode peak detectors discussed later in this dissertation.

A/D circuits have to transform the peak or RMS analog signal into a digital signal. Some of the information may be lost during the conversion if minimum precautions are not employed. The typical characteristics of the A/D are the number of bits (quantization) and speed (measured in samples per second). An important circuit that is associated with the A/D is the voltage reference. Either internal or external to the A/D, the voltage reference will dictate the accuracy, temperature drift and long-term stability of the A/D.

Table 2.1 A/D Quantization Error Depends on the Number of Bits

Number of A/D bit	Quantization Error (%)
8	0.390625
10	0.09765625
12	0.024414063
14	0.006103516
16	0.001525879

Analog Devices, Texas Instruments, Linear Technologies and Maxim are several manufacturers that are providing high performance A/D converters. For RF measurements, where we need better than 1% accuracy, 12 or more bits of resolution should be considered. Dual channels A/D and several ppm/°C for voltage references are required. We will show in the thesis the replacement of analog portions of the RF measurement system by digital algorithms. Proper digital algorithms can do the same functions as analog circuits: analog heterodyne frequency conversion, analog filtering and scaling. In addition of these capabilities there are unique functions of digital circuits (employ correction factors and I/O management) that make them better candidates for RF measurements.

2.6 Digital Circuit Emulation and Replacement of Analog Circuits

The digital circuit block can replace many of the analog functions on the mixed analog-digital RF measurement system due to advances in Digital Signal Processors. Digital processors excel when it comes to mathematical functions (like multiplying, squaring a number or complex corrections based on look up tables). On top of all the analog functions that they can implement, DSP also can give us the convenience of data communication (serial/parallel interfaces) and I/O for digital display.

Major commercial vendors for DSP are Motorola, TI, Xilinx and Microchip. For ease of use Microchip has hardware power, while it requires no special programming skills. For example the 16F873A controller has a digital interface, LCD interface, serial interface, 20 MHz clock (at 2-3 clock cycles/instruction), analog interface (unfortunately on 10bit), 8kB of EPROM, 128B of EEPROM at less than $10/pc. Using support software (compiler) the firmware can be developed using a set of instructions similar to Basic. For an intensive digital manipulation at low cost the FPGA from Xilinx called Spartan3 is preferred because of the following features:

- Embedded 18x18 bit multipliers to support high-performance DSP applications
- On-chip digital clock managers (DCMs) eliminating the need for external clock management devices

- Distributed memory and 16-bit shift register logic (SRL-16) efficiently implementing DSP functions
- 18Kb Block RAM that can be used as buffer memory or cache
- Digital on-chip termination eliminating the requirement for multiple external resistors
- Eight independent I/O banks supporting 24 different I/O standards

The combination of low-cost and full-feature capability means that the Spartan-3 Generation FPGAs can implement complete system functions in the most cost-efficient manner.

In summary, in Chapter 2 we have reviewed both the analog and digital building blocks that I have employed in my thesis research for RF power measurement at kW power levels and have detailed the capabilities and limitations of building the blocks, components and the overall system. This work on real impedance solutions sets the stage for Chapter 3 where RF measurements on complex lines and impedances are discussed. This leads to Chapters 5 and 6 where my novel designs and test results to RF power measurement are detailed.

2.7 References

[1] Hewlett-Packard Product Note 8510-5A, Specifying Calibration Standards for the HP 8510 Network Analyzer, (Feb. 1, 1988).

[2] Cronson, A Six-port Automatic Network Analyzer, IEEE Trans on MW Theory and Techniques, (Dec. 1977).

[3] Gerrish, K.S., US Patent No. 6,44,95,68, (September 10, 2002).

[4] Gerrish, K.S.,, US Patent No. 6,70,81,23, (March 16, 2004).

[5] Jeanne Cranford & team, Sematech, Radio Frequency (RF) Measurement and Control Project Report (TECQ001) (September 10, 1998).

[6] Gonzalez, J.J., Geissler, S.J., Tomasel, F.G., US Patent No. 7,00,58,45, (February 28, 2006).

[7] Carr, Joseph J., Sensors & Circuits: Sensors, Transducers, & Supporting Circuits For Electronic Instrumentation Measurement and Control, Prentice Hall PTR, 1st edition (July 14, 1997).

[8] Carr, Joseph J., Secrets of RF Circuit Design, McGraw-Hill/TAB Electronics, 3 edition (December 11, 2000).

[9] Huijsing, J.H., Steyaert, Michiel and van Roermund, Arthur, Analog circuit design: sensor and actuator interface electronics, integrated high-voltage electronics and power management, low-power and high-resolution ADC's, Kluwer Academic, (2004).

[10] IEE training course, How to design RF circuits, Kluwer Academic Publishers, (2000).

[11] Lenk, John D., Optimizing wireless/RF circuits, McGraw-Hill, (1999).

Steyaert, Michiel, Arthur H.M. van Roermund, Johan H. Huijsing, Analog circuit design: Workshop of Advances in Analogue Circuit Design (14th: 2005: Limerick, Ireland), Springer, (2005).

[12] Bahl, Inder, Lumped elements for RF and microwave circuits, Artech House, (2003).

[13] Maas., Stephen A., Nonlinear microwave and RF circuits, 2nd ed., Artech House, (2003).

[14] Besser, Les., Practical RF circuit design for modern wireless systems. Vol. 1, Passive circuits and systems, Artech House, (2003).

[15] Gilmore, Rowan, Besser, Les, Practical RF circuit design for modern wireless systems. Vol. II, Active circuits and systems, Artech House, (2003).

[16] Medley, M. W. (Max W.), Microwave and RF circuits: analysis, synthesis, and design, Artech House, (1993).

[17] Abramowitz, Milton and Irene A. Stegun (editors), Handbook of Mathematical Functions, Dover Publications, Inc., New York, (1970).

[18] Berkeley Physics Course, Electricity and Magnetism, volume 2, (1963).

[19] Stratton, Julius A., Electromagnetic Theory, McGraw Hill, Inc., New York (1941).

[20] Pozar, David M., Microwave Engineering Second Edition, Wiley, New York, (1998).

[21] Edwards, T.C., Foundations for microstrip circuit design, Wiley Chichester, Wes, (1991).

[22] Gupta, K.C., Microstrip lines and slotlines / K.C. Gupta, Ramesh Garg, I. J. Bahl. Artech House Dedham, Mass., (1979).

[23] Gardiol, F. E., Microstrip circuits, Wiley, New York, (1994).

[24] Fooks, E. H., Microwave engineering using microstrip circuits, Prentice Hall New York, (1990).

[25] Kompa, Gunter, Practical Microstrip Design And Applications (Artech House Microwave Library), Artech House Publishers (September 30, 2005).

[26] Jia-Shen G. Hong and M. J. Lancaster, Microstrip Filters for RF/Microwave Applications, Wiley-Interscience, 1 edition (June 22, 2001).

[27] T. C. Edwards and M. B. Steer Foundations of Interconnect and Microstrip Design, John Wiley & Sons, 3 edition (January 17, 2001).

[28] Kin-Lu Wong, Design of Nonplanar Microstrip Antennas and Transmission Lines, Wiley-Interscience, 1 edition (March 1, 1999).

[29] Gardiol, Fred, Microstrip Circuits (Wiley Series in Microwave and Optical Engineering) by Wiley-Interscience (March 1994).

[30] Hearn, C.P., E.S. Bradshaw, and R.J. Trew, The effect of coupling line loss in microstrip to dielectric resonator coupling, Microwave Journal by Microwave Journal, v33, 169(4) (November 1,1990).

[31] Bogatin, Eric, Microstrip or stripline? That is the question ,Printed Circuit Design & Manufacture, Printed Circuit Design & Manufacture, Thomson Gale, (Feb 1, 2006).

[32] Schrader, David H., Microstrip Circuit Analysis, Prentice Hall (May 1995).

[33] Lee, Thomas H., Planar microwave engineering: a practical guide to theory, measurement, and circuits, Cambridge University Press, (2004).

[34] Barrett, R.M. and Barnes, M.H., Microwave Printed Circuits, presented at IRE National Conference on Airborne Electronics, Dayton, OH, (1951).

[35] Grieg, D.D. and Englemann, H.F., Microstrip – A New Transmission Technique for the Kilomegacycle L Range, IRE Proceedings, Vol. 40, 1644, (1952).

[36] Tresselt, C.P., The Design and Construction of Broadband High-Directivity 90° Couplers Using Non-Uniform Line Techniques, IEEE Transactions on Microwave Theory and Techniques, Vol. 14, No. 12, 647–656, (December 1966).

[37] Lange, J., Interdigital Stripline Quadrature Coupler, IEEE Transactions on Microwave Theory and Techniques, Vol. 17, No. 12, 1150–1151, (December 1966).

[38] Podell, A., A High Directivity Microstrip Coupler Technique, 1970 International Microwave Symposium Digest, 33–36, (1970).

[39] Wilkinson, E., An N-way Hybrid Power Divider, IEEE Transactions on Microwave Theory and Techniques, Vol. 8, No. 1, 116–118, (January 1960).

[40] Parad, L.I. and Moynihan, R.L., Split-Tee Power Divider, IEEE Transactions on Microwave Theory and Techniques, Vol. 13, No. 1, 91–95, (January 1965).

[41] Cohn, S.B., A Class of Broadband Three-port TEM-mode Hybrids, IEEE Transactions on Microwave Theory and Techniques, Vol. 16, No. 2, 110–118, (February 1968).

[42] Levy, R. and Cohn, S., A History of Microwave Filter Research, Design and Development, IEEE Transactions on Microwave Theory and Techniques, Vol. 32, No. 9, 1055–1067, (September 1984).

[43] Matthaei, G., Young, L. and Jones, E.M.T., Microwave Filters, Impedance-matching Networks and Coupling Structures, Artech House Inc., Norwood, MA, (1980).

[44] Carlin, H.J., Principles of Gyrator Networks, Proceedings Modern Advances in Microwave Techniques, Polytechnic Institute of Brooklyn, 175, (November 1954).

[45] Bosma, H., On the Principle of Stripline Circulation, Proceedings of the IEEE, Vol. 109B, 137, (1961)

[46] Carr, Joseph J., Elements of Electronic Instrumentation and Measurements (3rd Edition), Prentice Hall, 3rd edition (October 16, 1995).

[47] Pallas, Abraham, Carr, Joseph J., Electronic Devices (Glencoe Tech Series), McGraw-Hill/Glencoe (January 1993).

[48] Ahn, Gil Cho, Design techniques for low-voltage and low-power analog-to-digital converters: (PhD Dissertation), OREGON STATE UNIVERSITY, (Apr 2006).

[49] Kester, W., High-Speed Design Seminar, Analog Devices, 2nd ed., I-55 to I-69, (Apr. 1990).

[50] Kester, W., Mixed-Signal Design Seminar, Analog Devices, III-2 to III-11, (Mar. 1991).

CHAPTER 3

Previous Methods for RF High Power Measurement on Complex Impedance Lines and Loads

3.1 Background

The precise behavior of the RF driven plasma is sought and RF sensor design needs to find more accurate methods below 1% accuracy to better control RF driven plasma process[1-12] or to achieve more precise processing of ever smaller feature sizes. Driven by industry demand for tighter process control accurate RF power and impedance measurement needs evolved recently to require accuracy better then 1%. In some cases the mathematical knowledge was available to improve accuracy, but the hardware infrastructure was lacking. Recent parallel advances in digital signal processors and fast analog chips made possible to improve accuracy into RF instrumentation, as we will discuss herein.

Measurement into real impedance lines is less technically demanding, but without proper consideration can lead to poor or inconsistent results as shown in Chapter 2. An analysis and proposed improvement of the RF power measurements technique into real impedance lines are done in Chapter 4 of this dissertation, but here we focus on the unique problems of mismatched lines with large VSWR ratios and with kW RF power level. Chapter 5 will address new means for obtaining all digital RF measurements in complex impedance lines

Prior research[13-43] into developing better voltage and current sensors on mismatched lines was limited by analog and digital hardware limitations. New digital signal processors open new pathways to RF sensor and power measurement to system designers.

The following methods presented into this chapter for measurements in complex impedance lines at RF high power (W to kW) will introduce the reader to the unique issues involved. Detailed discussions of my designs for all digital RF power sensor systems are given in Chapter 5, but the motivation for this approach is found here.

3.2 RF High Power Measurement Technique # 1 – Z-Scan

Z-Scan[44] technology is a proprietary RF power and impedance technique patented by Advanced Energy Ind. The instrument can measure complex impedances into powers up to 10kW at frequencies up to 30MHz: voltage, current and phases are the first electrical values that are calculated utilizing a V/I sensor. From these three values both the RF power and RF impedances are computed. Key to this technique is the methodology by which the phasor φ is calculated. Using simple trigonometry and the cosine theorem we can evaluate the module of the angle between the voltage vector v and the current vector i.

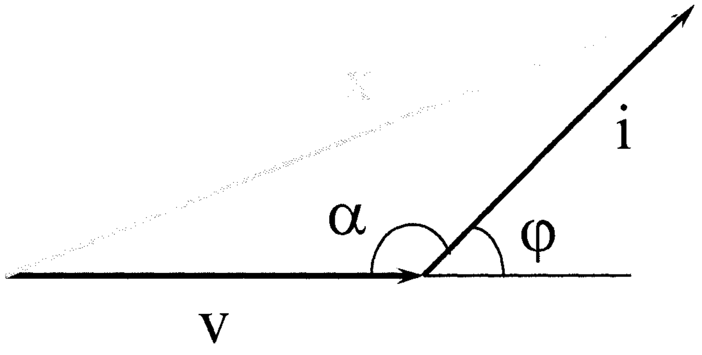

Fig. 3.1 v and i Phasor Diagram

According to Fig. 3.1 the sum of the angle α and φ is 180 degrees

$$\alpha = \pi - \varphi \tag{3.1}$$

$$\cos\alpha = \cos(\pi - \varphi) = -\cos\varphi \tag{3.2}$$

Applying the cosine theorem on Fig. 3.1 we obtain equation 3.3:

$$X^2 = V^2 + I^2 - 2VI\cos\alpha \tag{3.3}$$

$$X^2 = V^2 + I^2 + 2VI\cos\varphi \tag{3.4}$$

$$\cos\varphi = \frac{X^2 - V^2 - I^2}{2VI} \tag{3.5}$$

The sign of the phasor φ determines an extra vector termed *Y* (discussed in Fig 3.4) by adding 90 degrees to the *I* phasor. The analog operational amplifiers accomplish all mathematical operations.

The post sensor signal processing flow diagram signal for *V*, *X* and *I* is illustrated in Fig. 3.2.

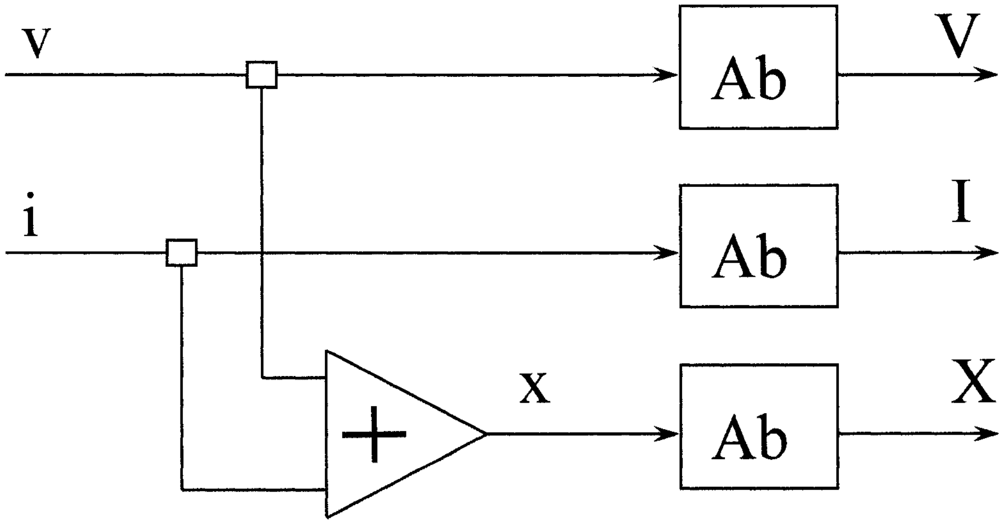

Fig. 3.2 **Initial Signal Processing Solution for Z-SCAN**

If the measurement system provides the properly scaled value for the vector *V* and current vector *I*, then the module value of the angle φ can be calculated. However, the result of the calculation (using the cosine theorem) is not unique because it does not give the information about the sign of the angle.

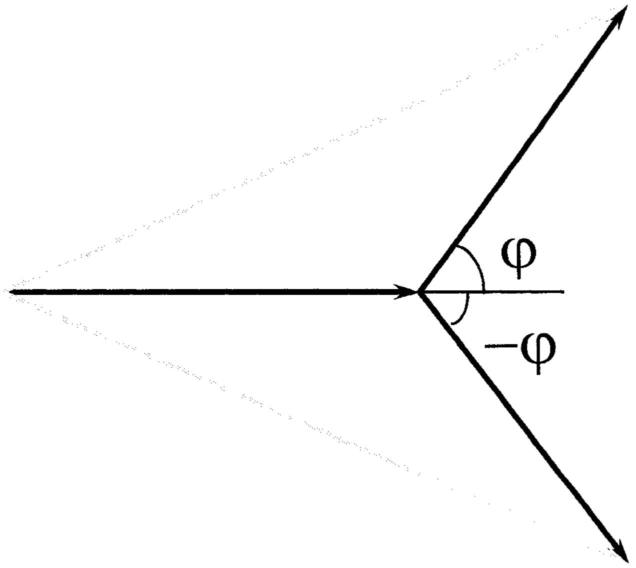

Fig. 3.3 **The Trigonometric Solution of the Cosine Theorem is not Unique to the Sign of Angle ϕ so Additional Calculations are Necessary**

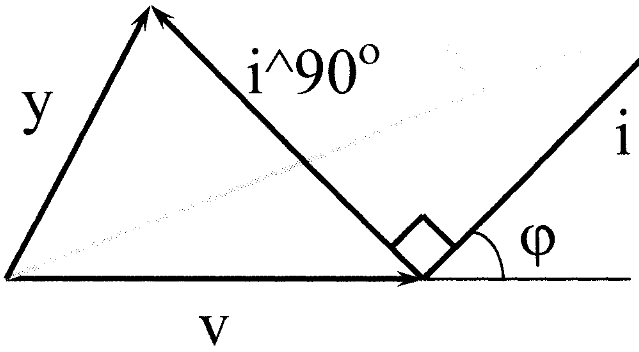

Fig. 3.4 **An Extra Vector, Y, is Required to Calculate the sinϕ**

Using simple analog circuits we can change the phase of the vector *I* by 90 degrees. Using the additional vector *Y* we can also calculate sinφ to determine the sign of the angle. We apply again the cosine theorem, however this time on the triangle that includes vector phasor *Y*:

$$Y^2 = V^2 + I^2 + 2VI\cos(\varphi + \frac{\pi}{2}) \tag{3.6}$$

$$\cos(\varphi + \frac{\pi}{2}) = \cos\varphi\cos\frac{\pi}{2} - \sin\varphi\sin\frac{\pi}{2} = -\sin\varphi \tag{3.7}$$

$$Y^2 = V^2 + I^2 - 2VI\sin\varphi \tag{3.8}$$

$$\sin\varphi = -\frac{Y^2 - V^2 - I^2}{2VI} \tag{3.9}$$

$$\cos\varphi = \cos(-\varphi) \tag{3.10}$$

$$\sin\varphi = \sin(\pi - \varphi) \tag{3.11}$$

The sign of cosφ and sinφ functions are summarized below by quadrants.

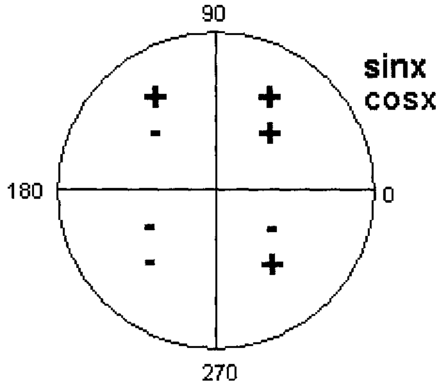

Fig. 3.5 Cos and Sin Sign in all 4 Quadrants

$$\sin(\pi - \varphi) = \sin\pi\cos\varphi - \cos\pi\sin\varphi = \sin\varphi \quad (3.12)$$

With the angle φ calculated using both sine and cosine functions we can uniquely determine the sign of the angle between voltage and current.

This technique will determine the voltage and current amplitude and it will calculate the angle between current and voltage. The signal-processing pathway for this is summarized in Fig. 3.6. Once these three elements are calculated, all the other information (power, impedance) can be calculated from the appropriate power or impedance triangles.

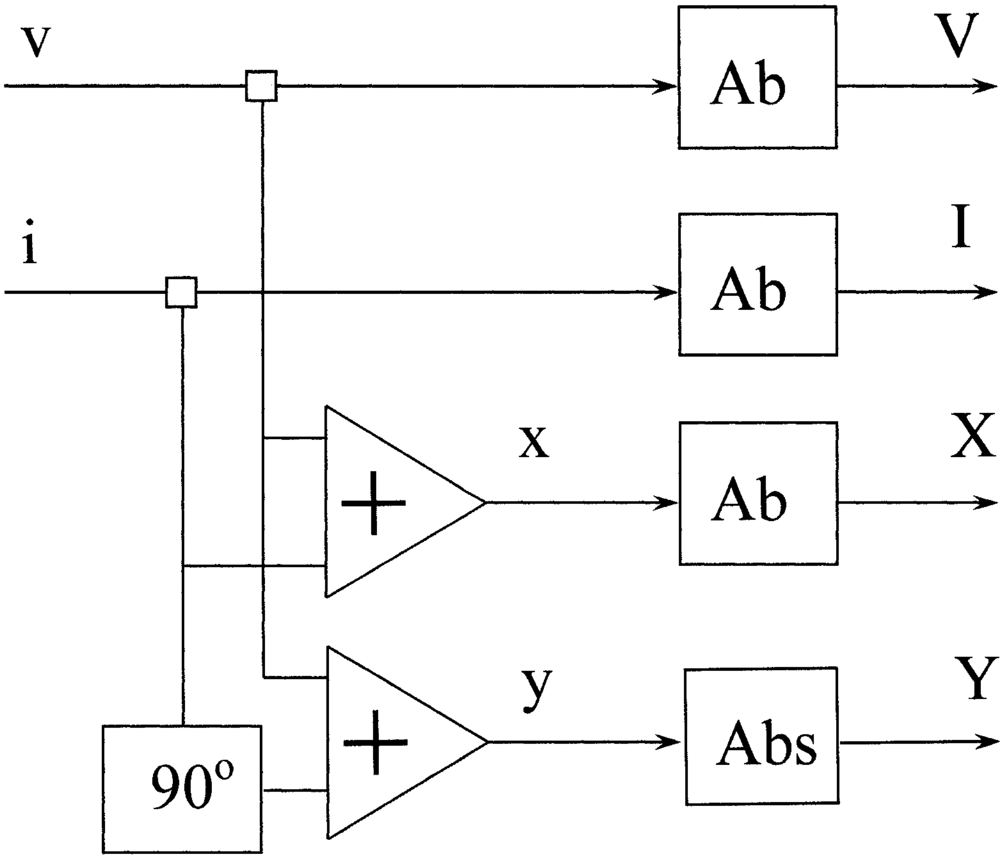

Fig. 3.6 Signal Processing Solution Pathway for Z-SCAN

The errors and limitations of the Z-Scan technique come both from hardware and firmware. Accurate gain scaling of the voltage and current as well as an accurate 90 degrees phase change are the issues that affect accuracy of the angle. The maximum frequency limitation is due primarily to computing resources.

Calibration of the Z-Scan is done using a three-load approach: Open/Short/Load conditions as well as a 50Ω calorimetric reference. Table 3.1 summarizes the accuracy limits of the Z-scan approach.

Table 3.1 Z-Scan Power Accuracy- Source User Manual PN#5705078-C

Degrees (phase angle)	Power Error (%)
0-30	2
30-50	2.5
50-70	3
70-75	3.5
75-80	4
80-85	6
85-87	8
87-88	11
88-89	19
89-89.5	31

The accuracy is 2% or above into 50Ω and it degrades with increasing VSWR encountered in unmatched loads. The maximum error occurs at extreme loads, pure capacitive or pure inductive loads where the angle between current and voltage is 90 degrees.

3.3 Analog Dominated RF High Power Measurement Technique # 2 - Real/Reactive Power Triangle Method

Implementing mathematical functions using analog design can still surpass computing limitations for some applications[45]. In general, the analog design will greatly improve speed and therefore it will work at higher frequencies, but the analog nature always makes the absolute calibration more difficult.

The heterodyne design is an old concept based on the mix of two different frequency signals to create a new signal at lower frequency that preserves all amplitude and phase information. This mix creates a signal with a frequency equal to the difference between the two mixed signals. A single local probe oscillator signal is used to mix with the target RF frequencies on both the RF voltage and RF current (or forward and reflected voltages) input channels.

The heterodyne will lower the frequency that has to be processed (so less performance analog circuits can be used) while it maintains the information of the original signal. Another point of view is that high frequencies can be analyzed (high frequencies that can not be approached with today's circuits).

The mathematical equation for mixing two sinusoidal signals is:

$$\begin{aligned} &A_1 A_2 \sin(\omega_1 + \varphi_1)\sin(\omega_2 + \varphi_2) = \frac{A_1 A_2}{2}\cos[(\omega_1 + \omega_2)t + \varphi_1 + \varphi_2] + \\ &\frac{A_1 A_2}{2}\cos[(\omega_1 - \omega_2)t + \varphi_1 - \varphi_2] \end{aligned} \tag{3.13}$$

From equation 3.13 we are interested in the difference signal (the sum signal is filtered out):

$$f(x) = \frac{A_1 A_2}{2}\cos[(\omega_1 - \omega_2)t + \varphi_1 - \varphi_2] \tag{3.14}$$

If one could calculate the power and the square of the voltage or current, then all other RF information in power and impedance triangles can be derived. To better visualize the topology look at Fig 3.7 which traces the forward and reflected voltages measured using a strip-line as they are first heterodyned to an IF frequency and then passed trough a low filter circuit to eliminate the higher component of the heterodyne mix. Analog calculations form the four quantities V^2, P, I, Q and I that enter into a digital signal processor for calculations for the power and impedance triangles.

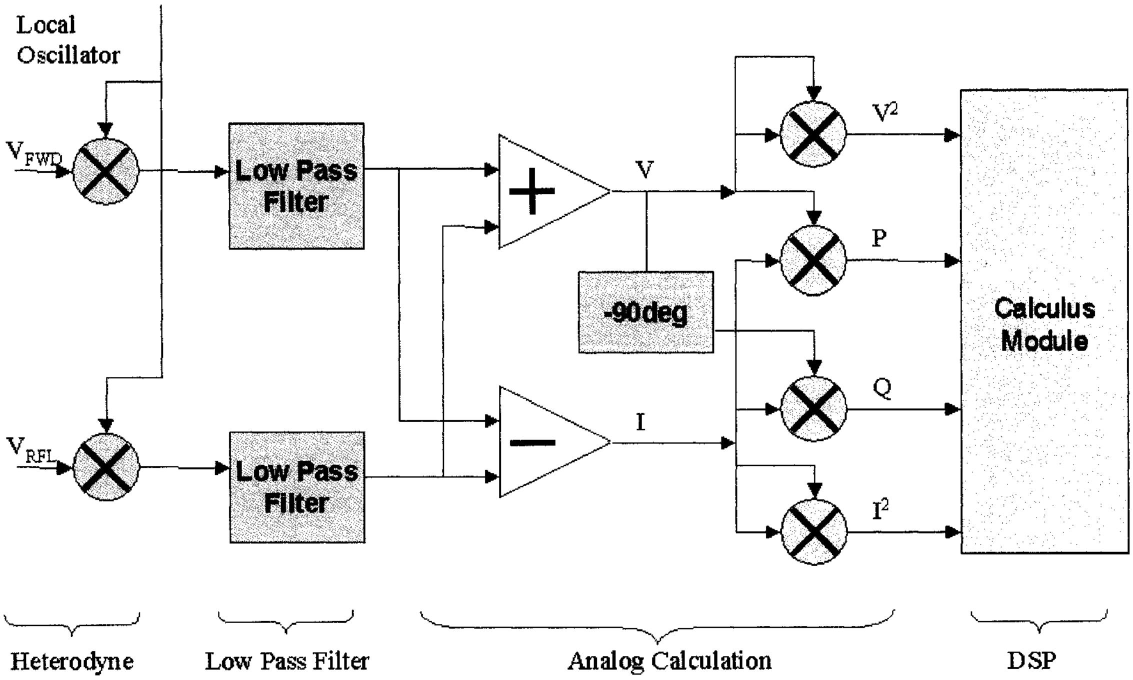

Fig. 3.7 Analog Heterodyne Based Measurement System

To calculate the RF elements (impedance components), this solution measures first both real power P and reactive power Q and then calculates the load impedance Z and phase angle φ.

$$\begin{cases} P = VI\cos\varphi \\ Q = VI\sin\varphi \end{cases} \tag{3.15}$$

This approach was never used historically at RF frequency because the necessary direct measurements could not be made, but today modern precision wideband analog multipliers make it possible. A 90 degrees shift block will also allow calculating the reactive power Q.

$$\sin\varphi = \cos(\varphi - \frac{\pi}{2}) \tag{3.16}$$

This technique provides the user with four terms with which to determine the characteristics of the load. The values of V^2 and I^2 as well as the in phase and quadrature phase products of V and I are available. Only three of the four terms are actually required to determine the phase and impedance of the circuit.

Using signals V^2, P, and Q we may derive the same result. Also, I^2, Q and P could be used as a second solution pathway. The final solution can be determined by averaging the two methods. This technique permits accurate and repeatable data to be collected.

Let us consider the general expression 3.17 for the impedance Z:

$$Z = R + jX \tag{3.17}$$

Circuit impedances can be derived from the current and voltage by:

$$R = \frac{P}{I_{rms}^2} \tag{3.18}$$

$$X = \frac{Q}{I_{rms}^2} \qquad (3.19)$$

Expression 3.20 calculates the phase of the current with respect to the voltage.

$$\varphi = \tan^{-1}\frac{Q}{P} \qquad (3.20)$$

One other way of calculating the impedance elements can be found in expressions 3.21 and 3.22.

$$R = \frac{V_{rms}^2}{P} \qquad (3.21)$$

$$X = \frac{V_{rms}^2}{Q} \qquad (3.22)$$

This technique depends on either a digital processor or software to calculate load impedance[46, 47]. No published performance specification is available, but it is estimated that this technique can achieve 1% accuracy into 50Ω.

3.4 Mixed Analog/Digital RF High Power Measurement Technique # 3 – Heterodyne + DSP for Error Correction

Advances into the Digital Signal Processors (DSP) made possible to push the digital application boundaries and replace analog functions. The technique proposed by Gerrish[48, 49] is using an analog mixer (superheterodyne) followed by a pair of Analog to Digital converters and a DSP (Fig. 3.8).

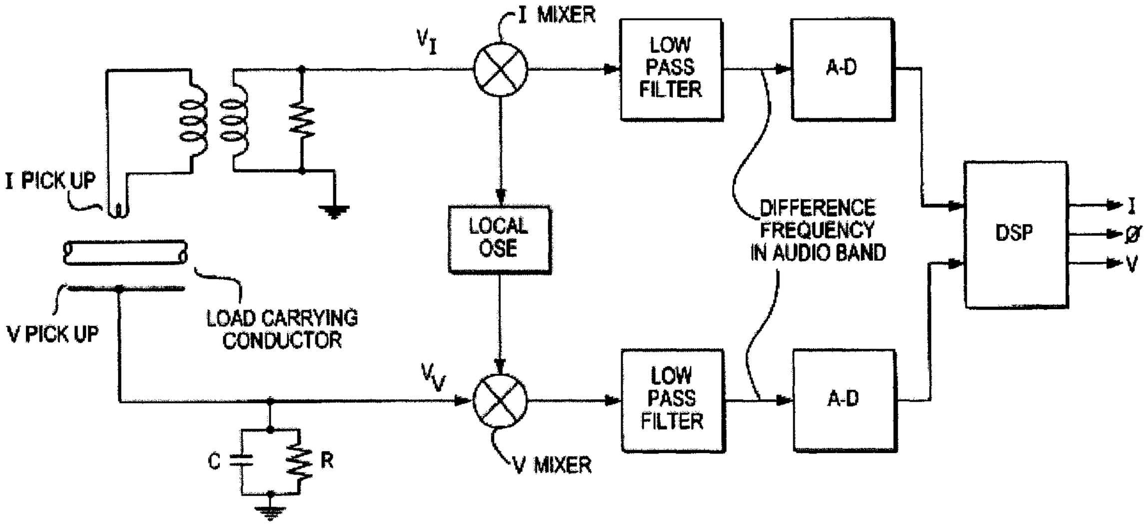

Fig. 3.8 Analog Heterodyne Measurement System with a Digital Error Correction Solution

In order to reduce the errors of the method along Gerrish focused on improving the V/I sensor along with an error compensation algorithm. For every operating frequency between successive calibrated radio frequencies (for which the correction coefficients are stored) correction coefficients are applied by interpolating between stored values. The method claims that it can achieve 0.2 degrees phase accuracy. Absolute phase accuracy does not give us clear information about the overall accuracy because the gradient of the phase is not linear (as explained next in the calibration procedure for component variations at high Rf power flow conditions).

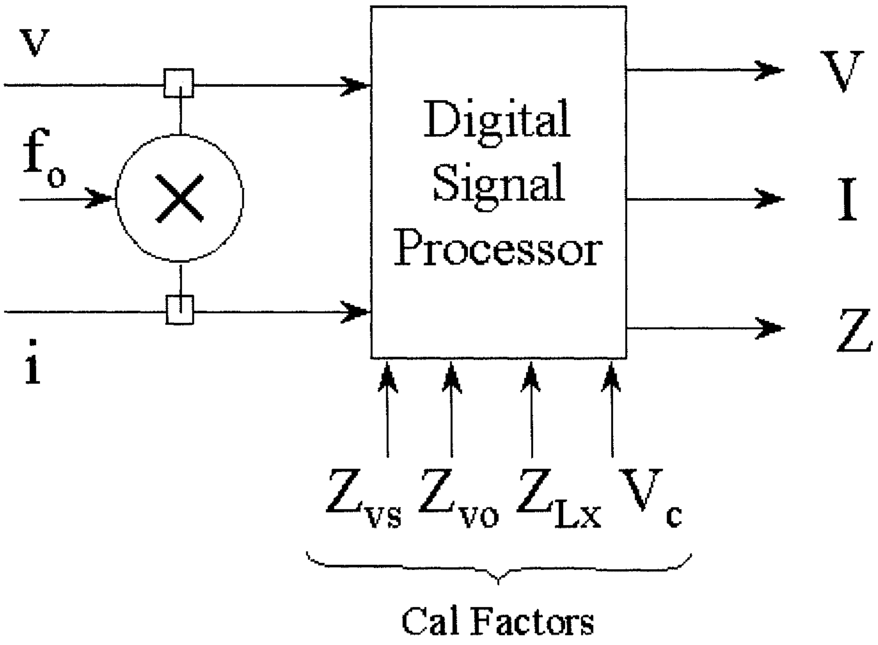

Fig. 3.9 **Signal Processing Schematic for US PAT No. 6,708,123**

The digital calibration of the circuit is done for several frequencies per decade using four well-known calibration standards:

a) Short circuit will generate the calibration constant Z_{vs}.

b) Open circuit will generate the calibration constant Z_{vo}.

c) 50Ω load (adapted load) will generate the calibration constant Z_{LX}.

d) Voltage or Current Standard (known value) will generate the calibration constants V_c, respectively I_c.

The DSP calculates the load voltage V, current I, and impedance Z for any arbitrary load using the following correction formulas:

$$\begin{cases} Z = Z_{Lx} * \dfrac{Z_v - Z_{vs}}{Z_{vo} - Z_v} \\ |V| = \left| v * \dfrac{Z_v - Z_{vs}}{V_c} \right| \\ |I| = \dfrac{|V|}{|Z|} \end{cases} \tag{3.23}$$

with

$$Z_v = \frac{v}{i} \tag{3.24}$$

The absolute accuracy for this commercial measurement system (MKS V/I Probe 4100) is 1% for power and 1.5% for impedance. This is still not enough to meet the new needs for less then 1% accuracy and sets the stage for my contributions in Chapters 4 and 5.

3.5 Summary

I identified and focused my researched on three of the most performing methods of RF high power measurements. All of them involve analog circuits and digital signal processing. None of the investigated techniques is breaking the 1% accuracy barrier for power.

3.6 References

[1] Meuth, H. et al., Excitation and damping of a compressional hydromagnetic waves on a magnetized, high pressure plasma column, Database Inspec Institute of Electrical Engineers, Insp. No. 2795644, and Physics of Fluids, vol. 29, No. 9, 3036-3051, (Sep. 1986).

[2] Liland, K.B. et al., Model confirmation of an experimental method for determination of sheath length in a low-pressure glow discharge, Database Inspec Institute of Electrical Engineers, Inspec. No. 4867293, and Journal of Physics D (Applied Physics), UK, vol. 27, No. 12, 2670-2672, (14 Dec. 1994).

[3] McKinney, W. R. et al., Plasma Discharge Cleaning of Replica Gratings Contaminated by Synchrontron Radiation, Nuclear Instruments and Methods, 195, 371-374, (1982).

[4] Shannon, R. L. et al., Active Cleaning Technique Device, Design Study Summary Report D180-15454-1, 1-60, (Mar. 1973).

[5] Lohner, T. et al., Short Communication-The Role of Surface Cleaning in the Ellipsometric Studies of Ion-Implanted Silicon, Radiation Effects, vol. 54, 251-252, (1981).

[6] Splichal, M. P. et al., Application of chemometrics to optical emission spectroscopy for plasma monitoring, Department of Chemical and Nuclear Engineering, Univ. of N. Mexico. (1999).

[7] The Bendix Corp. paper, End-of Process Detection for Plasma Cleaning, Microelectronics Measurement and Test Conference, Mar. 23-24, , San Jose, Calif., (1982).

[8] Hanson et al., Optimization Chemical Vapor Deposition Processing through RF Metrology, (1999).

[9] Angra et al., Unstable Plasma Characteristics in Mirror Field Electron Cyclotron Resonance, Journal of Physics, vol. 54, No. 5, 763-769, (May 2000).

[10] Godyak, V.A., Piejak, R.B. and Alexandrovich, B.M., Electrical Characteristics of Parallel-Plate RF Discharges in Argon, IEEE Transactions on Plasma Science, vol. 19, No. 4, 660-676, (Aug. 1991).

[11] Ohsawa, Atsushi et al., Improved RF-Driven Probe Method for RF Discharge Plasma Diagnostics, Measurement Science and Technology, vol. 2, No. 8, 1, 801-806, (Aug. 1991).

[12] Godyak, V.A. and Piejak, R.B., Probe measurements of the space potential in a radio frequency discharge, Journal Applied Phys. 68 (7), 3157-3162, (1 Oct. 1990).

[13] Dupuis, Timothy J., Bocock, Ryan M., Method and apparatus for controlling the output power of a power amplifier, US Patent No. 6897730, (Mar., 2003).

[14] Coumou, David J. (Webster, NY), Weatherell, Clifford C., Kirk, Michael L., Nasman, Kevin, RF metrology characterization for field installation and serviceability for the plasma processing industry, US Patent No. 6,983,215, (December 2, 2003).

[15] Millar, Douglas James, Youn, Tai Won, Zhang, Chen (Vancouver, WA), Power detector using a constant quiescent voltage divider, US Patent No. 5,675,245, (September 15, 1995).

[16] Powell, Robert, Thermocouple power meter, US Patent No. 4,628,256, (December 9, 1986).

[17] Jackson, Robert, Portable VI probe, US Patent No. 7,102,345, (September 5, 2006).

[18] Noh, Seung-Man, Probe for measuring voltage/current of low voltage power distribution cable, US Patent No. 6,624,622, (September 23, 2003).

[19] Hopkins, Michael, Apparatus for sensing RF current delivered to a plasma with two inductive loops, US Patent No. 5,808,415, (March 19, 1997).

[20] Butterbaugh, J. W. et al., Measurement and analysis of radio frequency glow discharge electrical impedance and network power loss, JOURNAL Vacuum Science Technol., 916-923 and Erratum, 578, (Mar./Apr. 1990).

[21] Sobolewski, Mark A., Electrical characterization of radio-frequency discharges in the Gaseous Electronics Conference Reference Cell, JOURNAL Vacuum Science Technol., 3550-3562, (Nov./Dec. 1992).

[22] Sobolewski, Mark A. et al., Electrical measurements for monitoring and control of rf plasma processing., SPIE vol. 1803, 309-320. (1992).

[23] Miller, Paul et al., Beyond RF-Power Measurements, NCSL meeting, Santa Clara, 1-16, (11 Feb. 1993).

[24] Williams, Norman, Spain, James, Radio frequency monitor for semiconductor process control, US Patent No. 5,467,013, (November 14, 1995).

[25] Crook , et al., Capacitively-coupled test probe, US Patent No.5,274,336, (December 28, 1993).

[26] Ettinger, G M., Shooter, L. T. and Tillier, M., Noncontact Test Signal Acquisition, Microprocessors and Microsystems, vol. 6, No. 2, 69-71, (Mar., 1982).

[27] Benjamin, Neil, High-Impedance Capacitive Divider Probe For Potential Measurements In Plasmas, Rev. Science Instrum., vol. 53(10),1541-1543. (Oct., 1982).

[28] Willenbecher, Jr., James F., Capacitive coupled clamp-on voltage probe, US Patent No.4,090,130, (May 16, 1978).

[29] Byrne, Joshua, Ravi, Tirunelveli S., Seamons, Martin, Hanson, Eric, Chamber monitoring and adjustment by plasma RF metrology, US Patent No. 6,051,284, (April 18, 2000).

[30] Turner, Terry R. , Spain, James D., Swyers, John R., Plasma monitoring and control method and system, US Patent No.5,576,629, (November 19, 1996).

[31] Dylla, H F., Glow discharge techniques for conditioning high-Vacuum systems, JOURNAL Vacuum Science Technol. A, vol. 6, No. 3, , 1276-1287. , (May/Jun. 1982).

[32] Hopkins, M B and lawler, J F, Plasma diagnostics in industry, Plasma Phy. Control Fussion 42, B189-B197, Printed in the UK., (2000).

[33] Yakabe, Masami , Matsumoto, Toshiyuki, Hirota, Yoshihiro , Nakano, Kouichi, Impedance detection circuit, impedance detection device, and impedance detection method, US Patent No.6,756,790, (June 29, 2004).

[34] Ukai et al., Endpoint Determination of Aluminum Reactive Ion Etching by Discharge Impedance Monitoring, Journal Vacuum Science Tech. 16(2), 385-387, (1979).

[35] Plasma Etching Endpointing by Monitoring Radio-Frequency Power Systems with an Artificial Neural Network, Journal of the Electrochemical Society, 143(6), 2029-2035, (1996).

[36] Coumou, David J., Method and apparatus for radio frequency (RF) metrology, US Patent No. 6,608,446, (August 19, 2003).

[37] Seebock , RJ., Deutsch, R. and Rauchle, E., Electric current oscillations in a parallel-plate plasma reactor, Journal Vacuum Science Technol. All(3), 682-688, (May/Jun. 1993).

[38] Morgan, Russ A., Plasma Etching in Semiconductor Fabrication, 202-221, (1985).

[39] Johnson, J.D. and Holmes, A.J.T., Edge effect correction for small planar Langmuir probes, Rev. Science Instrum. 61(10), 2628-2631, (Oct. 1990).

[40] Kobayashi, K., Mutsukura, N. and Machi, Y., Electrical measurements in a 13.56 MHz radio frequency discharge, Vacuum, vol. 42, No. 12, 741-744, (1991).

[41] Godyak, V.A. and Popov, O.A., Experimental study of resonant rf discharges, Sov. JOURNAL Plasma Phys. 5(2), 227-231, (Mar.-Apr. 1979).

[42] Harp, R.S. and Crawford, F.W., Characteristics of the Plasma Resonance Probe, JOURNAL Appl. Phys., vol. 35, No. 12, 3436-3446, (Dec. 1964).

[43] Annaratone, B.M. et al., A Comparsion of a Passive (Filtered) and an Active (Driven) Probe for RF Plasma Diagnostics, Measurement Science and Technology, vol. 2, No. 8, 795-800, (1 Aug. 1991).

[44] Gilmore, J. A., Voltage and current sensor, US Patent No. 6,66,13,24, (December 9, 2003).

[45] Jeanne Cranford & team, Sematech, Radio Frequency (RF) Measurement and Control Project Report (TECQ001) (September 10, 1998).

[46] Mavretic, Anton, Method and apparatus for monitoring parameters of an RF powered load in the presence of harmonics, US Patent No. 6,04,65,94, (February 11, 1997).

[47] Heckman, Randy L., System for characterizing AC properties of a processing plasma, US Pat. No. 5,523,955, (June 4, 1996).

[48] Gerrish, K.S., Voltage-current sensor with high matching directivity, US Patent No. 6,44,95,68, (September 10, 2002).

[49] Gerrish, K.S., Voltage current sensor with high matching directivity, US Patent No. 6,70,81,23, (March 16, 2004).

CHAPTER 4

Two Digitally Correctable RF Measurement Techniques for Real Impedance Lines and Loads

4.1 Background

Accurate power measurements into real impedance lines remain the main diagnostic tool for RF applications. Real impedance is an indication that the phase between the RF voltage and the RF current is zero.

The majority of the RF generators employed for plasma processing have 50Ω output impedance. Even the exceptions are typically 50Ω RF generators (including measurement systems) followed by variable matches (variable capacitors or switched pin diode arrays add capacitors or inductors into the circuit). For non-50Ω output RF generators, power is measured into 50Ω load and calculated based on efficiency (losses) of the variable (or fixed) match (see Annex 1).

Both radio and broadcast equipment are using 75Ω impedances as the adapted line. The principle of RF measurement however remains the same;

therefore everything presented in this dissertation applies. However, the requirements for broadcast are not as stringent as in plasma applications.

I proposed, designed and tested an RF power measurement (for real impedance lines) that takes into account the source errors that were analyzed in Chapter 2. The number of components was minimized based on the consideration that fewer parts would generate fewer errors. I researched two improved versions of the analog input circuit: a modified diode detector and a new analog multiplier circuit. All circuits fed the resulting analog signal into the same digital calculation and correction block (Fig. 4.1).

4.2 Multiplier RF Power Measurement Technique

This technique is based on the fact that power is proportional to the square of the voltage or the current. Computation of the power can be done with analog circuitry, digital circuitry or a combination of analog and digital. In this particular case a commercial analog multiplier[1] was used.

The input signal is sampled by a sensor, filtered by a band-pass filter and sequentially processed by an analog and then by a digital circuit. Analog circuits are preferred because of their speed; however they are not 100% predictable. The latest generation of digital signal processors (DSP) makes real time calculation of video signals possible, opening the path to replacing fast analog circuits.

The signal processing block diagram in Fig. 4.1 illustrates the way the signal is processed. In this application, the RF sensor will deliver as input signal the forward voltage V_f and the reflected voltage V_r from a strip-line sensor.

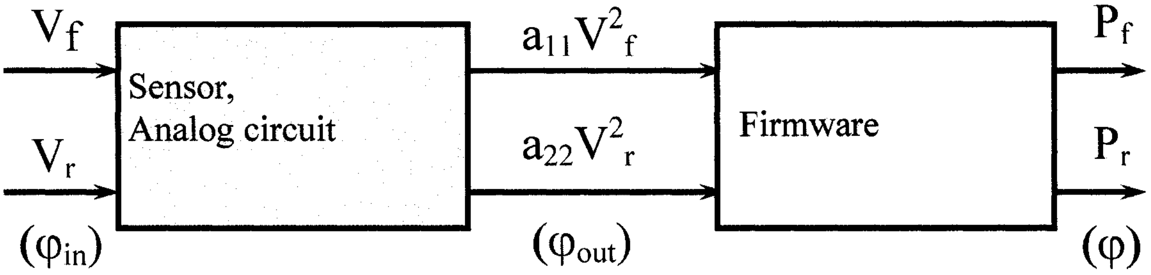

Fig. 4.1 Real Impedance Line RF Power Instrument - Signal Processing Diagram

From the mathematical point of view, the signal is processed in two steps.

The first step is to calculate the square of the forward and reflected power signals.

$$\begin{bmatrix} Vf_{out} \\ Vr_{out} \end{bmatrix} = A * \begin{bmatrix} V_f^2 \\ V_r^2 \end{bmatrix} \tag{4.1}$$

The elements of the matrix *A* are real numbers and physically correspond to an analog amplification present in the forward (a_{11}) and reflected (a_{22}) channel.

$$A = \begin{bmatrix} a_{11} & 0 \\ 0 & a_{22} \end{bmatrix} \tag{4.2}$$

The second step (digital) is to correct (calibrate) the signal.

$$\begin{bmatrix} P_f \\ P_r \end{bmatrix} = B * \begin{bmatrix} Vf_{out} \\ Vr_{out} \\ 1 \end{bmatrix} \tag{4.3}$$

Matrix *B* contains the correction information obtained either from a function or from a look-up table that was generated during calibration.

$$B = \begin{bmatrix} b_{11} & b_{12} & b_{13} \\ b_{21} & b_{22} & b_{23} \end{bmatrix} \tag{4.4}$$

Depending on the error types, the correction of the signal can take different forms. Most common are DC offset and variable gain; this correction pathway can only be used if the characteristic of the input signal is linear. The elements of the matrix *B* are real numbers:

b_{11}- Correction slope of the forward signal

b_{12}- Cross-talking correction factor (from reflected to forward channel). In an ideal case this element is 0.

b_{13}- Correction offset of the forward signal

b_{21} - Cross-talking correction factor (from forward to reflected channel). In an ideal case this element is 0.

b_{22} - Correction slope of the reflected signal

b_{23}- Correction offset of the reflected signal

Two other correction algorithms that are suitable are polynomial interpolation and an interpolation table. For more flexibility I used a correction table; therefore I employed a matrix *B* for every calibration point tested.

To eliminate the drifting hardware offset compensation I implemented a firmware auto-zero: after every ten measurements the circuit would measure the offset (short the input and measure the output) and would subtract it from the input (Fig. 4.2).

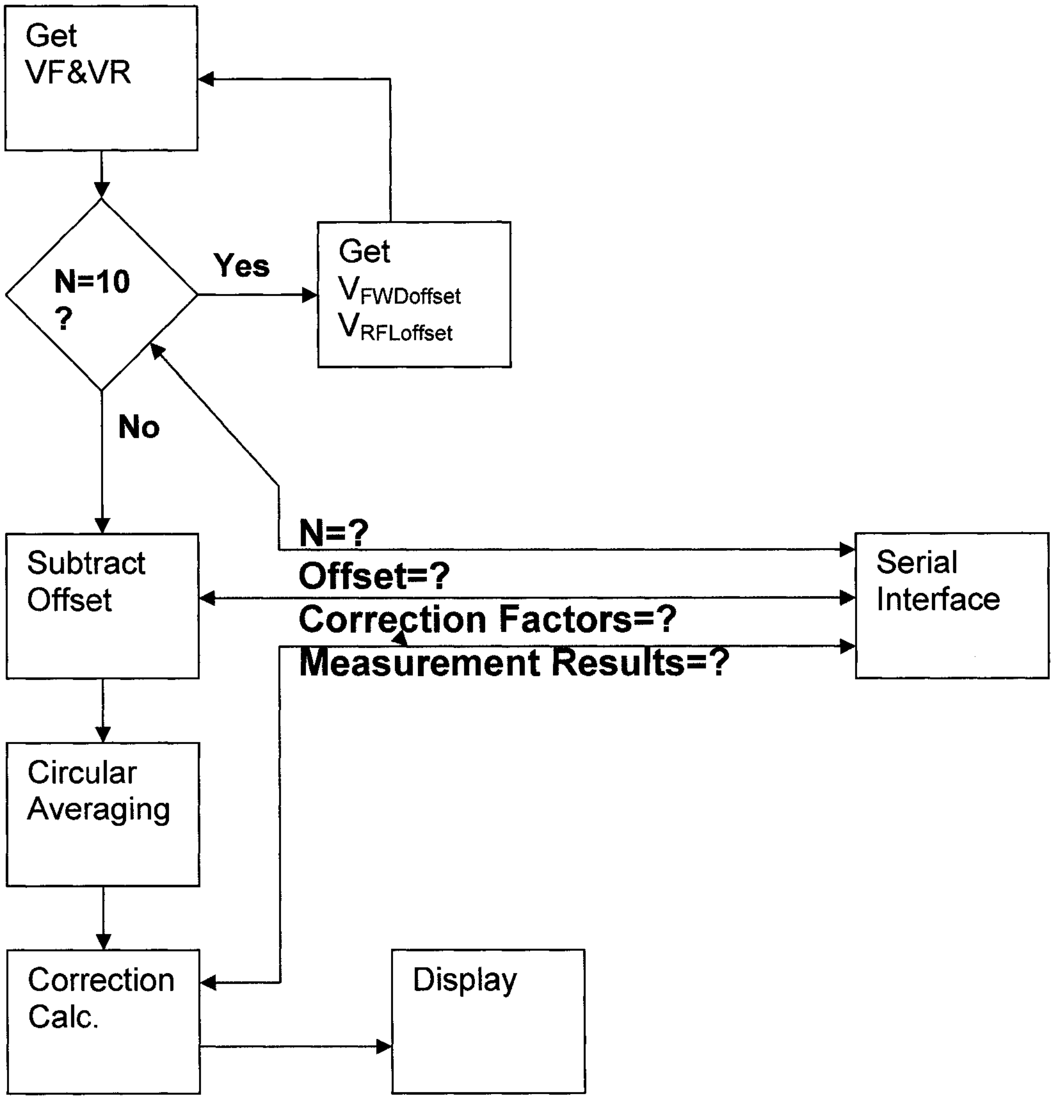

Fig. 4.2 **Real Impedance Line RF Power Instrument - Signal processing Flow Diagram**

The methodology outlined in Fig. 4.2 will remove errors due to hardware-offset drift plus will give a quantitative indication of the hardware stability with time and temperature. Next, we examine a series of experimental results employing this methodology.

4.3 Experimental Results for the Multiplier RF Power Measurement Technique

Fig. 4.3 depicts the schematic block of the proposed pathway for RF real impedance line measurement employing a stripline sensor and digital correction.

Experiments were run to measure V^2_f and the offset values at 13.56MHz for a power level up to 3000W.

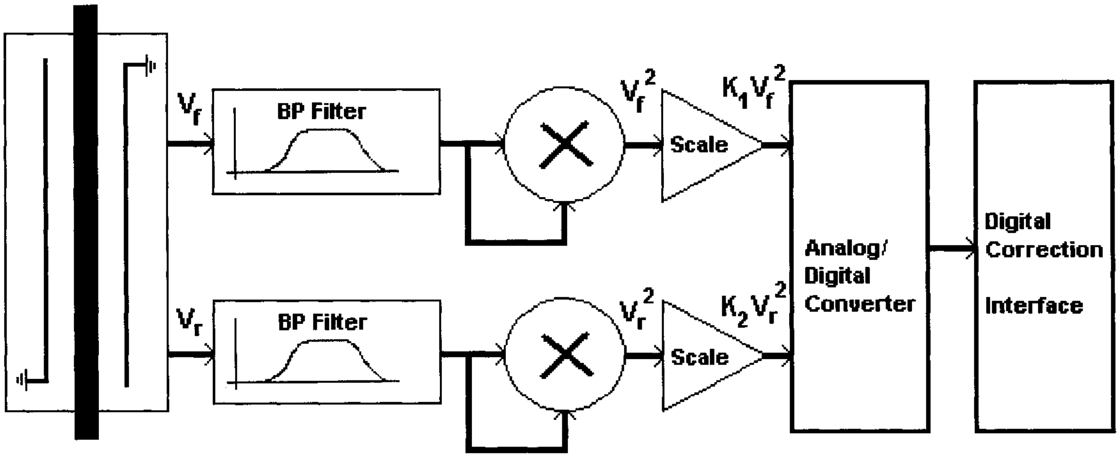

Fig. 4.3 Real Impedance Line Power Measurement Technique – Schematic Block Diagram

As a power reference I used a NIST traceable transfer standard. The topology was a 13.56MHz/3kW APEX RF signal generator followed by the Unit Under Test (UUT) and the transfer in standard into a tuned 50Ω load (Fig. 4.4).

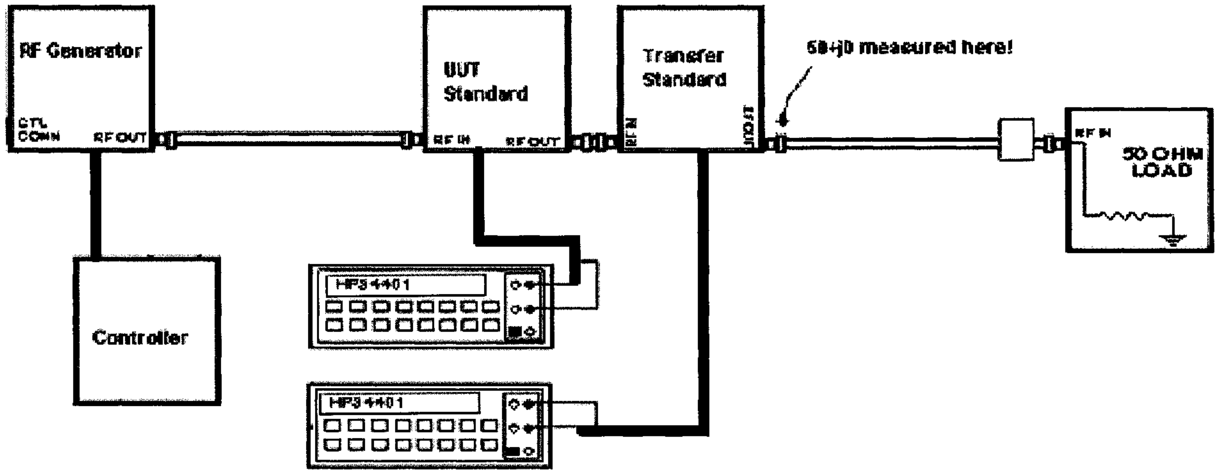

Fig. 4.4 **Experimental Setup to Evaluate the Power Error Measured in a Real Impedance Line**

The initial purpose of the experiment was to evaluate what kind of digital correction would be required for the proposed schematic block setup of Fig. 4.2 in order to achieve minimum error. This is based on a linear relationship between multiplier voltage and input power. Later, after the proper correction is set into the digital circuit, the same setup was used to check the accuracy of RF power measurement.

To evaluate the digital correction factors I varied RF power at three different RF power levels between 600W and 3000W and recorded the forward voltage output of the analog multiplier and the forward offset. In order to achieve maximum accuracy I used well-known power levels, based on the calibrated RF transfer standard.

Measurement results are presented in Table 4.1.

Table 4.1 Multiplier Voltage Out vs. RF Power In- Experimental Measurement Results

Transfer Standard (W)	UUT Multiplier Output$_{FWD}$ (V)	UUT Offset$_{FWD}$ (V)	Power Slope (W/V)
600.15	0.962	0.0304	644.21
1122.54	1.828	0.0304	624.46
2995.81	4.94	0.0304	610.19

As it can be observed in Fig. 4.5 the design using a multiplier[1-5] is a linear solution that would require just two coefficients to correct it: gain slope and offset intercept. Notice the linear interpolation factor R^2 is one (100% correlation).

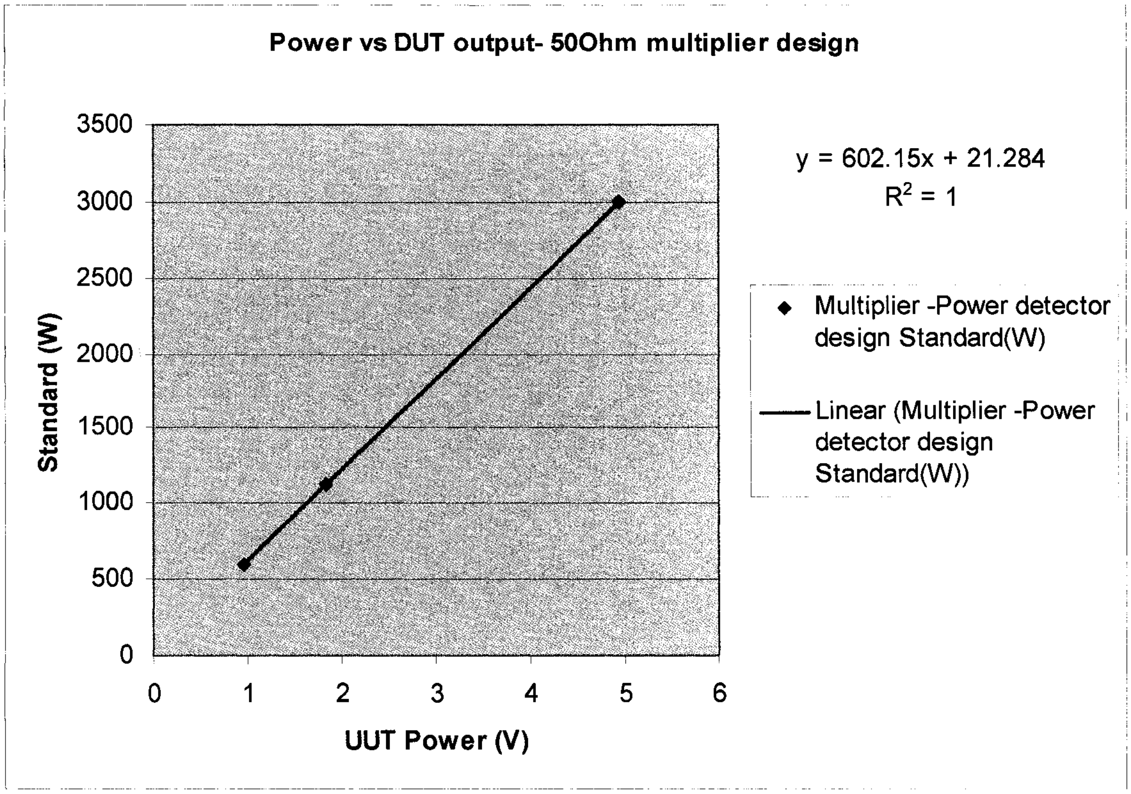

Fig. 4.5 Interpolation of the Multiplier Voltage out vs. RF Power In

Analyzing the design solely based on the analog block and in ideal load conditions (laboratory conditions) would lead to the conclusion that the power error is zero. Next we examine the multiplier circuit for various errors.

The following set of equations can describe the multiplier circuit power relationship:

$$\begin{cases} Power = Offset + V_f^2 * Slope \\ Offset = 21.284 Watts \\ Slope = 602.15 Watts / Volt \end{cases} \quad (4.5)$$

Using an A/D[6-9] with 16bit resolution would introduce a theoretical quantization error that is at least 1: 65536 from the full scale. This introduces an error due to the resolution of the A/D.

For a 3kW full scale the maximum resolution is 45mW or an equivalent error of 0.0015% from full scale.

For my comparison experiment I used an Analog Devices[1] multiplier AD835 and a Texas Instruments[6] 16bit A/D converter with a Maxim voltage reference to see the effects of addition of such circuits such as thermal drift.

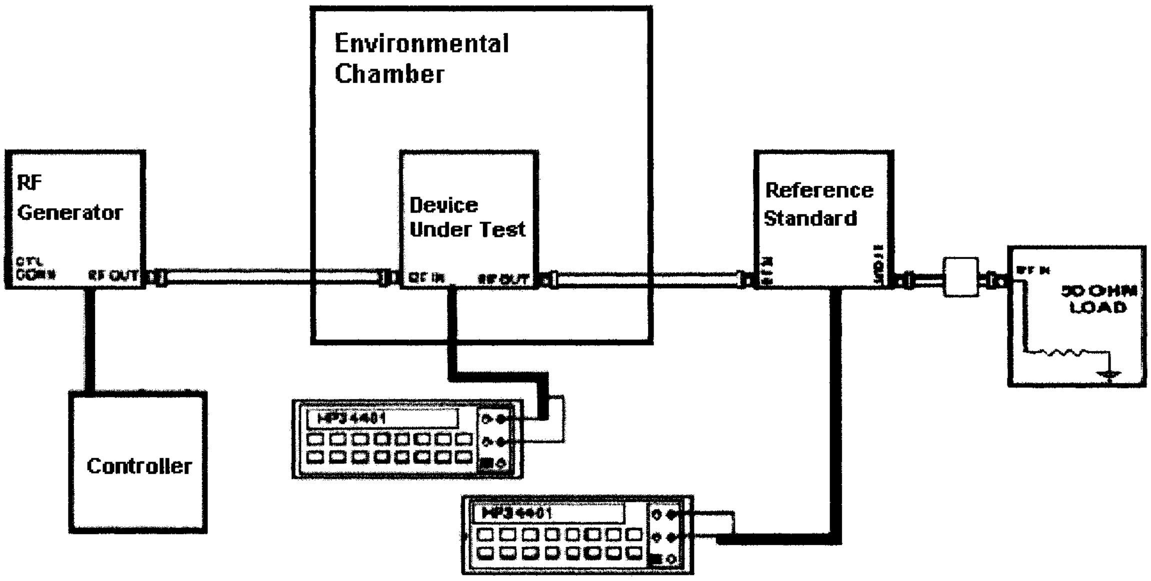

Fig. 4.6 **Setup for Thermal RF Power Drift Evaluation**

A major question related to the performance of the circuit is the temperature stability of the circuit, which has the main contributors: thermal drift of the input filter, A/D voltage reference[10-13] drift and the output multiplier drift.

The Maxim[10] Voltage reference had an advertised 15ppm/°C thermal drift. The multiplier AD835 spreadsheet was giving only an offset thermal drift; there were no mentions of any other thermal drifts.

For the thermal evaluation I used a standard environmental chamber. An ultra-stable RF signal generator fed the input of the multiplier (the stripline and input filter were not in the circuit). Analog readings of the output of the multiplier as well as the digital output of the A/D were recorded.

Input filters for both V_f and V_r signals are band-pass passive filters built with regular capacitors[20-24] and ceramic inductors[14-19] .

The inductors that I used were manufactured by Coilcraft[14] and had the following thermal specifications:

Inductor Specification

Ceramic core

+25 to +125 ppm/°C typical over operating temperature and frequency range specified in the product table.

To examine the inductance drift with the temperature we did the following:

Inductor Test method/condition

Inductors were placed in an LC oscillator circuit. The inductor was the only portion of the circuit in the environment chamber. The change in L will be indicated by the change in frequency and calculated using the following equation.

$$TCL = \frac{f_1^2 - f_2^2}{f_1^2(T_1 - T_2)}(1x10^6) \qquad (4.6)$$

I used capacitors from AVX Corporation[20] and they had the following thermal specification:

Capacitor Specification

Ceramic core

+/-100 ppm/°C from -55°C to 125°C

For my sensitivity analysis I used a pass band filter centered on 13.56MHz (Fig. 4.7). L and C values are shown for 27°C. The values of L and C at 125°C are shown in Fig. 4.9 and Fig. 4.11.

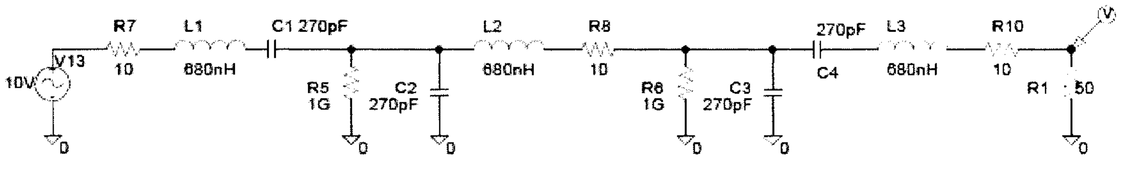

Fig. 4.7 Schematic of the Band Pass Filter simulation at 27°C

The simulation of the filter was done using PSpice[25-29]. The transfer function of the Band Pass Filter at 27°C is simulated in Fig. 4.7. Per the simulation the filter has an attenuation of the first harmonic (27.12MHz) of 21.82dB, obtained as follows:

In general we know that:

$$Atten_{2^{nd}\,harmonic} = 20\log\frac{Amplitude_{fundamental}}{Amplitude_{2^{nd}\,harmonic}}(dB) \tag{4.7}$$

For my simulations conclusions we could measure the fundamental and the 2nd harmonic values.

Likewise for 3rd harmonic:

$$Atten_{2^{nd}\,harmonic} = 20\log\frac{6.6564}{0.539327} = 21.82dB \tag{4.8}$$

$$Atten_{2^{nd}\,harmonic} = 20\log\frac{Amplitude_{fundamental}}{Amplitude_{3^{rd}\,harmonic}}(dB) \qquad (4.9)$$

Calculated data shows the 3rd harmonic attenuation:

$$Atten_{3^{rd}\,harmonic} = 20\log\frac{6.6564}{0.032369} = 46.26dB \qquad (4.10)$$

The third harmonic (40.68MHz) level is 46.26dB below the fundamental (per the simulation).

The above simulations were confirmed by measurements taken with the Network Analyzer to find measurements within 1dB of the simulations.

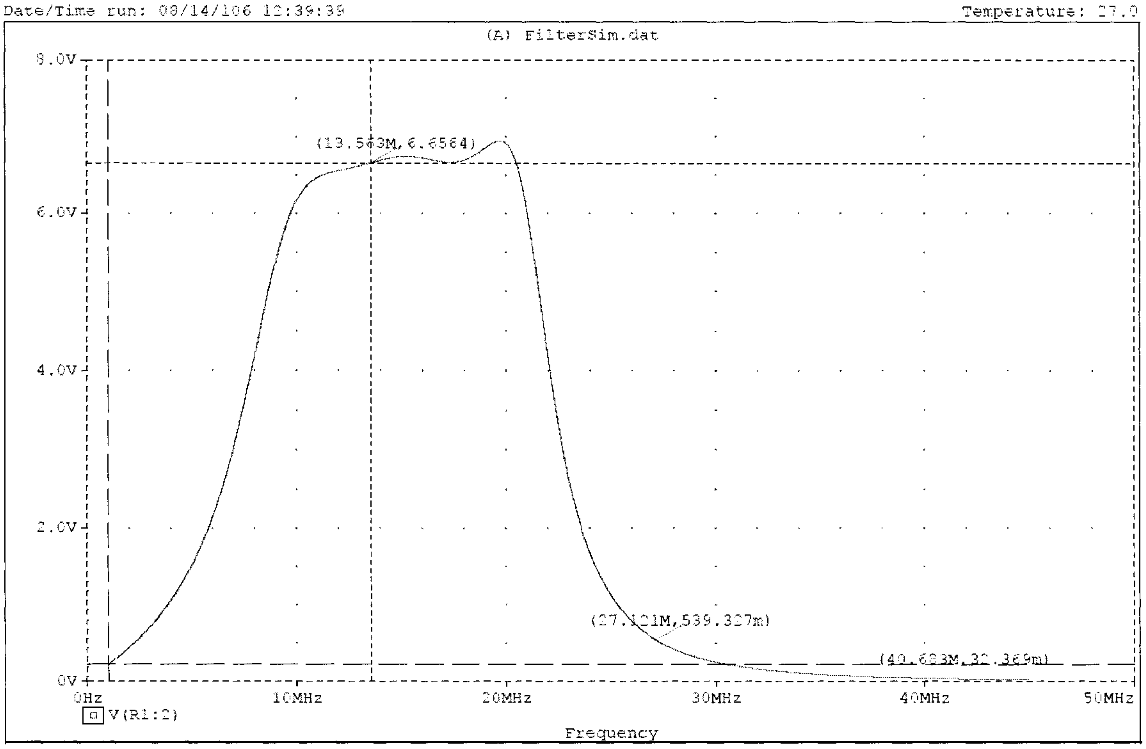

Fig. 4.8 **Transfer Function of the Band Pass Filter Simulation at 27°C**

As the next simulation step I considered that the ambient temperature would vary between 25°C and 125°C. After separately analyzing the effect of the temperature over all the filter components, I superimposed the results to see the effect on the entire filter. I considered for the inductor a drift of +100ppm/°C; therefore the overall drift of the inductor (across full temperature range) would be 1%. See Fig. 4.9 for the L values at 125°C.

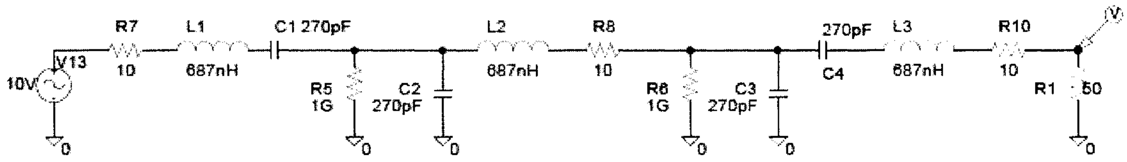

Fig. 4.9 Schematic of the Band Pass Filter with Inductors at 125°C

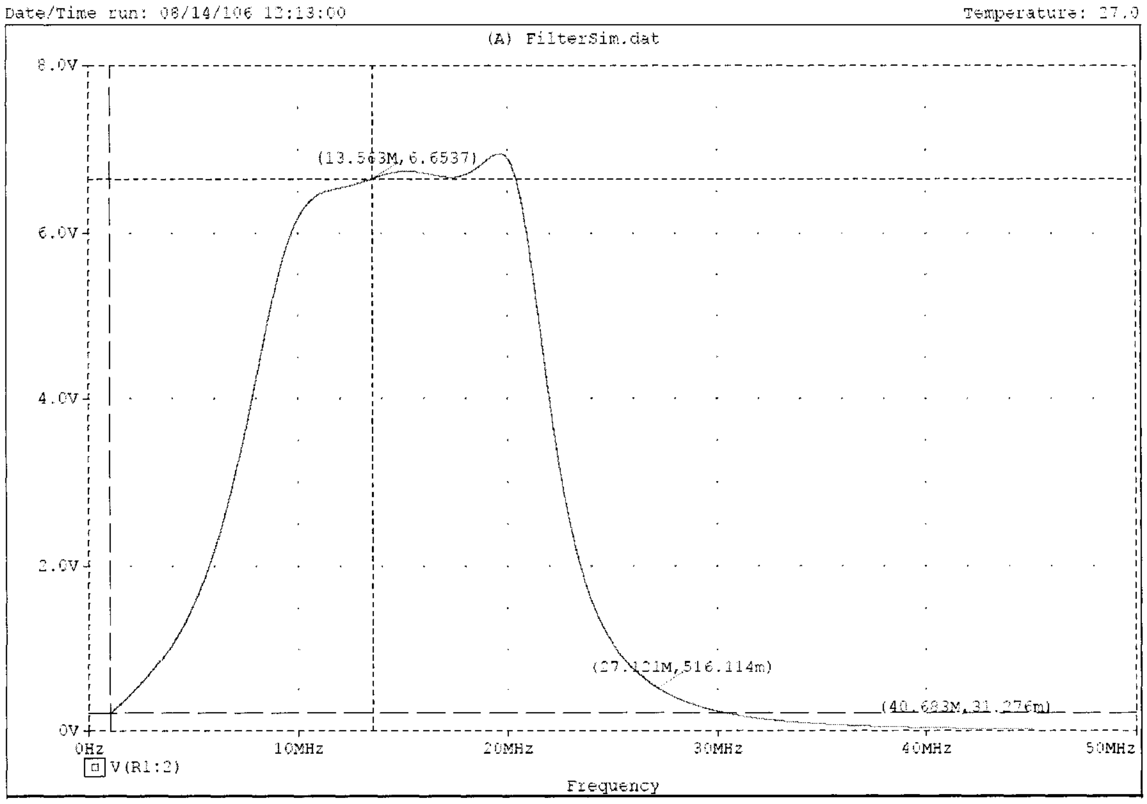

Fig. 4.10 Transfer Function of the Band Pass Filter Simulation with Inductors at 125°C

I considered for the capacitors also a drift of +100ppm/°C with a change of 1% in value over the temperature span of 25°C to 125°C. Values of C at 125°C are shown below in Fig. 4.11.

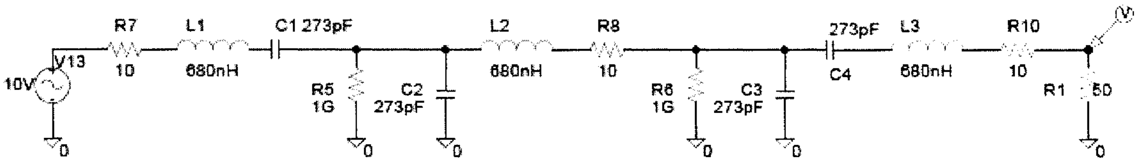

Fig. 4.11 Schematic of the Band Pass Filter with Capacitors at 125°C

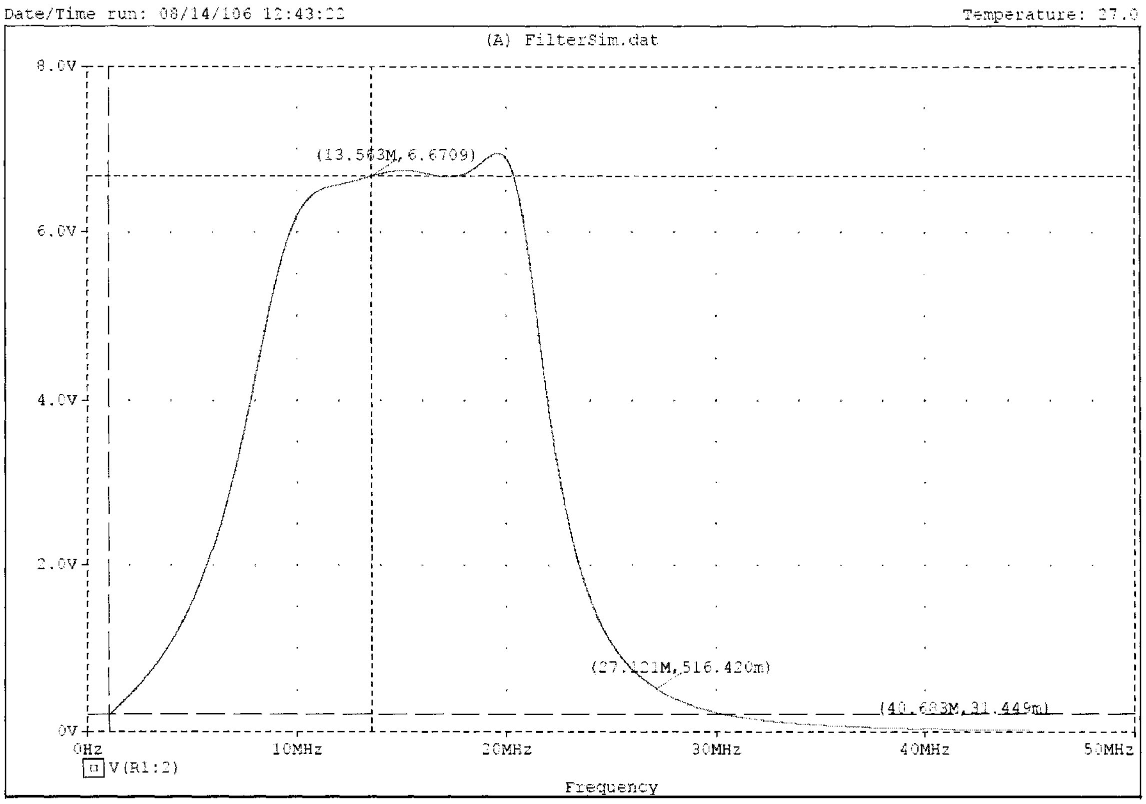

Fig. 4.12 Transfer Function of the Band Pass Filter Simulation with Capacitors at 125°C

According to the simulation, +100ppm in value change of the inductors over 100°C will produce a drift of 0.04% in signal amplitude at the fundamental 13.56MHz. The same thermal drift for the capacitors will produce 0.217% drift in signal amplitude at the fundamental 13.56MHz.

The above errors are an extreme temperature swing. In order to avoid any filter temperature drift I used Negative-Positive-Zero (NPO) capacitors and air core inductors. These types of components would give almost zero thermal drift. To double-check the hypothesis I heated and cooled (only) the filter area while a stable signal generator was connected at the input. The filter was stable under constant temperature, but it was exhibiting some drift when it was experiencing temperature transitions.

To evaluate the thermal drift for the entire circuit, such as multiplier, I used an Environmental Chamber and I set conditions as depicted in Fig. 4.6. The RF Generator, measurement equipment as well as the Reference Standard was maintained at constant temperature during the entire experiment. Only the Device Under Test was placed in the test chamber. Temperature of the Environmental Chamber was varied between 10°C and 45°C and output power from the Device Under Test was observed. Sufficient amount of time was allowed to the entire system to stabilize.

The test was run at constant 1000W at 13.56MHz. This resulted in an average drift of 0.105%/°C that was only due to the multiplier circuits placed in the stress chamber. All other parts in the circuit were zero drift or were low drift and matched.

After the thermal drift effect was loaded in the firmware the circuit was re-tested using the empirical correction.

Table 4.2 Power Error into Real Impedance Line. Test Results

Reference Standard (W)	Device Under Test (W)	Error (%)
72.81	72.76	-0.07
91.96	91.99	0.04
121.77	121.49	-0.23
164.58	164.46	-0.08
229.24	229.31	0.03
319.98	319.97	-0.00
455.46	455.77	0.07
655.86	655.73	-0.02
947.68	948.55	0.09
1377.52	1379.04	0.11
2005.67	2007.10	0.07
2926.95	2929.01	0.07

This final test results for the multiplier technique with correction are accurate and repeatable. Multiple tests did not exceed a power error of 0.3%.

4.3 Double Diode Peak Detector RF Power Measurement Technique

The classic approach to measuring RF Power is to use a diode detector/rectifier and an R-C load to peak detect the voltage proportional to the RF power. A basic approach is depicted in Fig. 4.13 but several other variations (like a combination of positive and negative peak detectors) are in use[31-39].

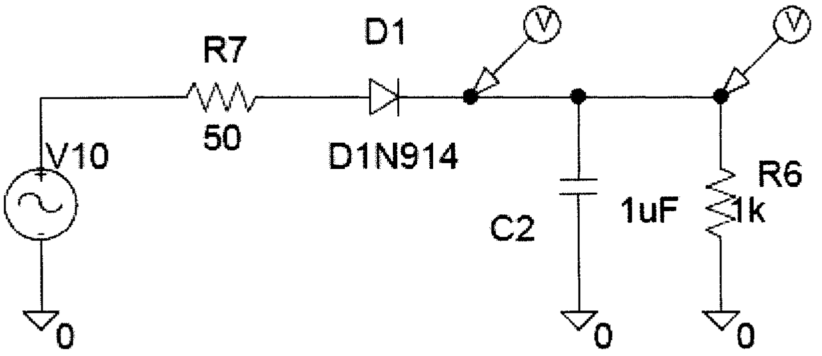

Fig. 4.13 Voltage Detector Using a Diode

The main drawback for this design is the finite threshold value (V_t)of the diode. If the input voltage does not go above the diode threshold value the output will be virtually 0V.

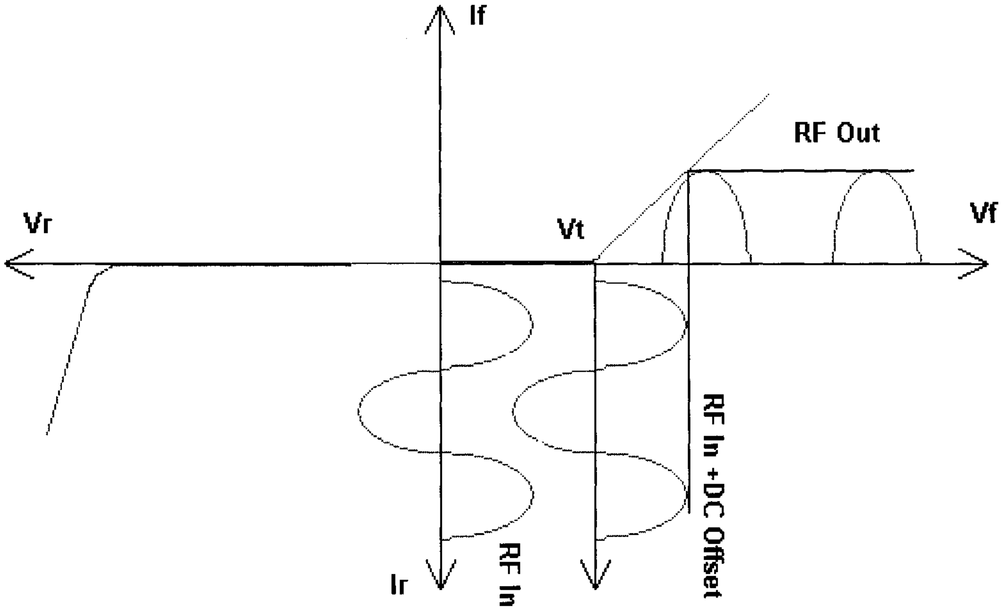

Fig. 4.14 Characteristic Output of a Diode Detector

As long as the input signal is at a relatively high level compared to V_t, the output signal is available (Fig. 4.14).

A SPICE simulation of the diode detector circuit from Fig. 4.13 at three different input RF voltages (1V, 4V, 10V) supplied the peak voltage DC results depicted in the graph in Fig. 4.15.

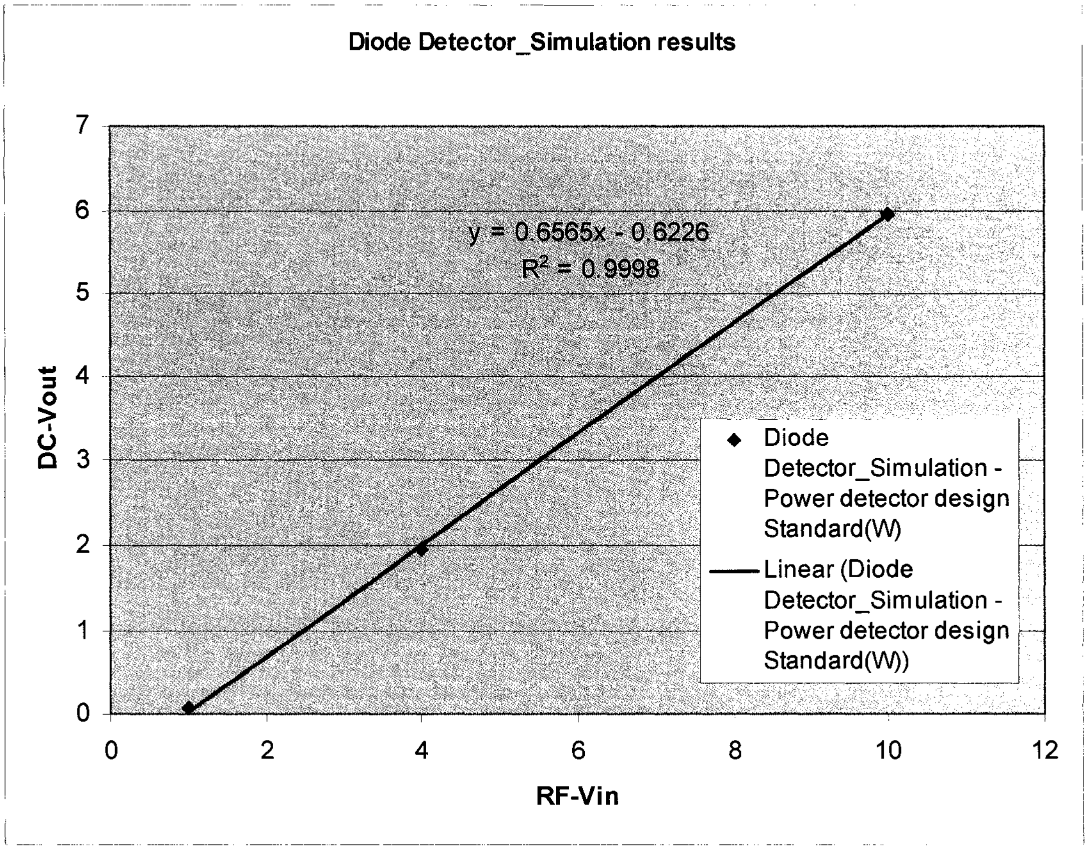

Fig. 4.15 Diode Detector Design - Output Voltage vs. Input RF

The Diode detector approach works well at input voltage levels above 1V. The low V_{RF} interpolation (Fig. 4.15) of the output signal shows little error but it also emphasis the offset. Unfortunately, the offset cannot be digitally corrected; therefore a different approach should be used for low voltage RF signal.

One variation of the diode detector is the use of the diode detector without threshold through DC bias. This solution works better but it still has limitations in frequency response.

The alternative solution that I proposed in this thesis is depicted in Fig. 4.16. Advantages of this approach are the lack of voltage offset and almost zero thermal drift.

I proposed a pair of diodes as in Fig. 4.16 biased with a DC current in order to get deep in the linear characteristic area. In DC analysis both diodes are forward biased and the voltage at pin 1 is 0VDC or very close. If we carefully match the +/-5V power supplies, the diodes V_t threshold match, and the resistors accuracy this goal can be achieved.

If we apply an RF signal at the input of the circuit (C1), because of the bias current, a voltage will also be present at the cathode of diode D1 (see Fig.4.16). The RF signal is then filtered by the capacitor C2.

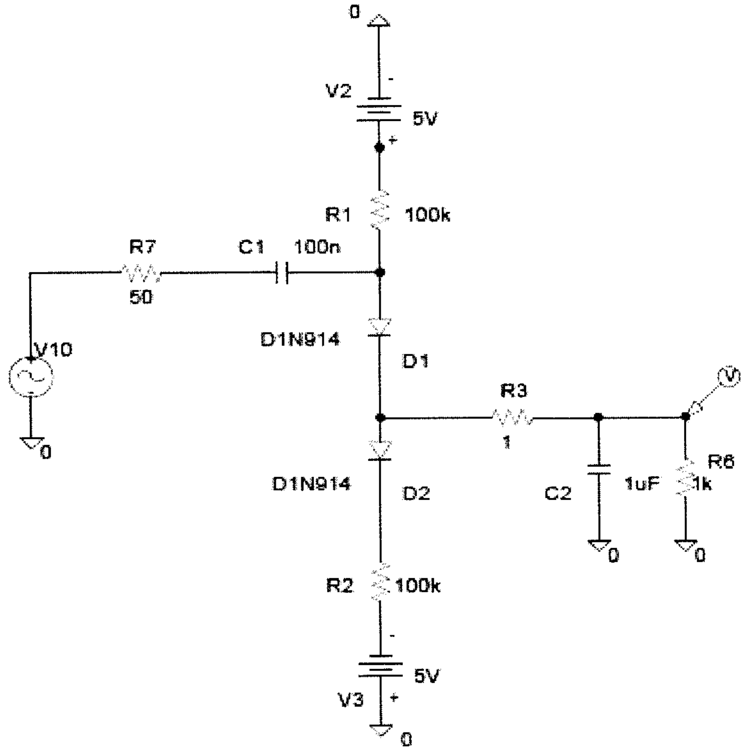

Fig. 4.16 Double Diode Detector Design- Schematic Used in Simulation

The SPICE simulation of the circuit of Fig. 4.16 confirmed that the output voltage is linear dependent on the input RF signal with no V_t offset effects as shown in Fig. 4.17.

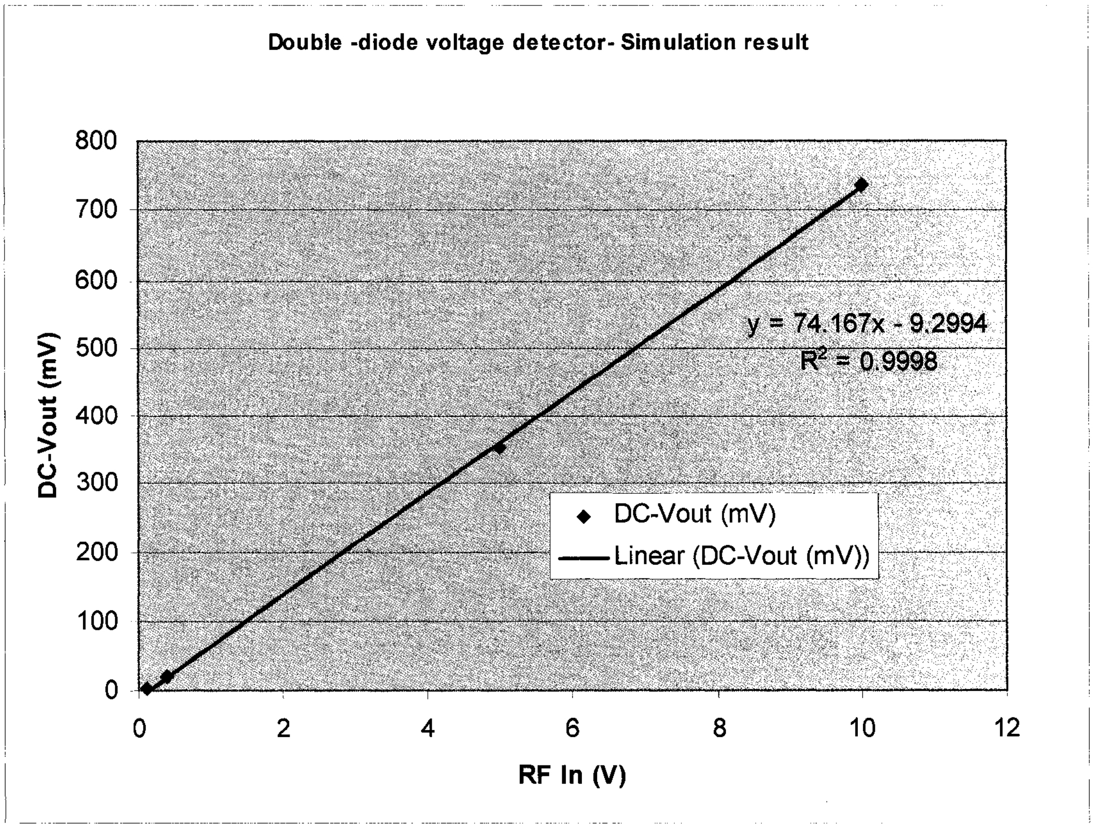

Fig. 4.17 Simulation of the Proposed Circuit Confirmed Linearity

The next step in design feasibility of the double-diode peak detector was to implement the circuit and test the performance. To achieve maximum performance, I selected a chip containing a pair of HSMS2812 diodes. The manufacturer (Avago/Agilent[30]) guarantees that the pairs are taken from the same sites on the wafer, so the performance of both diodes should be as close as possible. The diode pair was used in the voltage forward V_f and voltage reflected V_r peak detectors to achieve a threshold voltage V_t=0.

4.4 Experimental Results for the Double Diode Peak Detector RF Power Measurement Technique

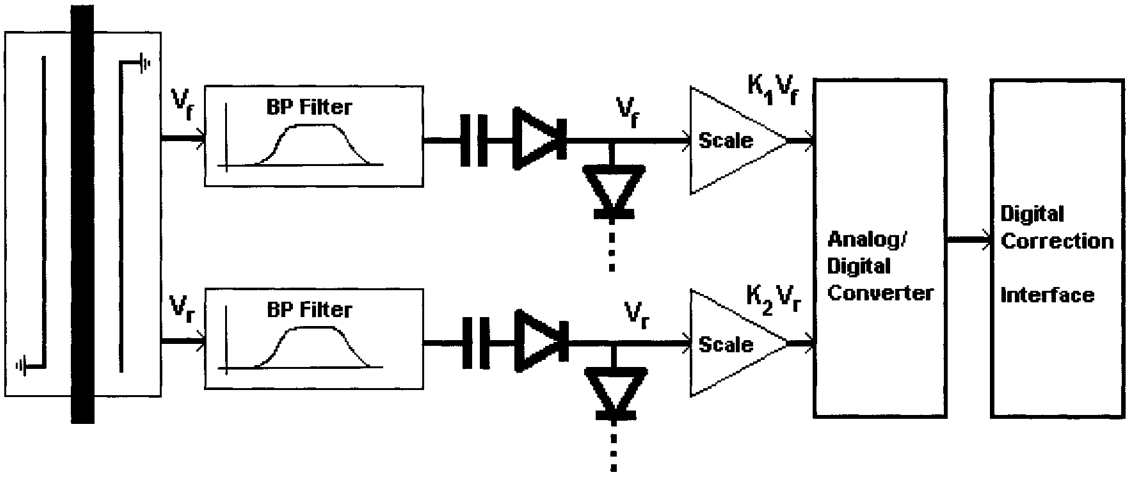

Fig. 4.18 Double Diode Peak Detector Design - Schematic Block

Unit under Test (UUT) measurements were done at 13.56MHz and with a power level up to 3000W by measuring both the peak output voltage and the DC offset.

Table 4.3 Double Diode Peak Detector Design - Test Results

Transfer Standard (W)	UUT V_{FWD} (V)	UUT Offset_{FWD} (V)	Power Slope (W/V)
600.15	2.194	0.781	300.59
1122.54	2.807	0.781	273.47
2995.81	4.268	0.781	246.38

Test results sensor UUT voltage output versus input power revealed that the circuit is not linear, but the results are still predictable using a second-degree polynomial interpolation (Fig. 4.19).

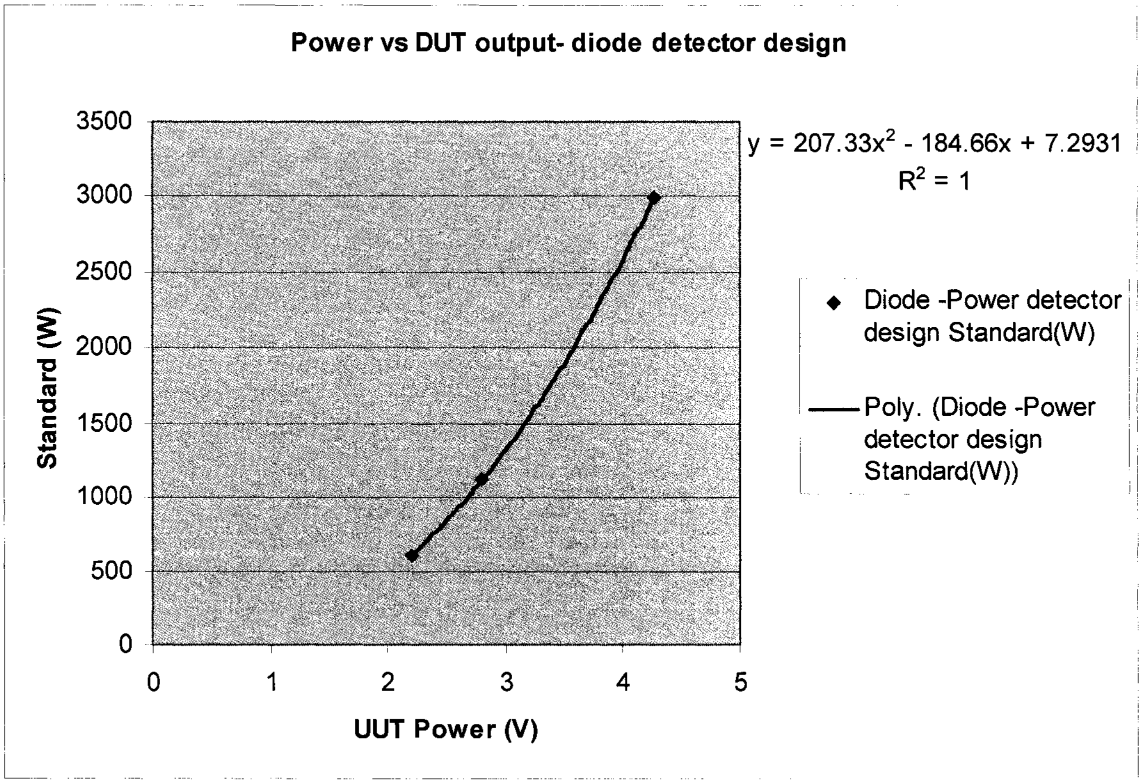

Fig. 4.19 Double Diode Peak Detector Design Circuit Voltage Output can be approximated by a Second-Degree Polynom

Empirical calculations with the test results provided the polynomial calibration coefficients a, b and offset.

$$\begin{cases} Power = aV_f^{\,2} + bV_f + Offset \\ Offset = 7.2931 Watts \\ a = 207.33 \\ b = -184.66 \end{cases} \tag{4.11}$$

4.5 Conclusions

Two methods for measuring RF power on real impedance lines were presented: zero V_t double diode peak detector and the analog multiplier method. Results are analyzed and fit to polynomials. Both techniques are suited to using three corrections to the sensor signal: a software auto-zero, lookup table correction and temperature compensation.

Because of the nature of RF circuit components it is impossible to build an analog instrument that would measure RF power with better than 1% accuracy without look-up corrections.

Using a combination of analog circuits and digital correction, an accuracy of +/-0.3% can be achieved versus a reference (transfer standard).

The largest error contributors turned out to be the temperature drift from self heating and exterior ambient temperature variations. Correction tables for temperature coefficients help maintaining the accuracy under control.

4.6 References

[1] http://www.analog.com/, Analog Multiplexers/Dividers.

[2] Gray, Paul R., Hurst, Paul J., Lewis, Stephen H., and Meyer, Robert G., Analysis and Design of Analog Integrated Circuits (4th Edition), Wiley, (Feb 15, 2001).

[3] Johns, David and Martin, Ken, Analog Integrated Circuit Design, Wiley, (Nov 15, 1996).

[4] Williams, Jim, The Art and Science of Analog Circuit Design (EDN Series for Design Engineers), Newnes, (Jul 23, 1998).

[5] Hickman, Ian, Analog Electronics, Newnes, (May 11, 1999).

[6] http://www.ti.com/, Data Converters.

[7] van de Plassche, Rudy J., CMOS Integrated Analog-to-Digital and Digital-to-Analog Converters (The International Series in Engineering and Computer Science), Springer, (May 31, 2003).

[8] Seitzer, Dieter, Electronic Analog-To-Digital Converters: Principles, Circuits, Devices, Testing, John Wiley & Sons Inc, (Jan 1984).

[9] Tang, Hua, An optimization-based methodology for top-down design of filters and analog-to-digital converters, ProQuest / UMI, (Mar 20, 2006).

[10] http://www.maxim-ic.com/ , Voltage References.

[11] Rincon-Mora and Gabriel Alfonso Rincon-Mora, Voltage References: From Diodes to Precision High-Order Bandgap Circuits, Wiley-Interscience, 1 edition, (Oct 11, 2001).

[12] Harrison, Linden T., Current Sources and Voltage References: A Design Reference for Electronics Engineers, Newnes, (Jul 20, 2005).

[13] Huijsing, Johan H., van de Plassche, Rudy J., and Sansen, Willy M.C., Analog Circuit Design: Low-Noise, Low-Power, Low-Voltage, Mixed-Mode Design with CAD Tools, Voltage, Current and Time References, Springer, 1 edition, (Dec 31, 1995).

[14] http://www.coilcraft.com/ , RF Inductors.

[15] Aguilera, Jaime and Berenguer, Roc, Design and Test of Integrated Inductors for RF Applications, Springer, 1 edition, (Mar 1, 2004).

[16] McLyman Wm. T., Transformer and Inductor Design Handbook, Third Edition (Electrical and Computer Engineering), CRC, 3 edition, (Mar 31, 2004).

[17] McLyman Wm. T, Magnetic Core Selection for Transformers and Inductors (Electrical and Computer Engineering), CRC, 2 edition,(May 5, 1997).

[18] Den Bossche, Alex Van and Cekov Valchev, Vencislav, Inductors and Transformers For Power Electronics, CRC, (Mar 24, 2005).

[19] Kaiser, Cletus J., Inductor Handbook, Cj Pub, 1st ed edition, (April 1996).

[20] http://www.avxcorp.com/, Ceramic Capacitors.

[21] Geyer, R. G., Dielectric Ceramic Materials, Transactions of the American Ceramic Society, (May 01, 1999).

[22] Cahn, Robert, Concise Encyclopedia of Materials Characterization, Second Edition: 2nd Edition Elsevier Science, 2 edition (January 25, 2005).

[23] Herbert, J. M. Ceramic Dielectrics and Capacitors (Electrocomponent Science Monographs), Routledge, (Jan 1, 1985).

[24] IEEE Standard for Series Capacitors in Power Systems (Aug 1994).

Perna, Vincent F. The RF Capacitor Handbook (American Technical Ceramics Corp), 1st edition, (1994).

[25] http://www.cadence.com/orcad/ , PSpice.

[26] Tront, Joseph G. and Tront, Joseph, PSpice for Basic Circuit Analysis, McGraw-Hill Science/Engineering/Math, 1 edition, (Mar 5, 2004)

[27] Svoboda, James A., PSpice for Linear Circuits (uses PSpice version 9.2), Wiley, Bk&CD-Rom edition, (Aug 21, 2001).

[28] Nilsson, James W., Riedel, Susan A., Nilsson, James W, and Susan A Riedel Introduction to PSpice for Electric Circuits (6th Edition), Prentice Hall, 6 edition, (Dec 21, 2001).

[29] Herniter, Marc E., Schematic Capture with Cadence PSpice (2nd Edition), Prentice Hall, 2 edition, (May 21, 2002).

[30] http://www.agilent.com/, Surface Mount RF Schottky Barrier Diodes.

[31] Vizmuller, Peter RF Design Guide: Systems, Circuits, and Equations Artech House Publishers, 1st edition (April 1995).

[32] Ramo, Simon, Whinnery, John R., Fields and Waves in Modern Radio, Second Edition, John Wiley and Sons, New York, NY, (1962).

[33] Beatty, R. W., Application of waveguide and circuit theory to the development of accurate microwave measurements and standards, Nat. Bur. Stand. (U.S.) Monograph 137, (August, 1973).

[34] Walker, D. K., Williams, D. F., Lumped-Element Impedance Standards ARFTG Conference, (June 7-12, 1998).

[35] Carr, Joseph J., How to Design and Build Electronic Instrumentation, TAB Books Inc, 2Rev Ed edition (November 19, 1986).

[36] Carr, Joseph J., Designer's Handbook Instrmtn./Contr. Circuits, Academic Press (April 28, 1991).

[37] Davies, John, Carr, Joseph J., Newnes Radio and RF. Engineer's Pocket Book, Butterworth-Heinemann, 2nd edition (May 2000).

[38] Carr, Joseph J., Elements of Microwave Electronics Technology, Harcourt (December 1989).

[39] Carr, Joseph J., The Technician's Radio Receiver Handbook, Newnes,1st edition (September 1, 2006).

CHAPTER 5

Novel RF Measurement Technique for Complex Impedance Lines and Loads: Digital Direct Sampling

5.1 Background

The RF based semiconductor manufacturing industry is characterized by the need for tight process control in order to achieve both increasingly difficult device structure geometries and higher yields.

RF measurements into real impedance lines, placed *outside* the plasma chamber, provide information about the amount of RF power delivered to the plasma *inside* the process chamber. However, other physical components of the RF plasma delivering system, like the RF match networks, can change the final result of the process (etch or deposition rate) even when the level of applied RF from the power source is the same.

In his 2003 keynote address at Advanced Equipment and Process Control (AEC/APC) XV[1], Tom Sonderman of AMD reiterated the truism that, "Your ability to control a process is directly related to your ability to measure the process."

Using RF metrology placed as close as possible to the work piece we gain better measurements and control of the RF plasma process.

There is no consensus on the precise definitions for the metrology terms: integrated metrology, in situ metrology, in situ sensors, and process and equipment sensors. This leads to considerable confusion, unless we clarify the terms.

Integrated Metrology has many uses in the control of etch and deposition processes, such as film thickness monitoring, endpoint detection of a process and a large variety of fault detection conditions that might occur during a process.

The expression "integrated metrology" is used by many in the semiconductor industry to illustrate the capability to measure a wafer feature or a wafer property that characterizes a process internal to a piece of process equipment. The term "in situ metrology" describes the same thing, although this term is frequently used to describe the capability to make the measurement directly *inside* the process chamber itself, during processing. For example, the use of in situ metrology to measure film thickness during a deposition process enables true real-time process control for a film deposition tool that seeks precise film thickness. The deposition process can be stopped as soon as the in situ metrology reports that the proper film thickness has been achieved. In this example, in situ metrology is useful when deposition rates are unstable over time or have excessive or unpredictable drifts.

If process repeatability is achieved, true in situ metrology is not required for adequate process control. Many times in situ metrology is required only for first time development of the process recipe. Once the process is stable, standalone metrology can be used in a run-to-run control methodology to correct for small drifts in future deposition runs in the same deposition/etch tool.

As a generic example, in Fig. 5.1 RF plasma conditions are monitored using current and voltage probes (measurement sensors) placed in between the variable match and the process chamber.

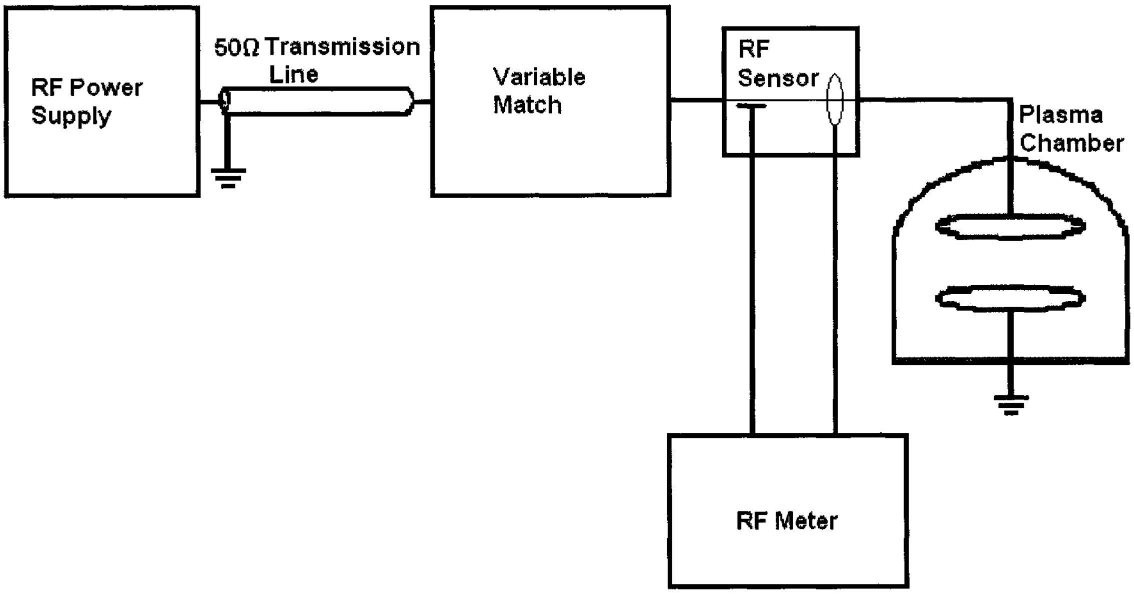

Fig. 5.1 RF Power Sensors can be Located Outside the Process Chamber

RF metrology[2-4] is also critical to fault detection during a process and chamber status. Most important tasks are the early detection of equipment or process faults such as electrode wear or undesired depositions on chamber walls.

Both RF driven etch and deposition processes require stable RF plasma conditions. Brouk and Heckman have described how plasma instabilities result from the interaction between the plasma condition and RF generator[5]. Since probing inside the plasma chamber can be more difficult, plasma control can be achieved by monitoring RF circuit parameters outside the reactor. Sobolewski discussed how total plasma ion current, electrode sheath voltage and ion energy distributions impinging on the wafer could be determined by measuring the RF external current and voltage delivered to the biased chamber electrode[6].

The RF measurement technique presented in this chapter classifies as external to the plasma chamber. The external RF method is enabled by advancements in Digital Signal Processors as detailed below.

5.2 Theory of the Direct Digital Sampling RF Measurement Technique

The method proposed for measurement characteristics in complex impedance environment can be categorized as a direct digital sampling method if compared to all previous methods, which employ mostly analog circuits. The drawbacks of analog based methods were related to complexity, lack of accuracy at high VSWR, uncontrollable thermal drift and the difficulty to calibrate.

Direct digital sampling technique acquires in parallel both input signals (V_f and V_r or V and I) and process them entirely digitally. The advantages of this method are the reduced number of analog circuits, stability and easy of frequency agility. Digital direct sampling works at different frequencies without hardware changes as long as fast A/D hardware is available. The direct sampling method is mostly used in GPS radio receivers[7 - 11](radar, satellite) applications but lately has also been used on RF instrumentation[12, 13].

There is a one to one mathematical relation between the Forward Voltage/Reflected Voltage (V_f/V_r) pair of signals and the RF line Voltage/Current (V/I) pair. Hence the same downstream RF measurement algorithm can be used with either a V/I sensor pair or a directional coupler providing V_f and V_r. The choice between front-end sensors depends on the particular application. In general, a V/I RF sensor is a better choice for measuring low impedance loads.

The hardware schematic block (Fig. 5.2) of the method analyzed in this chapter contains three basic blocks: an RF sensor (directional coupler or V/I sensor), an analog circuit (filter and scale the signal for maximum dynamic) and a digital circuit for calculating both impedance and power as well as for I/O signals (2 channel parallel A/D and a Digital Signal Processor).

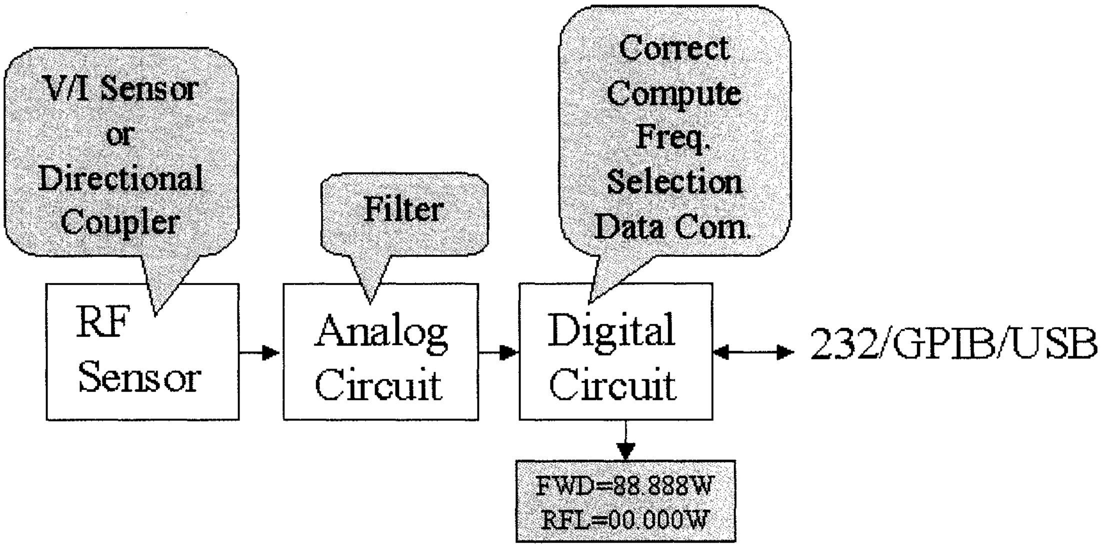

Fig. 5.2 Hardware Schematic Block of the Direct Digital Sampling RF Measurement Technique

The RF signal is acquired thru the input sensor and analog scaled and filtered before input of the A/D. The analog filtering is optional because a frequency selection is implemented into the digital signal processor. However, the undersampling technique requires an analog band-pass filter, as it will be explained later.

A major contributor to the errors is expected to be the angle (phase) between the input signals (V_f and V_r or V and I). Typically the amplitude of the signals is not an issue and can be calculated and calibrated accurately.

From a signal processing point of view, the schematic block diagram of direct digital RF measurement for a strip-line sensor is represented in Fig. 5.3.

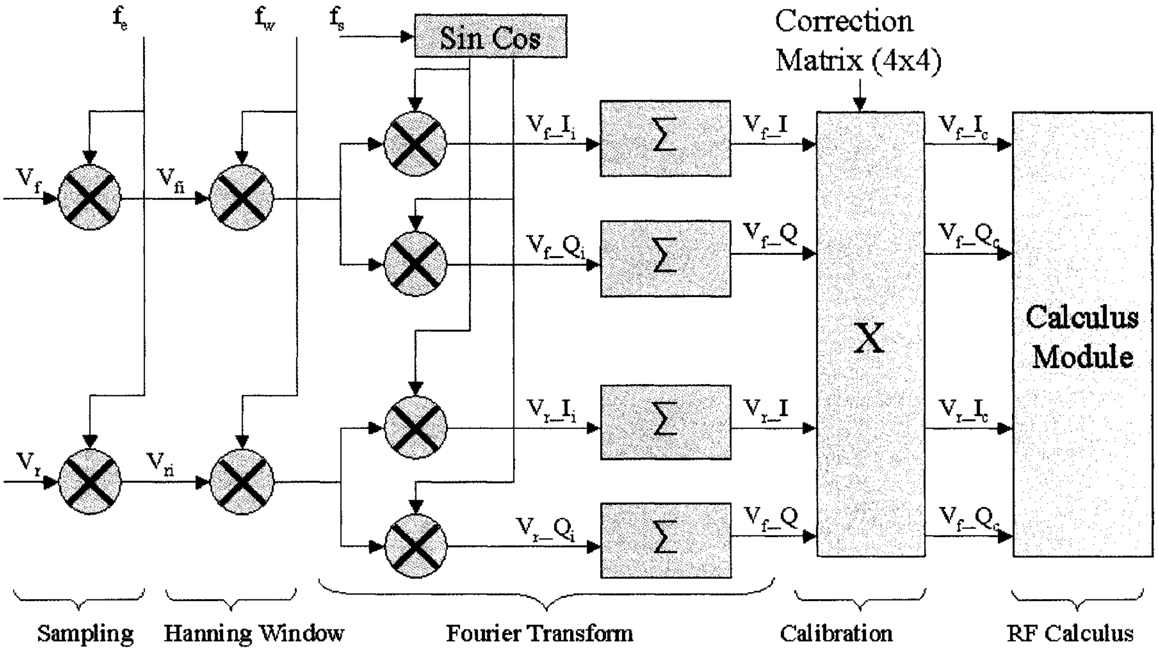

Fig. 5.3 Signal Processing Schematic Block for Direct Sampling

The RF input signal is sampled as fast as possible (there is a hardware limitation but undersampling technique is possible) followed by a windowing function (Hann window). The signal goes then thru a Discrete Fourier Transform. The output signals are kept in complex form and a correction or calibration matrix may be applied. Output of the correction matrix is an accurate representation of the sampled signals (V_f and V_r). A final math block will calculate any RF information (RF power, voltages, currents, impedance).

The Fourier Transform[14, 15] is the core signal methodology used to process the signal for my application, therefore I am going to present all the aspects related to this key step.

5.2.1 Fourier Transform for Continuous Functions

For a continuous waveform f(t) with the highest frequency component f_h, the Fourier Transform[16] F(f) will be defined mathematically as:

$$F(f) = \int_{-\infty}^{\infty} f(t)e^{-j\omega t}dt = R(f) + jI(f) \tag{5.1}$$

F(f) is a complex function with boundary conditions 5.2.

$$F(f) = 0 \text{ for} |f| > f_h = 0 \tag{5.2}$$

The condition for alias-free sampling at digital rate f_s (in waveform samples per second) will be then:

$$f_s > 2f_h \tag{5.3}$$

f_s is traditionally called Nyquist rate or $f_h < f_s / 2$ where f_h is the Nyquist frequency. This inequallity is essential to meet as I will demonstrate later. If the sampling frequency f_s is exactly twice and not greater then the bandwidth of the input signal, then phase mismatches between the sampler and the signal can still dramatically distort the measured signal. For example, sampling a signal defined by cos(πn) at t=0, 1, 2, ...will give you the discrete signal cos(πn), as expected. However, sampling the same signal at t=0.5, 1.5, 2.5,... will give you a constant zero signal. These two sets of samples, which differ only in ampling phase and not in frequency of sampling, give dramatically different results because they sample *at* the critical frequency, instead of strictly *above* the critical frequency. This result provides a clear rationale for meeting the strict inequality of the sampling condition, and is the reason why the sampling rate must allways exceed the critical frequency.

The time interval between successive approximations is a constant and is referred as the sampling interval. It is typically given in seconds as:

$$T = \frac{1}{f_s} \tag{5.4}$$

The Fourier inverse transform is mathematically defined as:

$$f(t) = \int_{-\infty}^{\infty} F(f) e^{j\omega t} dt \tag{5.5}$$

where j is the square root of -1 and e denotes the natural exponent

$$e^{j\omega t} = \cos(\omega t) + j\sin(\omega t) \tag{5.6}$$

$$e^{-j\omega t} = \cos(\omega t) - j\sin(\omega t) \tag{5.7}$$

In general the Fourier Transform, in frequency space, is a complex quantity:

$$F(f) = R(f) + jI(f) = |H(f)| e^{j\omega(f)} \tag{5.8}$$

$R(f)$ is the real part of the Fourier Transform and $I(f)$ is the imaginary part of the complex Fourier Transform.

$|H(f)|$ is the absolute amplitude of the Fourier spectrum and is given by the relation:

$$|H(f)| = \sqrt{R^2(f) + I^2(f)} \tag{5.9}$$

$\omega(f)$ is defined as the phase angle of the Fourier Transform at frequency f and is given by the relation:

$$\omega(f) = \tan^{-1}\left(\frac{I(f)}{R(f)}\right) \tag{5.10}$$

Each of the above mathematical functions represents various forms of the continuous Fourier Transform. However, for digital signal processing applications (like the one discussed on this dissertation) the continuous Fourier transform is not employed. Rather a particular case is employed. The Discrete Fourier Transform (DFT) is discussed below.

5.2.2 Discrete Fourier Transform (DFT)

Digital processing requires both digital sampling and a discrete way of manipulating the measured data. The Discrete Fourier Transform[17 - 20] is the mathematical method employed to process discrete waveform data in order to obtain the spectral image of the input waveform. The final result of the DFT is physically correct and similar to the continuous Fourier Transform if a series of conditions and restrictions (discussed below) are met.

Applying the change in the limits of integration to the Fourier Transform formula 5.11 we obtain expression 5.12.

$$F(f) = \int_{-\infty}^{\infty} f(t) e^{-j\omega t}\, dt \tag{5.11}$$

$$F(k) = \frac{1}{P}\int_{0}^{P} f(t) e^{\frac{-j2\pi kt}{P}}\, dt \tag{5.12}$$

If the signal is repetitively sampled with a period *T* during a time window *P* for a finite number of samples N, then the DFT representation becomes:

$$\begin{cases} F(k) = \dfrac{1}{NT}\sum_{n=0}^{N-1} x(n) e^{\frac{-j2\pi knT}{NT}} T \\ t \leftarrow nT \\ dt \leftarrow T \\ P = NT \end{cases} \tag{5.13}$$

Unlike the integral form of the continuous Fourier Transform, the Discrete Fourier Transform will have the frequency spectrum representing a discrete collection, usually referred as frequency bins. Some information, contained in the f(t), may be lost if the frequency bins are not selected correctly.

For my application, the signal f(t) that I am analyzing is sinusoidal and has a known frequency, therefore this error (discrete frequency bin or "picket fence error") is not present. If the continuous time signal f(t) is represented by *N* samples x(n), sampled with a period *T*, then the DFT function X(k) is represented by:

$$X(k) = \frac{1}{N}\sum_{n=0}^{N-1} x(n) e^{\frac{-j2\pi kn}{N}} \tag{5.14}$$

with k=0,1, 2,..., N-1. Rearranging the power of "*e*" term in equation 5.14 to emphasis the frequency (instead of "bin number") by multiplying by *P/P* we obtain:

$$X(f) = \frac{1}{N}\sum_{n=0}^{N-1} x(n) e^{\frac{-j2\pi kn\overbrace{NT}^{P}}{NP}} \tag{5.15}$$

If we substitute the expression for the period *P* and we use the notation $\omega = 2\pi f$ we obtain:

$$X(f) = \frac{1}{N}\sum_{n=0}^{N-1} x(n)e^{-j\omega nT} \tag{5.16}$$

Here nT is the discrete moment in time when the input signal x(t) is sampled and termed x(n). If we substitute the conventional mathematical expression 5.17 in the formula 5.16 we obtain the form of the discrete signal as a sum of trigonometric functions 5.18.

$$e^{-j\omega nT} = \cos(\omega nT) - j\sin(\omega nT) \tag{5.17}$$

Then the DFT be represented as:

$$X(f) = \frac{1}{N}\sum_{n=0}^{N-1} x(n)\left[\cos(\omega nT) - j\sin(\omega nT)\right] \tag{5.18}$$

$$X(f) = \frac{1}{N}\sum_{n=0}^{N-1} x(n)\left[\cos(\omega nT)\right] - j\frac{1}{N}\sum_{n=0}^{N-1} x(n)\left[\sin(\omega nT)\right] \tag{5.19}$$

x(n) is the “n” sample of the input signal and *N* is the number of samples.

To avoid complicating the simple physical understanding of what happens to the discrete signal when is processed I am not going to include at this point in the math the effects of sampling and Hann window (see the convolution paragraph).

Key to the signal processing for RF measurement is that V_f and V_r voltages are both parallel sampled; therefore the phase information (between the channels) is kept constant. Following the signal-processing path both discrete signals are multiplied by sin and cos.

Let us assume that the V_f and V_r signals from the directional coupler are:

$$\begin{cases} V_f = A\sin(\omega_S t + \varphi_f) \\ V_r = B\sin(\omega_S t + \varphi_r) \end{cases} \tag{5.20}$$

By choosing to parallel sample both signals, the phase difference φ is going to be a constant φ=constant between the V_f and V_r signals, even as the phase of the load changes.

$$\varphi = \varphi_f - \varphi_r \tag{5.21}$$

A local (digital) sin/cos function generator (see Fig. 5.3) will provide the proper values for multiplication to recreate the equation 5.19 sample by sample. Note that the generated values correspond to a signal that has the same frequency as the input signal. Both "sin" and "cos" functions values are calculated for the exact same time interval and the same time (so they would not change the difference in phase of the input signals V_f and V_r).

Indices t_i represent the precise moment in time when the signal f(t) was sampled. This moment corresponds also to a sample number (within the observation window) $t_i = nT$. Following the signal processing from Fig. 5.3, as a result of the multiplication of the input V_f and V_r sampled signals with the "cos" and "sin" functions we obtain equation 5.22. Indices "*i*" from V_{fi} signifies the "*i*" digital sample of the V_f analog forward signal. Similar notation is used for the V_r signal.

$$\begin{cases} V_f\_I_i = V_{fi} * \sin(\omega_S t_i) \\ V_f\_Q_i = V_{fi} * \cos(\omega_S t_i) \end{cases} \tag{5.22}$$

I used the notation of $V_f\_I_i$ for the digital sample that is multiplied with “sin” and $V_f\_Q_i$ as the expression for the digital sample that was multiplied by “cos” function. The notation is similar (and has the same meaning) to generic I –Q signals that are considered orthogonal (from phase point of view).

If we substitute the values of the signal V_{fi} we get for the forward channel:

$$\begin{cases} V_f\_I_i = A\sin(\omega_S t_i + \varphi_f) * \sin(\omega_S t_i) \\ V_f\_Q_i = A\sin(\omega_S t_i + \varphi_f) * \cos(\omega_S t_i) \end{cases} \quad (5.23)$$

Using trigonometric manipulation we obtain the pair of equations 5.24 for the forward DFT:

$$\begin{cases} V_f\_I_i = \frac{A}{2}\left[\cos\varphi_f - \cos(2\omega_S t_i + \varphi_f)\right] \\ V_f\_I_i = \frac{A}{2}\left[\cos\varphi_f - \cos(2\omega_S t_i + \varphi_f)\right] \end{cases} \quad (5.24)$$

Similar calculation is done for the RFL channel to find the reflected DFT pair of equations:

$$\begin{cases} V_r\_I_i = \frac{B}{2}\left[\cos\varphi_r - \cos(2\omega_S t_i + \varphi_r)\right] \\ V_r\_Q_i = \frac{B}{2}\left[\sin\varphi_r + \sin(2\omega_S t_i + \varphi_r)\right] \end{cases} \quad (5.25)$$

The next step for DFT calculation is finding the sum of all the discrete samples over the length of the observation window:

$$\begin{cases} V_f\_I = \frac{1}{N}\sum_{i=0}^{N-1} Vf\_I_i \\ V_f\_Q = \frac{1}{N}\sum_{i=0}^{N-1} Vf\_Q_i \end{cases} \quad (5.26)$$

The sum will become:

$$\begin{cases} V_f\_I = \dfrac{A}{2N}\sum_{i=0}^{N-1}\left[\cos\varphi_f - \cos(2\omega_S t_i + \varphi_f)\right] \\ V_f\_Q = \dfrac{A}{2N}\sum_{i=0}^{N-1}\left[\sin\varphi_f + \sin(2\omega_S t_i + \varphi_f)\right] \end{cases} \tag{5.27}$$

The leakage effect is attenuated by the proper observation window – Hanning function window. Then we know that the signal was sampled at regular intervals and both sums ($\sum_{i=0}^{N-1}\cos(2\omega_s t_i + \varphi_f)$ and $\sum_{i=0}^{N-1}\sin(2\omega_s t_i + \varphi_f)$) are zero in expression 5.28 and 5.29. The zero summing of these two terms is guaranteed either by employing coherent sampling or by using a Hanning observation window as it will be demonstrated later in the thesis.

$$\frac{A}{2N}\sum_{i=0}^{N-1}\cos\varphi_f - \underbrace{\frac{A}{2N}\sum_{i=0}^{N-1}\cos(2\omega_s t_i + \varphi_f)}_{0} = \frac{A}{2}\cos\varphi_f \tag{5.28}$$

$$\frac{A}{2N}\sum_{i=0}^{N-1}\sin\varphi_f - \underbrace{\frac{A}{2N}\sum_{i=0}^{N-1}\sin(2\omega_s t_i + \varphi_f)}_{0} = \frac{A}{2}\sin\varphi_f \tag{5.29}$$

So far, for the forward channel we find the equation pair 5.30:

$$\begin{cases} V_f\_I = \dfrac{A}{2}\cos\varphi_f \\ V_f\_Q = \dfrac{A}{2}\sin\varphi_f \end{cases} \tag{5.30}$$

Similar results follow for the reflected channel with the equation pair:

$$\begin{cases} V_r\_I = \dfrac{B}{2}\cos\varphi_r \\ V_r\_Q = \dfrac{B}{2}\sin\varphi_r \end{cases} \tag{5.31}$$

Observe that on both channels the results carry the information about the phase and amplitude of the input signal.

Up until to this level of processing the signal was arranged in a convenient form. Both amplitude and phase are corrupted by errors due to several factors: the way the signal was sampled, non-ideal components, printed circuit board layout (cross talking) or digital processing itself. As long as all these factors have a constant predictable influence over the measuring system we can correct for all of them. The easiest way is to use a linear correction. From the way the signal is processed we can notice that the output amplitude of the "I" and "Q" components are linear dependent with the input V_f:

$$\underbrace{V_f\_I_c}_{digital\_processed\_signal} = \underbrace{K}_{coefficient} * \underbrace{V_f}_{input\_signal\_amplitude} \tag{5.32}$$

The conclusion is that scaling the input signal up/down will also determine a proportional (linear) variation of the processed signal; explicitly the RF power scaling can be done only by a proportional factor. This is introduced in the formulas as "*K*", an amplitude-scaling coefficient.

There are four signals in the Calibration block (see Fig. 5.3) and four signals coming out. The mathematical relation between input and output of the calibration block is defined by expression 5.33.

$$\begin{bmatrix} V_f\_I_c \\ V_f\_Q_c \\ V_r\_I_c \\ V_r\_Q_c \end{bmatrix} = Kx\begin{bmatrix} a11\_a12\_a13\_a14 \\ a21\_a22\_a23\_a24 \\ a31\_a32\_a33\_a34 \\ a41\_a42\_a43\_a44 \end{bmatrix}x\begin{bmatrix} V_f\_I \\ V_f\_Q \\ V_r\_I \\ V_r\_Q \end{bmatrix} \tag{5.33}$$

There are no DC input signals to the A/D so I can define the calibration matrix A as in expression 5.34.

$$A = \begin{bmatrix} a11\_a12\_a13\_a14 \\ a21\_a22\_a23\_a24 \\ a31\_a32\_a33\_a34 \\ a41\_a42\_a43\_a44 \end{bmatrix} \tag{5.34}$$

Any DC input signal would add an extra offset term a15 as:

$$V_f\_I_c = Kxa11xV_f\_I + Kxa12xV_f\_Q + Kxa13xV_r\_I + Kxa14xV_r\_Q\text{+a15} \tag{5.35}$$

The final math for the calibration block can be summed in the 5.36 system of equations.

$$\begin{cases} V_f\_I_c = Kxa11xV_f\_I + Kxa12xV_f\_Q + Kxa13xV_r\_I + Kxa14xV_r\_Q \\ V_f\_Q_c = Kxa21xV_f\_I + Kxa22xV_f\_Q + Kxa23xV_r\_I + Kxa24xV_r\_Q \\ V_r\_I_c = Kxa31xV_f\_I + Kxa32xV_f\_Q + Kxa33xV_r\_I + Kxa34xV_r\_Q \\ V_r\_Q_c = Kxa41xV_f\_I + Kxa42xV_f\_Q + Kxa43xV_r\_I + Kxa44xV_r\_Q \end{cases} \tag{5.36}$$

In an ideal case, when no calibration would be required, the matrix “A” is diagonal with elements “1” and “0”.

$$A = \begin{bmatrix} 1\_0\_0\_0 \\ 0\_1\_0\_0 \\ 0\_0\_1\_0 \\ 0\_0\_0\_1 \end{bmatrix} \tag{5.37}$$

Based on this observation we can conclude then the other elements of the matrix “A” are measuring the cross talk between the forth channels and they would be close to zero for an ideal design.

Another interesting aspect of this method is the rejection of other frequencies. We can specify the frequency bin we want to observe by changing the mixing frequency f_S (see Fig. 5.3). An analogy would be the analog heterodyne circuit where you can select the probe mixing frequency to keep the intermediate frequency constant and tuned to the low frequency input amplifier.

There are four elements as input to the correction matrix and four elements as output. We also take into consideration any possible cross talking (that any element can influence any other element) therefore the size of the correction matrix should be 4x4. Some of the terms may be redundant (for example term "a" has a symmetric effect on term "b" and "b" has the same effect on "a"), but as a general form the matrix has a maximum of 16 independent elements.

5.2.3 The Fast Fourier Transform

In 1965 Cooley and Tukey published their abbreviated mathematical algorithm which has become known as the "Fast Fourier Transform[21]". The Fast Fourier Transform (FFT) is a computational algorithm that greatly reduces computing time and hence makes the Fourier Transform more real time possible. In my application I did not used the Fast Fourier Transform, but I think it is worth mentioning as an alternative.

It must be pointed out that the FFT is not a different transform from the DFT, but rather just a means of computing the DFT with a considerable reduction in the number of calculations required.

While it is possible to develop FFT algorithms that work with any number of points, maximum efficiency of computation is obtained by constraining the number of time points to be an integer power of two, e.g. 1024 or 2048.

5.2.4 Approximation of Continuous Fourier Transforms with the DFT

The approximations involved when using the DFT[22 - 26] in the analysis of continuous time systems must be carefully understood. There are problems that arise in the process that may lead to erroneous results unless proper precautions are taken.

While the mathematical properties of the DFT are exact, the DFT itself is seldom of interest as the end goal. The DFT is usually used to approximate the Fourier Transform of a continuous time process, and it is necessary to understand some of the limitations inherent in this approach.

There are three possible phenomena that result in errors between the DFT computed and the true Fourier Transform. The three major phenomena are (a) *aliasing*, (b) *leakage*, and (c) *the picket-fence effect*.

(a) *Aliasing*. One solution to the aliasing problem is to ensure that the sampling rate is high enough to avoid any spectral overlap, or to use an *anti-aliasing filter*. This is considered common digital knowledge but there are ways around it. Special considerations to aliasing are given in the undersampling chapter of this dissertation.

(b) *Leakage*. This problem arises because of the practical requirement that we must limit observation of the signal to a finite interval. The process of terminating the signal after a finite number of terms is equivalent to multiplying the signal by a *window function*. The net effect is a distortion of the spectrum.

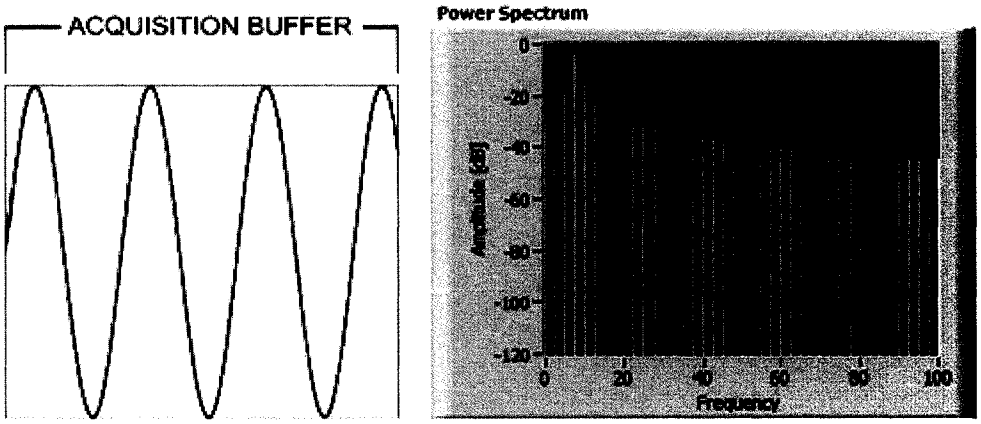

Fig. 5.4 Measuring a non-integer number of periods adds spectral leakage to the FFT

However, the leakage is NOT present if the window of observation is a multiple of the period of the observed signal. This is a relatively difficult condition to meet, but not impossible. Some authors are using the term "coherent sampling" for this technique.

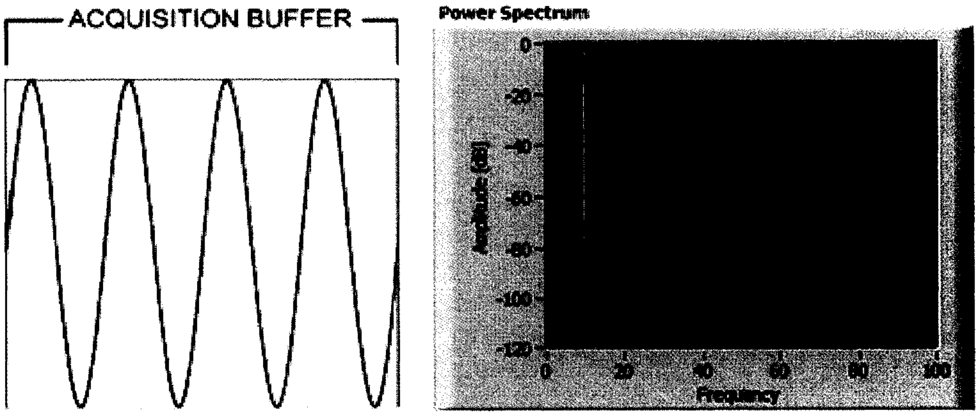

Fig. 5.5 Measuring an integer number of periods gives ideal FFT

One way to alleviate the leakage effect is to use a special window of observation. We have to employ a time domain truncation function that has side-lobe characteristics smaller in magnitude then those of the $\frac{\sin(f)}{f}$ function; which is the Fourier Transform of a regular window of observation.

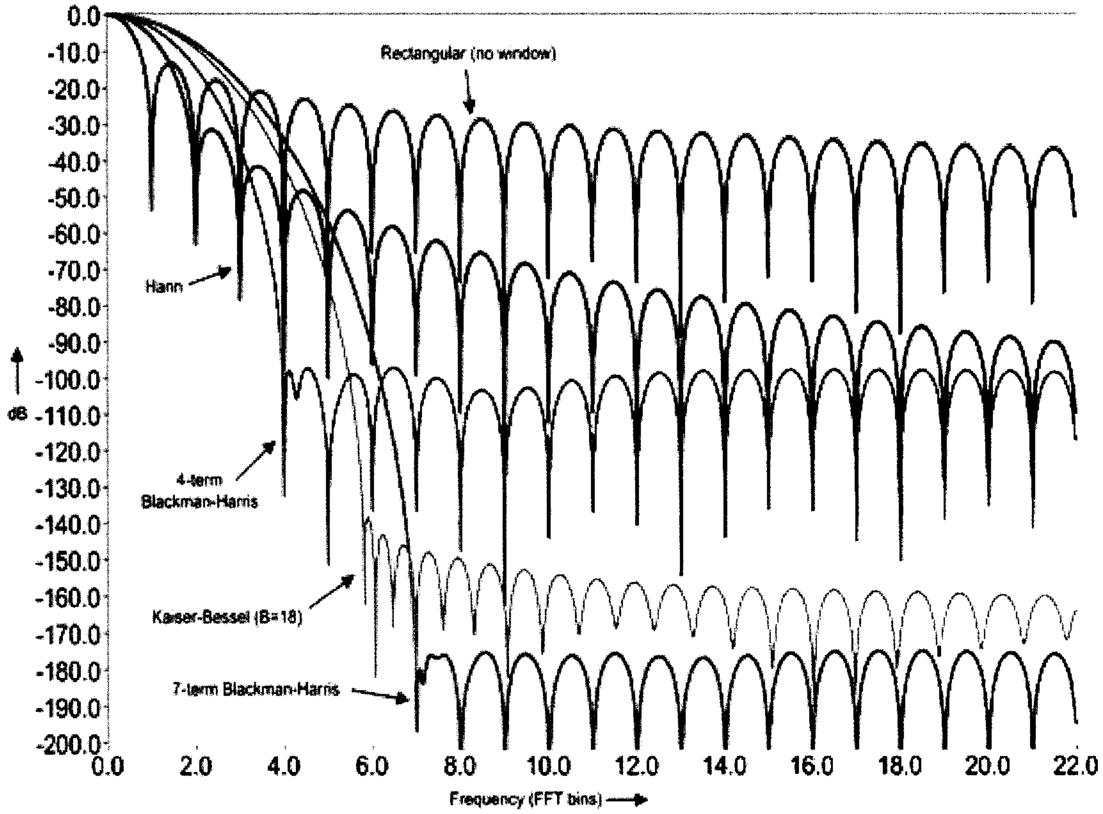

Fig. 5.6 Representation in frequency of common type of sampling windows

One option for the observation window, to alleviate the leakage effect, is the Hanning function:

$$x(t) = \frac{1}{2}\left[1 - \cos(\frac{2\pi t}{Tc})\right] \tag{5.38}$$

Tc is the length of the observation window; $0 \le t \le Tc$.

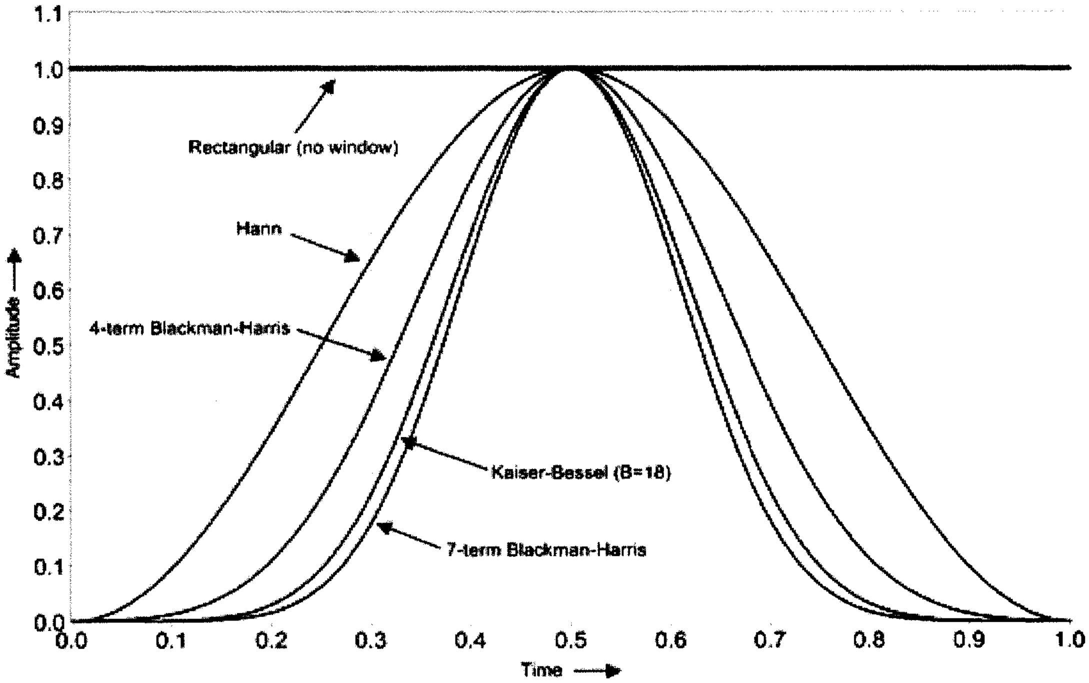

Fig. 5.7 Representation in time of different type of sampling windows

(c) *Picket-Fence Effect.* This effect is produced by the inability of the DFT to observe the spectrum as a continuous function, since computation of the spectrum is limited to integer multiples of the fundamental frequency f. Observation of the spectrum with the DFT is analogous to looking at it through a sort of "picket-fence," since we can observe the exact behavior only at discrete points. The major peak of a particular component could lie between two of the discrete transform lines, and the peak of this component might not be detected without some addition processing.

To summarize this section, the DFT algorithm can be used to approximate the transform of a continuous time function, subject to the following limitations and difficulties.

The signal must be band limited, and the sampling rate must be sufficiently high to avoid aliasing. For computational purposes it is necessary to limit (in time) the length of the signal. As a consequence of the limited observation time the spectrum will be degraded somewhat by the leakage effect. Leakage is most severe when the simple rectangular window function is used.

Components lying between discrete frequency lines are subject to error in magnitude due to the "picket-fence" effect.

5.2.5 Undersampling Effect

The undersampling effect can be found in the literature under several different names: sub-sampling, harmonic sampling, bandpass sampling or super-Nyquist Sampling.

From Nyquist criteria we know that we have to digitize a signal at a frequency (called the Nyquist frequency) that is at least twice the bandwidth of the signal (some authors would wrongfully mention “twice the signal frequency”). In the baseband signals case the bandwidth and the maximum frequency that can be analyzed are the same.

There are cases when we are constrained by existing hardware limitations. For example, the speed of the A/D converters is not high enough to acquire the input signal. One solution to the hardware limitation is the undersampling method.

The answer is that we can acquire signals at higher frequencies than Nyquist frequency if several precautions are taken into consideration.

To properly discuss undersampling the term of non-based bandwidth has to be clarified. The *baseband bandwidth* is equal to the highest frequency of a signal or system, or an upper bound on such frequencies. By contrast, the *non-baseband* bandwidth is the difference between the highest frequency and the nonzero lowest frequency. A good example is the FM radio where the signal is ranging from 88MHz to 108MHz. This can be considered as a non-baseband signal with a bandwidth of 20MHz; therefore it can be sampled with a sampling frequency above 40MHz.

Perhaps an easier explanation to undersampling follows changes in frequency rather than time.

We know that sampling a signal f(t) at a frequency Fs is equivalent to a convolution in frequency (analog to a frequency mixer). On the frequency axis we will see the presence of the Fs+f(t) and Fs-f(t). This pair of mixed frequencies are repeated every n*Fs, where “n” is the “n” harmonic.

The same mix of frequencies happens in the case of undersampling, but this time we are using one of the harmonics of the sampling frequency (this is why some authors are using the term harmonic sampling). Since this is true for any harmonic it is obvious that we have to use a bandpass filter (at the input of the A/D) to reject any other frequencies that may result into images across our field of interest.

To include the undersampling case, the Nyquist theorem must be restated as follows:

Let $0<f_L<f_H$ be the lower and higher boundaries of a frequency band of a signal, then there is a non-negative integer N and a sampling frequency f_s that will satisfy simultaneously the following conditions :

$$\begin{cases} 2(f_H - f_L) < f_s \\ N\dfrac{f_s}{2} < f_L \\ (N+1)\dfrac{f_s}{2} > f_H \end{cases} \tag{5.39}$$

If we reduce the above statement for a baseband signal then $f_L=0Hz$ and N=0, therefore the condition is going to be reduced to $f_s>2f_H$ (that is the Nyquist alias-free sampling condition).

As an example let's consider the FM radio band to illustrate the idea of undersampling.

An FM radio is operating in the band from $f_L=88MHz$ to $f_H=108MHz$ with a total bandwidth of:

$$W = f_H - f_L = 20MHz \tag{5.40}$$

According to the undersampling conditions mentioned before, the following requirements must be met simultaneously:

$$\begin{cases} 2(f_H - f_L) = 40MHz < f_s \\ N\frac{f_s}{2} < f_L = 88MHz \\ (N+1)\frac{f_s}{2} > f_H = 108MHz \end{cases} \tag{5.41}$$

Using the result from the first equation and solving the second inequation gives us N<4.4. If we proceeding with N=4 then we get the expressions 5.42 for sampling frequencies boundaries.

$$\begin{cases} f_s < \frac{2*88MHz}{4} = 44MHz \\ f_s > \frac{2*108MHz}{5} = 43.2MHz \end{cases} \tag{5.42}$$

with an interval of sampling frequencies as set of solutions

$43.2MHz < f_s < 44MHz$.

Any acceptable solutions are for N=1, 2, 3, 4. If we select N=3 then the solutions for the sampling frequencies are:

$$\begin{cases} f_s < \frac{2*88MHz}{3} = 58.66MHz \\ f_s > \frac{2*108MHz}{4} = 54MHz \end{cases} \tag{5.43}$$

with an interval of sampling frequencies as set of solutions

$54MHz < f_s < 58.66MHz$. Of course, the last solution (using N=3) is not the best optimization as a higher speed A/D has to be used.

Note that when undersampling a real-world signal, the sampling circuit must be fast enough to capture the highest signal frequency of interest. Theoretically, each sample should be taken during an infinitesimally short interval, but this is not practically feasible. Instead, the sampling of the signal should be made in a short enough interval that can represent the instantaneous value of the signal with the highest frequency. This means that in the FM radio example above, the sampling circuit must be able to capture a signal with a frequency of 108 MHz, not 43.2 MHz. Thus, the sampling frequency may be only a little bit greater than 43.2 MHz, but the input bandwidth of the system must be at least 108 MHz.

If the theorem is misunderstood to mean twice the highest frequency, then the required sampling rate would be assumed to be greater than the *Nyquist-frequency* 216 MHz. While this does satisfy the last condition on the sampling rate, it is grossly oversampled.

Some A/D converters are specifically characterized for undersampling, while others are designed only for baseband sampling. The analog signal path of the A/D converter must handle the input frequencies with minimum distortion. The A/D clock jitter is a concern and can generate some signal indetermination (error).

5.3 Experimental Results for the Direct Digital Sampling RF Measurement Technique

Fig. 5.8 depicts the schematic block of the proposed RF measurement solution for RF complex impedance line and loads measurement. The signal sensor is a directional coupler that is feeding the forward and reflected voltage into a dual channel A/D.

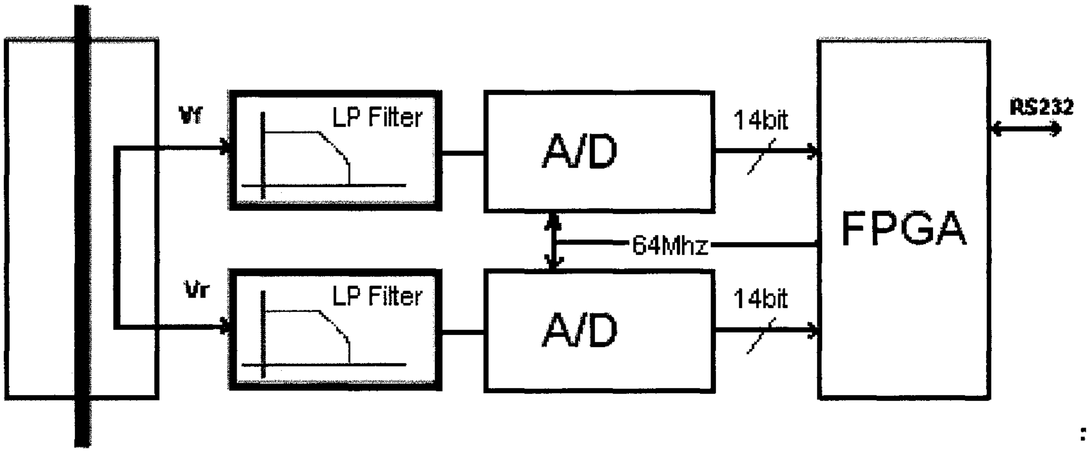

Fig. 5.8 **Schematic Block for the Direct Digital Sampling Technique**

A one-pole low pass filter (25Ω+12pF) is used to attenuate any undesired high frequency signals. The input circuit (Fig. 5.9), including the input filter, is specified by the A/D manufacturer. Other configurations are possible (including a high speed single-input to differential output operational amplifier).

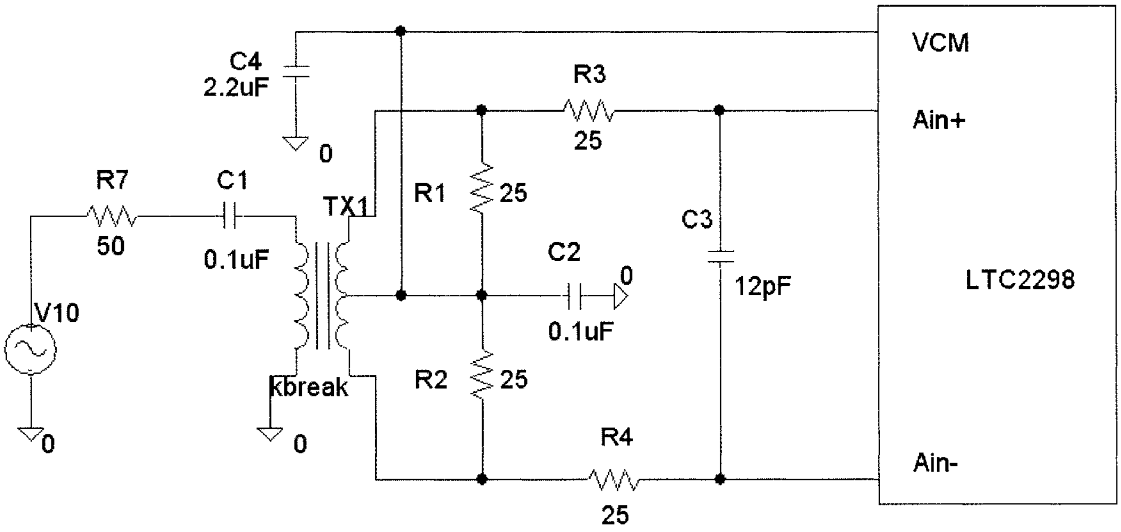

Fig. 5.9 **Input Circuit for Direct Digital Sampling Technique**

Both clocks of the A/D were connected together for true parallel sampling. The manufacturer is mentioning sampling speeds up and above 300MHz; therefore this chip is a good candidate for undersampling. Because of low values of the track-and-hold capacitors (4pF) there is a limitation at low frequencies; in this particular case it is 1MHz.

Tests were conducted using a 13.56MHz generator with power levels up to 3kW. The circuit was loaded with a variable match that covered impedances up to 5:1 VSWR.

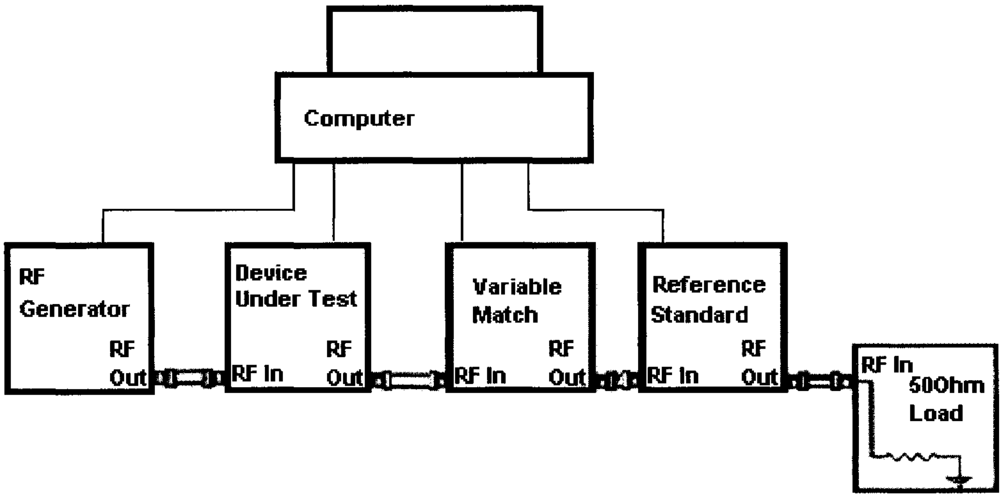

Fig. 5.10 Test Setup for Direct Digital Sampling Technique

The variable match impedance and the efficiency variation (using the method presented in Annex 1) were mapped using an impedance analyzer. One concern was the difference in impedance at low power (using impedance analyzer) and at high power. The design of the variable match had to be optimized (range vs. efficiency) to achieve efficiency as high as possible. Careful design of the match delivered efficiency in excess of 95% even at high VSWR.

Since the direct sampling measurement method is linear with power, the calibration process itself can be done at low powers (to further minimize the thermal effects).

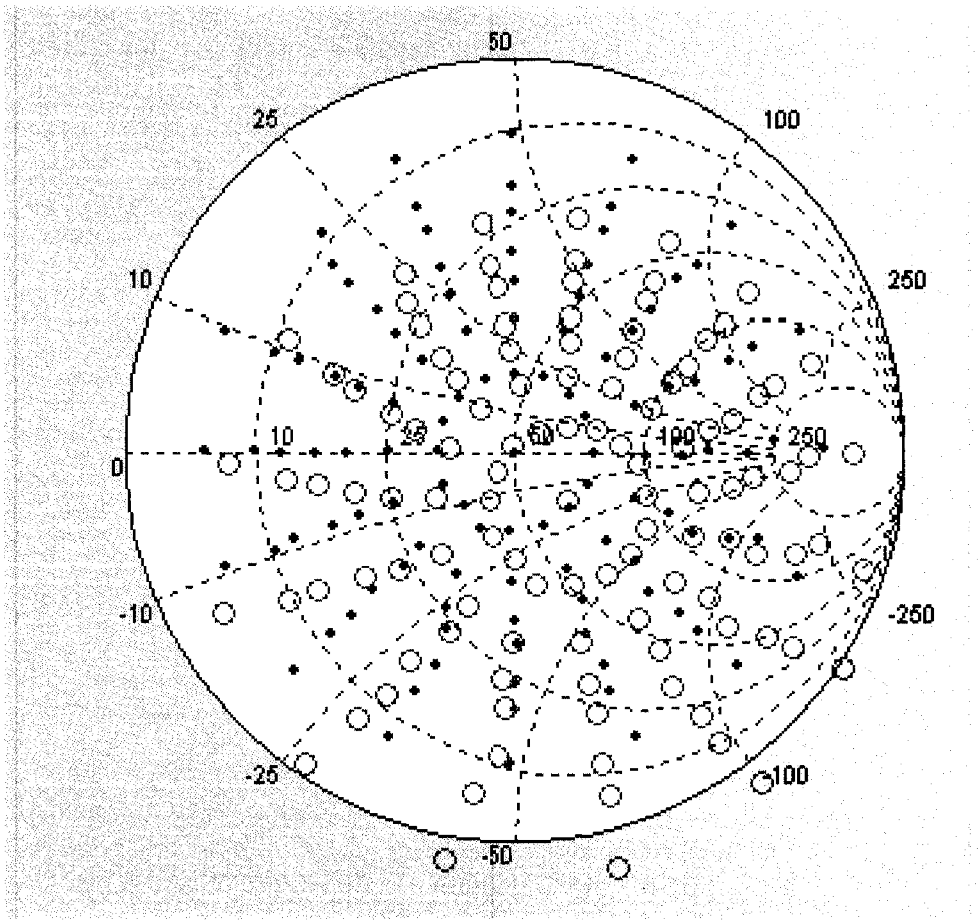

Fig. 5.11 Impedance Accuracy of the Circuit with Default Calibration Factors (Before Calibration)

Based on previous tests a set of calibration coefficients (default values) were loaded on the DSP. Fig. 5.11 displays the impedance values measured by the device before calibration versus real impedances. The red dot represents the true impedance (as measured by Network Analyzer) and the green circles are the values reported by the direct digital sampling device under test. Notice that the relative distribution of the impedances is similar but affected by an offset. The calibration process was done at 300W. The match impedance was changed to 113 positions, including 50Ω. The values reported by the device under test were recorded along with the power levels reported by the W-Meter connected to 50Ω load.

The calibration process created a set of 113 equations with 16 unknowns (calibration factors). The 16 unknowns are the elements of the 4x4 correction matrix. A software program optimized the solution and the calibration matrix was loaded into the DSP.

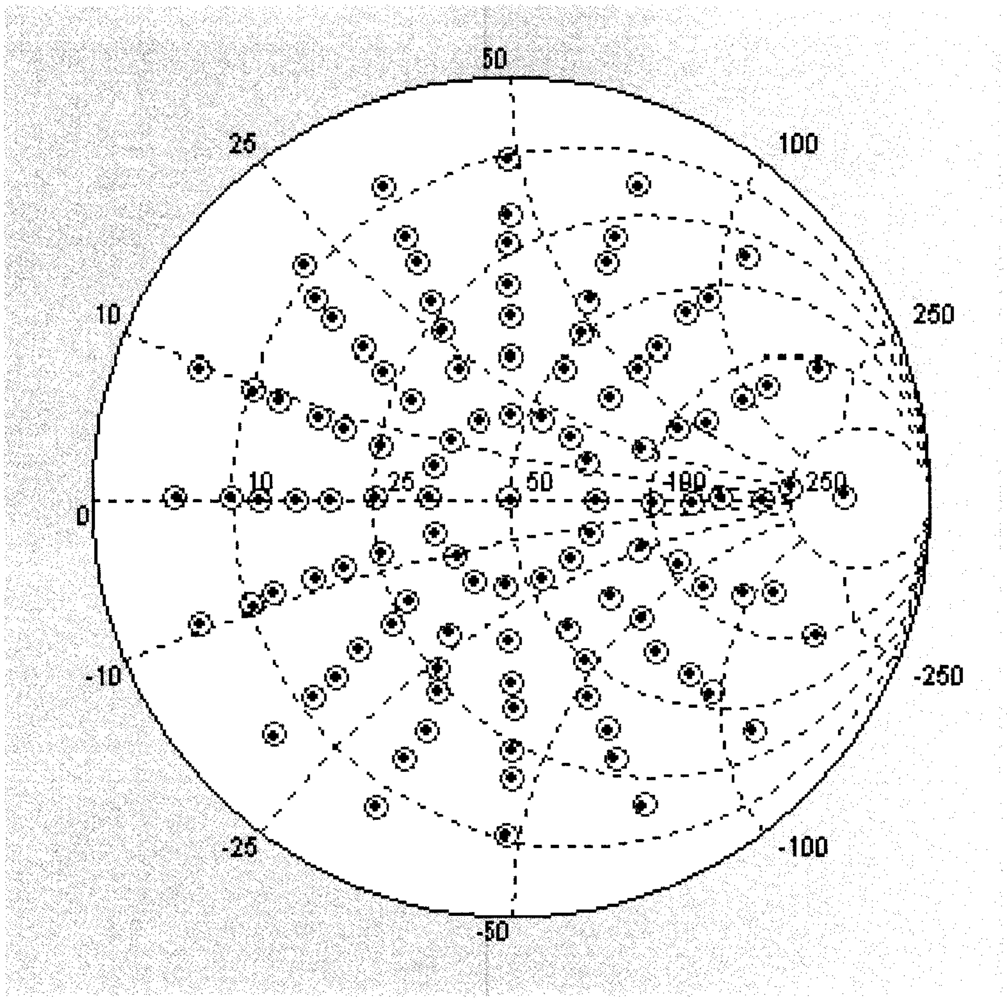

Fig. 5.12 Impedance Accuracy of the Circuit, After Calibration

The measurement process was repeated, this time with the calibration coefficients. The result of the direct digital impedance measurement, with the device calibrated, in graphical form is depicted in Fig. 5.12.

To verify the repeatability of the device, six devices were tested on a fixed load. Typical applications require specifications of accuracy into VSWR=3. A fixed load of $Z = 17.00 + j2.70$ was measured using six different devices.

Table 5.1 Test Results. Six Different Devices Measured a Fixed Load

DUT ID	Measured Resistance R	Measured Reactance X	Impedance distance (W)	Impedance Error (%)	Phase (rad)	Phase Error (rad)	Phase Error (deg)
552750	16.87	1.2	1.51	0.09	0.07	-0.09	-4.96
552753	16.78	2.2	0.55	0.03	0.13	-0.03	-1.55
552755	17.34	3.5	0.87	0.05	0.20	0.04	2.39
552756	16.65	2.2	0.61	0.04	0.13	-0.03	-1.50
552757	17.23	3.4	0.74	0.04	0.19	0.04	2.14
552751	17.45	2.3	0.60	0.03	0.13	-0.03	-1.52

The test results were very good (see Table 5.1). The Impedance error was below 0.1%.

The next step was to verify the power accuracy. The setup from Fig. 5.13 was used to evaluate the power accuracy. To minimize the errors the variable match was removed from the circuit during the 50Ω power accuracy test.

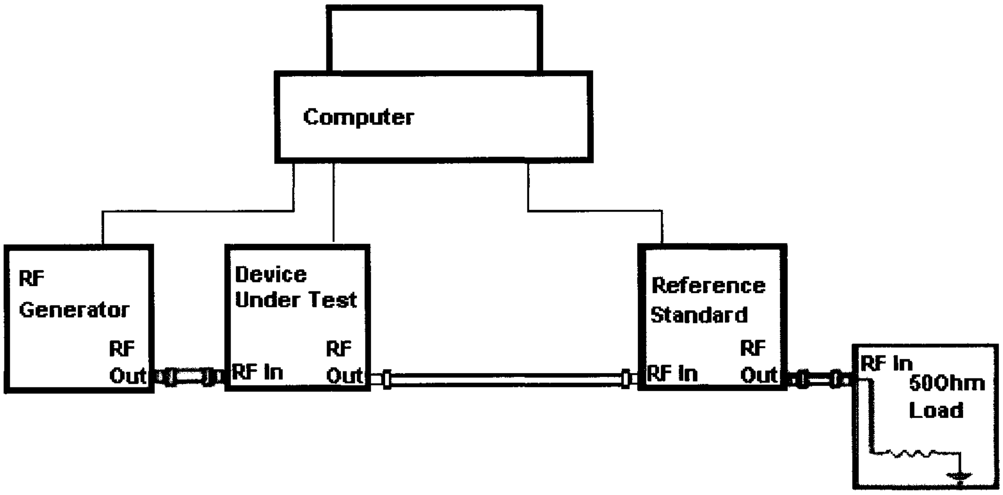

Fig. 5.13 Power Accuracy of the Circuit, Setup for 50Ω Test

The power accuracy test results are listed in Table. 5.2. Power was increased in 10 steps from 32W to 2500W. The reference standard was a transfer standard calibrated on the calorimeter. A proper way to characterize the RF power accuracy is by using a combination of percentile and absolute values. The result of my tests was 0.34% accuracy or 0.71W whichever is higher (Table 5.2).

Table 5.2 Power Accuracy of the Circuit into 50Ω. Test Results

RF Power level (W)	DUT (W)	Standard (W)	Error	UM
32	31.37	32.08	-0.71	W
50	49.56	50.07	-0.51	W
100	99.92	99.95	-0.03	W
200	199.67	199.91	-0.24	W
400	399.48	399.88	-0.10	%
800	798.82	800.34	-0.19	%
1000	997.71	1000.98	-0.33	%
1500	1499.47	1501.36	-0.13	%
2000	1999.83	2001.34	-0.08	%
2500	2501.55	2500.45	0.04	%
3000	2984.4	2994.45	-0.34	%

Looking at the results we can notice that all the errors are in the negative range. If we perform a correlation between the DUT and the Standard reference

(Fig. 5.14) we can conclude that is not an offset error but a slope error (error of 0.16%). In the ideal case, the correlation function was supposed to be y=x, but we obtained y=1.0016x. The explanation of the slope error is from the variable match. The efficiency of the variable match had an error of 0.16% into 50Ω.

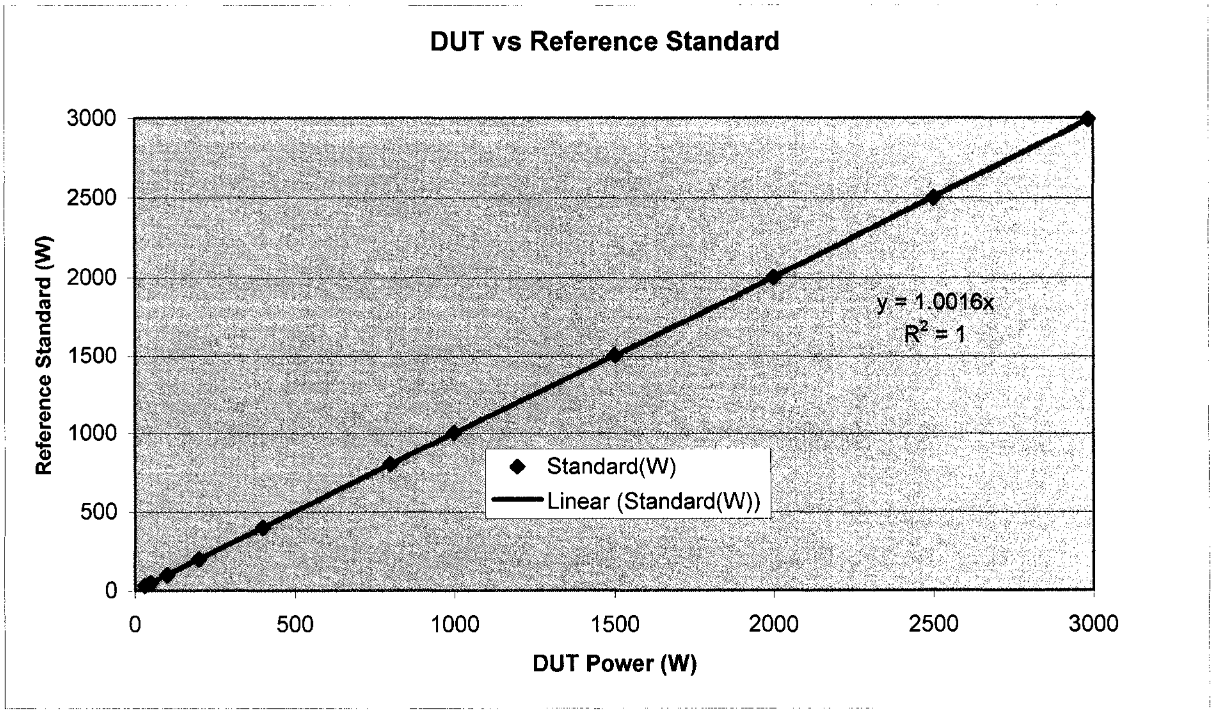

Fig. 5.14 **Correlation revealed a slope error of 0.16%**

To evaluate the repeatability and reproducibility of the measurement method a Measurement System Analysis[27] was performed. The subjects of the test were 6 devices connected as shown in Fig. 5.13. Three different operators performed three tests for a total of 54 tests. Table 5.3 contains the input data (error into 50Ω at 1000W) for the MSA.

Table 5.3 Power Error at 1000W into 50Ω Load

MSA Data Template

Date: 8/3/2006
Part Type: Direct Sampling Measurement

USL: 1.0
LSL: -1.0

		Operator 1			Operator 2			Operator 3		
Part #	Reference	Rep 1	Rep 2	Rep 3	Rep 1	Rep 2	Rep 3	Rep 1	Rep 2	Rep 3
1	0	0.218	0.247	0.135	0.145	0.055	0.201	0.04	0.145	0.134
2	0	-0.042	-0.102	-0.112	-0.122	-0.145	-0.045	-0.002	-0.114	-0.156
3	0	-0.011	-0.004	0.065	-0.087	-0.102	0.02	0.04	-0.098	-0.109
4	0	-0.02	0.101	0.155	0.125	0.056	0.09	0.089	0.002	-0.04
5	0	-0.224	-0.058	-0.124	-0.187	-0.114	-0.209	-0.108	-0.098	-0.188
6	0	-0.269	-0.282	-0.212	-0.225	-0.305	-0.321	-0.231	-0.187	-0.165

Test results were slightly skewed by -0.05 (Mean=-0.05 in Fig. 5.15).

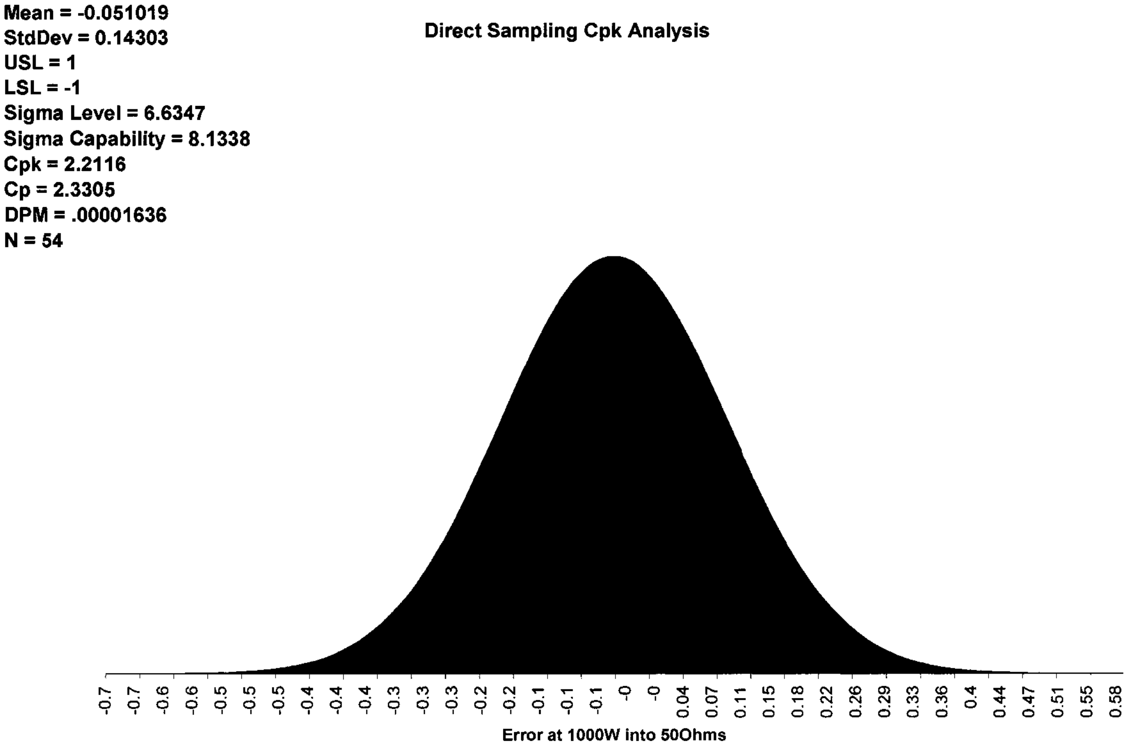

Mean = -0.051019
StdDev = 0.14303
USL = 1
LSL = -1
Sigma Level = 6.6347
Sigma Capability = 8.1338
Cpk = 2.2116
Cp = 2.3305
DPM = .00001636
N = 54

Fig. 5.15 Cpk Analysis Results on Power Error at 1000W into 50Ω Load

The mean value drives the same conclusion as before: the match efficiency requires a slight correction. I used +1% as Upper Level and –1% as Lower Level. With a result of σ=6.6 this measurement device is more than adequate to measure 1% accuracy.

Table 5.4 Measurement System Analysis of power error at 1000W into 50Ω load

MSA ANOVA Method Results

Source	Variance	Standard Deviation	% Contribution
Total Measurement (Gage)	0.00383208	0.061903798	16.33%
Repeatability	0.00368531	0.060706794	15.70%
Reproducibility	0.00014677	0.012114678	0.63%
Operator	0.0001389	0.011785637	0.59%
Oper * Part Interaction	7.8642E-06	0.002804318	0.03%
Product (Part-to-Part)	0.01963497	0.140124847	83.67%
Total	0.02346705	0.153189598	100.00%

USL	1
LSL	-1
Precision to Tolerance Ratio	0.18571139
Precision to Total Ratio	0.40409923

Repeatability[28] (Table 5.4) is a figure of merit for the interaction of the device under test with the test operator. Repeatability is 15.70%, 5 times less than the product repeatability. This means that no matter how the operator handled the device, the error introduced is 5 times less than the error introduced by the inaccuracy of the device. Reproducibility (figure of merit of the variance between operators) is below 1%, which is a very good result.

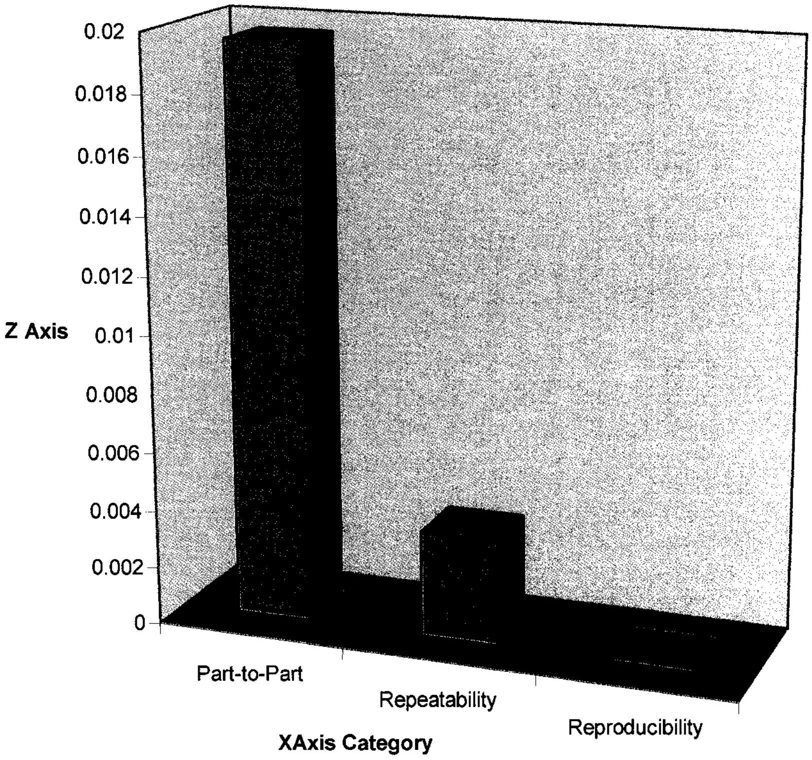

Fig. 5.16 Power at 1000W - Measurement System Variance Components

Another way of looking at the errors is depicted in Fig. 5.16. Out of the entire measurement system, errors less then 20% are due to the operator (reproducibility) and operator/device interaction (repeatability). The study concludes that the device is easy to use and gives repeatable and reproducible results.

5.4 Conclusions

The direct digital sampling method is well known as a generic way of acquiring signals. My unique contribution is to supplement the direct sampling method with the math behind the signal processing analysis that delivers information regarding both the amplitude and phase between two input signals. Also, I contributed to the development of the calibration method.

A new method to measure RF impedance and RF power into real and complex loads was presented from both the theoretical and the practical point of view. Direct digital RF sampling front end uses no analog frequency down conversion mixing. This type of design significantly simplifies the multiple frequency receiver design. In theory the accuracy should be almost zero, but digital errors combined with variable match calibration and power reference will have an effect on the final result.

Errors of less than 0.3% were obtained consistently for power measurements into 50Ω and lower than 0.1% error readings for impedances.

5.5 References

[1] Sonderman, T., Bode, C. and Miller, M., Advanced Process Control Technology Evolution Requirements for 300-mm Manufacturing, AEC/APC XV Symp., (September 13-17, 2003).

[2] S. Djurovic, Diagnostic Measurements in RF Plasmas for Materials Processing, 157, Atomic processes in plasmas, Portland, ME, (1991).

[3] Koenig, H. R., Maissel, L. I., Application of RF Discharges to Sputtering,168-171, (Mar. 1970).

[4] A Broadband Short-pulse Plasma Diagnostic Technique for Measuring Electroacoustic Resonances, Proceedings of IEEE, vol. 60, Baird, 754-755, (Jun. 1972).

[5] Brouk, V., and Heckman, R., Stabilizing RF Generator and Plasma Interactions, AEC/APC XVI Symp., (September 18-23, 2004).

[6] Sobolewski, M., Real-Time, Non-Evasive Monitoring of Ion Current and Ion Kinetic Energy During Plasma Etching and Deposition," AEC/APC XVII Symp., (Sept. 26-28, 2005).

[7] Gordon, W.B., A comparison of three direct sampling techniques, Record of the IEEE 1995 International Radar Conference, 546 – 550, (8-11 May 1995).

[8] Xiaobing, Sun, Zheng, Bao, Analysis and experimental results of digital quadrature coherent detector, CIE International Conference of Radar. Proceedings, 381 – 384, (8-10 Oct 1996).

[9] Hua, Liu Jian, Yuan, Zhou Xi, Spectrum arrangement and the generalized bandpass signal directsampling theorem, 3rd International Conference on Signal Processing, Volume: 1, 28-31, (14-18 Oct 1996).

[10] Davies, N.C., A high performance HF software radio, Eighth International Conference on HF Radio Systems and Techniques, IEE Conf. Publ. No. 474, 249 – 256, (2000).

[11] Biebl, E.M., Sampling architectures [radio receivers], Microwave Symposium Digest, 2003 IEEE MTT-S International, Volume: 2, 1055- 1058, (8-13 June 2003).

[12] Doerner, S., Schneider, T., Schroder, J., Hauptmann, P., Universal impedance spectrum analyzer for sensor applications, Proceedings of IEEE Sensors, 2003. Volume 1, 596 – 599, (22-24 Oct. 2003).

[13] Yanpu, Chen, Jieqiu, Zhang, Dabin, Li, Ronggui, Cheng, Triangular window weighted algorithm for RMS value measurement, Signal Processing, 2004, Proceedings. ICSP apos;04. 2004 7th International Conference on Volume 1, 85 – 88, (31 Aug.-4 Sept. 2004).

[14] J. R. Roberts, J. K. Olthoff, M. A. Sobolewski, R. J. Van Brunt, J. R. Whetstone, Bracewell, R., The Fourier Transform and Its Applications, 3rd ed., New York: McGraw-Hill, (1999).

[15] Walker, J. S., Fast Fourier Transform, 2nd ed., Boca Raton, FL: CRC Press, (1996).

[16] Brigham, E. O., The Fast Fourier Transform and Applications, Englewood Cliffs, NJ: Prentice Hall, (1988).

[17] Elliot, F. D. and Rao R. K., Fast Transforms, Algorithms, Analyses, Applications, Academic Press, (1982).

[18] Papoulis, A., The Fourier Integral and its Applications, New York: McGraw-Hill, (1962).

[19] Stoer, J. and Bulirsch, R., Introduction to Numerical Analysis, New York: Springer-Verlag, 1980. Academic Press, New York, (1982).

[20] Blahut, R. E., Fast Algorithms for Digital Signal Processing, New York: Addison-Wesley, (1984).

[21] Cooley, J. W. and Tukey, O. W., An Algorithm for the Machine Calculation of Complex Fourier Series, Mathematics of Computation, Vol19, No90, 297-301, (1965).

[22] Gergkand, G. D., A Guided Tour of the Fast Fourier Transform, IEEE Spectrum 6, 41-52, (July, 1969).

[23] Lipson, J. D., Elements of Algebra and Algebraic Computing, Reading, MA: Addison-Wesley, (1981).

[24] Oppenheimer, A.V. and Shaffer, R.W., Digital Signal Processing, Prentice-Hall, Englewood Cliffs, NJ, (1975).

[25] Elliot, D.F. and Rao, K.R., Fast Fourier Transforms: Algorithms, (1982).

[26] Duhamel, P. and Vetterli, M., Fast Fourier Transforms: A Tutorial Review, Signal Processing 19, 259-299, (1990).

[27] Kiemele, M. J., Schmidt, S. R., and Berdine, R. J., Basic Statistics: Tools for continuous Improvement, (1997).

[28] Schmidt, S. R., Kiemele, M. J., and Berdine, R. J., Knowledge Based Management, Air Academy Press & Associates, (1999).

CHAPTER 6

CALIBRATION TECHNIQUES FOR RF POWER MEASUREMENT DEVICES

6.1 Background

The calibration of RF devices can be achieved only using indirect RF to DC power measurement methods[1-5]. Moreover, the final accuracy of the calibrated device will be affected by the cumulative errors of all the instruments or references used in the chain of measurement. At best, the RF instrument calibration will only be as good as the secondary reference that was used. All RF high power instruments are calibrated (besides other procedures) into 50Ω loads.

For accurate and traceable RF power measurements, the principle of RF/DC power substitution[6-9] is used for primary standards because no RF standard exists. By comparing the heating effects of the RF power and a substituted DC power in the energy-absorbing element of a calibrating calorimeter, the RF power level is traced back to a DC power standard (DC Voltage and DC Current). In a practical calorimeter, various corrections are usually necessary as described below.

One ideal RF calibration possibility would be to look at the line voltage[10] of the fundamental frequency. This approach would work well, but only if the load is perfectly matched to the RF generator (adapted) and the signal would also have zero harmonics (perfectly sinusoidal). When the load is not matched to the source there are forward and reflected standing waves along the transmission medium, connecting the source and the load (see Fig. 6.1). The only constant along the unmatched transmission line is the delivered power.

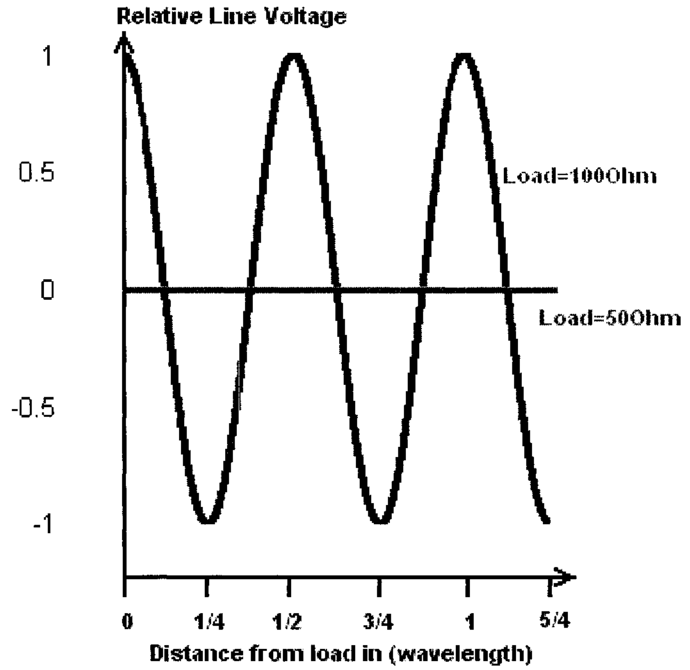

Fig. 6.1 Voltage Across a Transmission Medium Depends on the Load

Even accurately measuring the amplitude of an RF voltage is no trivial matter. A typical RF oscilloscope has +/-5% error for voltage amplitude readings. RF voltage amplitude calibration has also a traceability issue; there is no such thing as an absolute RF standard for RF voltage. Hence we are forced to measure the energy delivered by an RF source to the load.

The RF energy delivery calibration process does have a sound traceability part, but it is affected by many cumulative errors. The sources of the calibration errors using calorimetry are going to be studied in this chapter.

Any traceable energy standard substitution method takes hours to perform an accurate RF calibration. For this reason it is considered impractical to directly calibrate each RF instrument. The typical approach is to calibrate a secondary reference that later is used to calibrate the RF instruments. The secondary reference source is called a "transfer standard". Calibration of the RF Instrument versus the transfer standard is done by direct comparison.

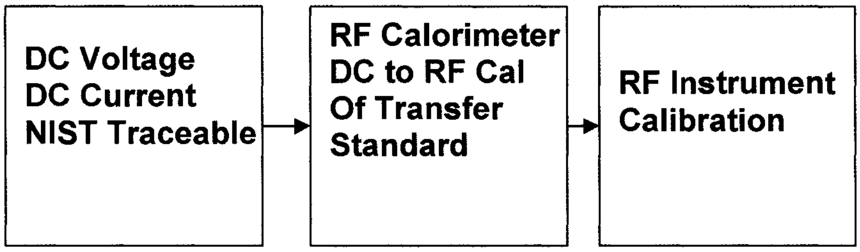

Fig. 6.2 RF Instrument Calibration. Calorimetry Pathway

There are several methods commonly used to calibrate the Transfer Standard. Two of them are presented in detail in this chapter along with an associated error analysis.

6.2 RF Calibration Method by a Dry Calorimeter

The dry calorimeter is most associated with a bolometric measurement, method[11-13] widely used by National Laboratories to calibrate RF signals at mW levels and microwave frequencies[14-24].

I will describe a method that would leverage the fundamental work done so far in the field of low power RF calorimetry and then extend it to high power calibrations, in the range of kW.

The first method is based on a calibrated directional coupler (or a series of cascaded directional couplers) along with a calibrated secondary RF power reference. An RF generator will deliver power to the input of a directional coupler connected to two separate loads. The ratio of the power split, K, between port 2 and port 3 is known as a characteristic of the directional coupler. In Fig. 6.3, one of the power meters is calibrated (either the) it is a matter of algebraic calculation to find exactly how much RF power is flowing to the other port.

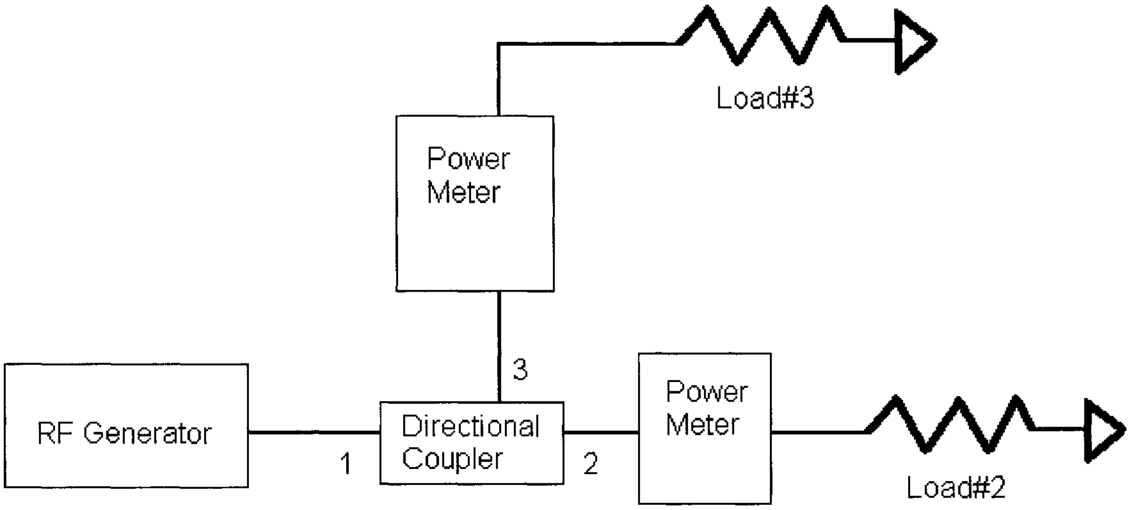

Fig. 6.3 Dry Calorimeter – Block Diagram

The dry calibration method relies primarily on two known elements:

a) A calibrated Power reference connected to Load#3 in Fig. 6.3

b) A directional coupler with a calibrated power coupling coefficient, K

$$K = \frac{P_2}{P_3} \tag{6.1}$$

The coupling coefficient *K* is not easy to characterize. The transfer factor *K* is affected not only by the intrinsic characteristics of the coupler, but also by the external loads. Since we are dealing with high power RF (kW range), a simple network analyzer characterization is not enough due to thermal effects. Thermal drift of the directional coupler will affect the accuracy. Therefore it is important to maintain the directional coupler at constant temperatures. Using alumina or (even better) beryllium oxide for the directional coupler substrate will help spread the heat and maintain a constant coupler temperature during calibration. We can use several couplers and form a scaling chain between an available standard and an unknown RF power level.

If we have a 1kW RF transfer standard available (calibrated using a substitution method) and we try to calibrate a 10W RF standard then the directional coupler will require 20dB-coupling factor. The same 20dB coupler would be used if we have a 10W transfer standard and we have to calibrate a 1kW RF standard.

$$K = 10 * \log\left(\frac{P_3}{P_2}\right) \quad (6.2)$$

6.2.1 Dry Calorimeter. Error Analysis

The quantitative analysis of the errors introduced by external load or source factors is done using the RF scatter S parameters[25-28].

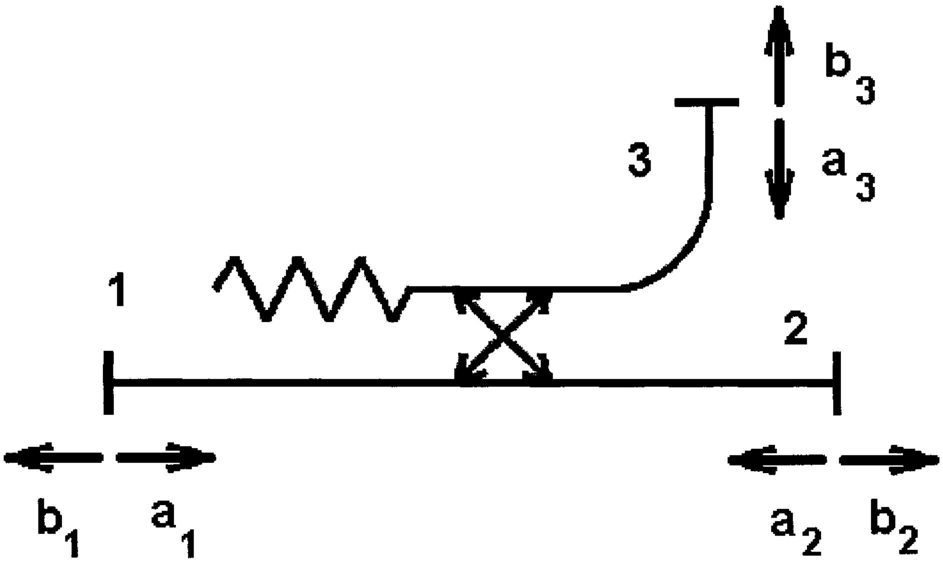

Fig. 6.4 Directional Coupler Scatter Diagram

The scattering equations for the directional coupler junctions (Fig. 6.4) are given, by definition, in terms of the S parameters as follows:

$$\begin{cases} b_1 = S_{11}a_1 + S_{12}a_2 + S_{13}a_3 \\ b_2 = S_{21}a_1 + S_{22}a_2 + S_{23}a_3 \\ b_3 = S_{31}a_1 + S_{32}a_2 + S_{33}a_3 \end{cases} \tag{6.3}$$

Consider the case where we are interested to develop an expression for b_3 (output power) in terms of b_2 (input power). The relation would give us the power transfer coefficient. Solving equation 6.3 for b2 in terms of b3 we find:

$$b_2 = \frac{S_{21}}{S_{31}} b_3 + \left(S_{22} - \frac{S_{21}S_{32}}{S_{31}} \right) a_2 + \left(S_{23} - \frac{S_{21}S_{33}}{S_{31}} \right) a_3 \tag{6.4}$$

The RF measurement setup will include loads attached to port 2 and to port 3. Ideally the loads would be adapted (exactly 50Ω impedance matched) but in reality they have associated reflection coefficients Γ_2, respectively Γ_3:

$$\begin{cases} a_2 = \Gamma_2 b_2 \\ a_3 = \Gamma_3 b_3 \end{cases} \tag{6.5}$$

Making the substitutions we get the final expression equation 6.6 for b_2 in terms of S parameters, b_3, Γ_3 and Γ_2:

$$b_2 = \frac{\frac{S_{21}}{S_{31}} + \Gamma_3\left(S_{23} - \frac{S_{21}S_{33}}{S_{31}}\right)}{1 - \Gamma_2\left(S_{22} - \frac{S_{21}S_{32}}{S_{31}}\right)} b_3 \tag{6.6}$$

Assuming the wave amplitudes are normalized by the characteristic impedance, the incident power P_2 on the load connected to port 2, is given by:

$$P_2 = |b_2|^2 \tag{6.7}$$

By squaring the amplitude (from expression 6.6) we get:

$$P_2 = \left(\frac{\frac{S_{21}}{S_{31}} + \Gamma_3\left(S_{23} - \frac{S_{21}S_{33}}{S_{31}}\right)}{1 - \Gamma_2\left(S_{22} - \frac{S_{21}S_{32}}{S_{31}}\right)}\right)^2 |b_3|^2 \tag{6.8}$$

On port 3 we have also connected a power sensor. Similarly, $|b_3|^2$ is the incident power on port 3.

The power transfer coefficient K from port 2 to port 3 is:

$$K = \frac{|b_2|^2}{|b_3|^2} \tag{6.9}$$

Substituting expression 6.8 in equation 6.9 we obtain the final expression for the power ratio factor from port 2 to port 3 as in Fig.6.4.

$$K = \left(\frac{\frac{S_{21}}{S_{31}} + \Gamma_3 \left(S_{23} - \frac{S_{21}S_{33}}{S_{31}} \right)}{1 - \Gamma_2 \left(S_{22} - \frac{S_{21}S_{32}}{S_{31}} \right)} \right)^2 \tag{6.10}$$

All scatter parameters can be measured with a network analyzer[29-37] and an accurate transfer factor *K* can be computed. Γ_2, respectively Γ_3 are intrinsic characteristics of the loads 2 and 3 and they can also be measured using a network analyzer.

6.3 RF Calibration Method by a Wet Calorimeter

Wet calorimeter calibration method applies to real impedance lines (50Ω) and high RF power (>100W to kW). The principle of a wet calorimeter is based on the substitution method of one calibrated source of energy being compared to an unknown source of energy. Specifically, a temperature increase in a common load developed by a standard DC source is compared with the temperature change (in the same load) developed by an RF source that is under test. If the temperature change in the load by the RF generator and the DC source are the same we conclude that the power levels are equal to the DC power level. This is an indirect method that relies on the wide availability of DC equipment (traceability of DC voltages and DC currents standards).

The RF load that is used for this application is water-cooled ("wet") and has a frequency bandwidth that starts from DC. RF and DC sources are alternatively cycled to the load until a thermodynamic equilibrium is met (Fig. 6.5).

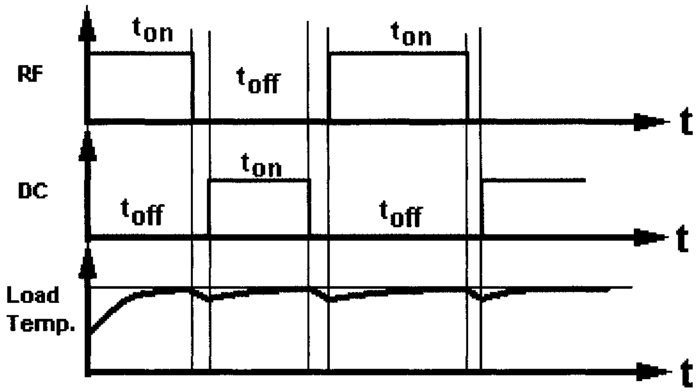

Fig. 6.5 Wet RF Calorimeter Timing Diagram to Compare DC and RF Energy Delivery

6.3.1 Wet RF Calorimeter Components and Analysis of Possible Error Sources

Some of the RF Calorimeter components are large error sources and their control is critical for an accurate calibration. Other components have a reduced error contribution (<0.1%), but their control will also help reduce the overall error of the calibration process.

6.3.1.1 Load Impedance Effect on Calorimeter Accuracy

A major RF calibration error is introduced by the fact that the load is not pure resistive, but also has a reactive component. Off the shelf resistive RF loads have 5% Z accuracy; the manufacturer does not specify if this is a resistive R or reactive X error. Experimental measurements show that the error can be of any nature (resistive or reactive); furthermore the error is changing in time.

$$\tan\varphi = \frac{X}{R} \tag{6.11}$$

Only load delivered RF power P_{DLV} will heat up the load while the RF measurement systems are measuring forward power P_{FWD} and reflected power P_{RFL}.

$$P_{DLV} = P_{FWD} - P_{RFL} \tag{6.12}$$

Delivered DC Power is:

$$P_{DC} = V_{DC} I_{DC} \tag{6.13}$$

As a figure of merit, I arbitrarily define the error introduced by the Imaginary part (X) of the load as the difference between the forward RF Power and the delivered Power. Ideally the RF reflected Power would be 0W and the forward and delivered Power would be equal.

$$E_{Load} = \frac{P_{FWD} - P_{DLV}}{P_{FWD}} * 100(\%) \tag{6.14}$$

In expression 6.14 we substitute the relation 6.15 between forward power P_{FWD} and delivered power P_{DLV}. The RF reflection coefficient is defined as:

$$\Gamma = \frac{Z_l - Z_0}{Z_l + Z_0} = \sqrt{\frac{P_{RFL}}{P_{FWD}}} \quad (6.15)$$

$$E_{Load} = \frac{P_{FWD} - P_{FWD}(1 - |\Gamma|^2)}{P_{FWD}} * 100(\%) \quad (6.16)$$

Performing the simplification we obtain the error introduced by the mismatch of the load as a function of load reflection coefficient:

$$E_{Load} = |\Gamma|^2 * 100(\%) \quad (6.17)$$

Now I define the *LoadDeviation* as the difference from the actual mismatch load Z_l to the nominal value $Z_0 = 50 + j0$

$$LoadDeviation = \frac{\sqrt{(R_l - 50)^2 + X_l^2}}{50} * 100(\%) \quad (6.18)$$

In summary, a *LoadDeviation* of 6.5% will introduce a calorimeter error of 0.1%. Fig. 6.6 summarizes the calibration of forward power versus load deviation. Hence, for a 1% error accuracy in RF calibration the load deviation has to be 22%. However, for high accuracy (<0.1%) the load deviation must be accounted for.

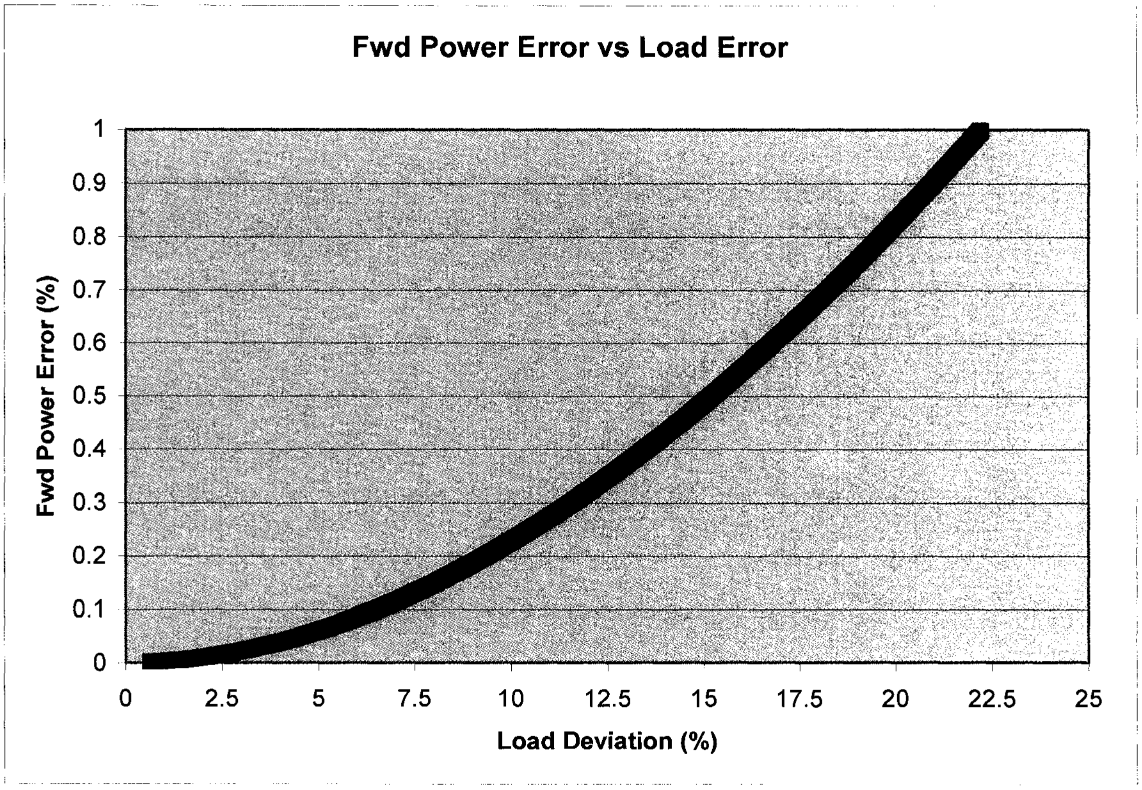

Fig. 6.6 RF FWD Power Error vs. Load Error

Since typical off the shelf RF loads are only 5% accurate they will introduce an error of 0.06% for the Forward Power reading.

6.3.1.2 Effect of the Coolant Flow Variations on Calorimeter Accuracy

The calorimeter employs the measurement of the temperature rise of water flowing thru a heated load. Variations of the cooling water flow[38] in a calorimeter can introduce calibration errors. Below I will derive an expression for the dependency of the measured power dissipated in a load immersed in water versus the flow variations.

I can express dissipated power P versus energy Q and time t.

$$P = \frac{Q}{t} \tag{6.19}$$

The energy Q also depends on the cooling mass m and temperature increase ΔT of the coolant as it passes through the calorimeter:

$$Q = mc\Delta T \tag{6.20}$$

The cooling flow F (liters/second) depends on both: volume V and time t.

$$F = \frac{V}{t} \tag{6.21}$$

Density is the relation between mass and volume.

$$\rho = \frac{m}{V} \tag{6.22}$$

Combining all of the above expressions we obtain a relation for the dissipated power in the calorimeter versus water flow, cooling medium and temperature increase:

$$P = \frac{mc\Delta T}{t} = \frac{\rho V c\Delta T}{\frac{V}{F}} \tag{6.23}$$

$$P = F\rho c\Delta T \tag{6.24}$$

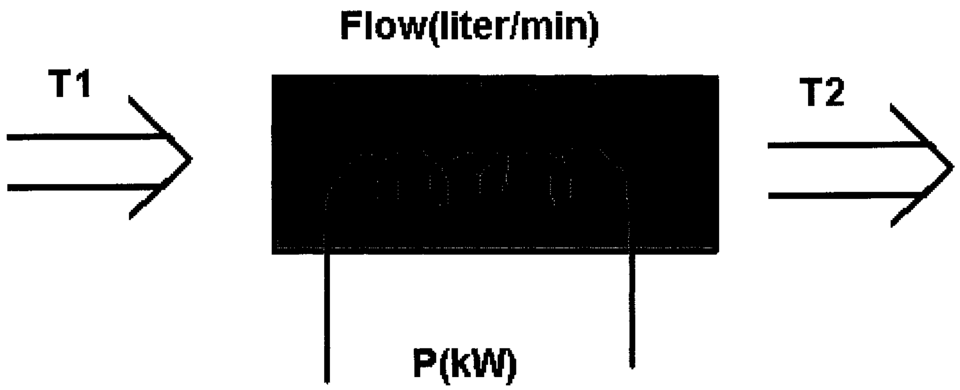

Fig. 6.7 Wet RF Calorimeter Energy Diagram

The increase in temperature ΔT for flowing water passing thru the heated load is:

$$\Delta T = \frac{P(W)}{F(\frac{liters}{\sec}) * 1000(\frac{kg}{m^3}) * 4.184 * 10^3 (\frac{J}{KgC})} \tag{6.25}$$

$$\Delta T = \frac{P(W)}{F(\frac{liter}{\min}) * 69.73} \tag{6.26}$$

$$P(W) = \Delta T * F(\frac{liter}{\min}) * 69.73 \tag{6.27}$$

Any unaccounted variations in water flow rate will directly affect the calorimeter accuracy via ΔT measured.

This requires a very accurate and constant flow pump - constant flow. Further considerations and more exact calculations can be done based on the flow type (laminar or turbulent), shape and surface of the material, but the above assumptions are sufficient for first order error calculations.

The error on the calorimeter accuracy is one to one. 1% change in water flow will determine a 1% inaccuracy of the power measurement.

6.3.1.3 Effect on Calorimeter Accuracy due to Input Temperature Variations of the Coolant

A typical coolant used for RF calorimetry is water or water based solution. As has been shown above, the temperature variation induced by the applied power is inverse proportional to the product of density ρ and caloric capacity of the coolant C_p. Below I show that for every °C difference of inlet water we get a 0.04% error in calorimeter power calibration. Water temperature variations will introduce a power measurement error if the absolute input temperature, T1 in Fig.6.7 (going into the load), will change during RF measurement cycle vs. DC measurement cycle. In other words it is not enough to match the increase in temperature during DC and RF cycle, but one must also match the inlet temperature (or introduce a correction factor) to do an accurate calibration.

Variations in the inlet water temperature, T1 in Fig.6.7, are inducing fine changes in both the density and specific heat of water[38, 39]. The product of the water heat capacity and water density affects the energy transfer from the heated element to the water. Both these elements are temperature dependent.

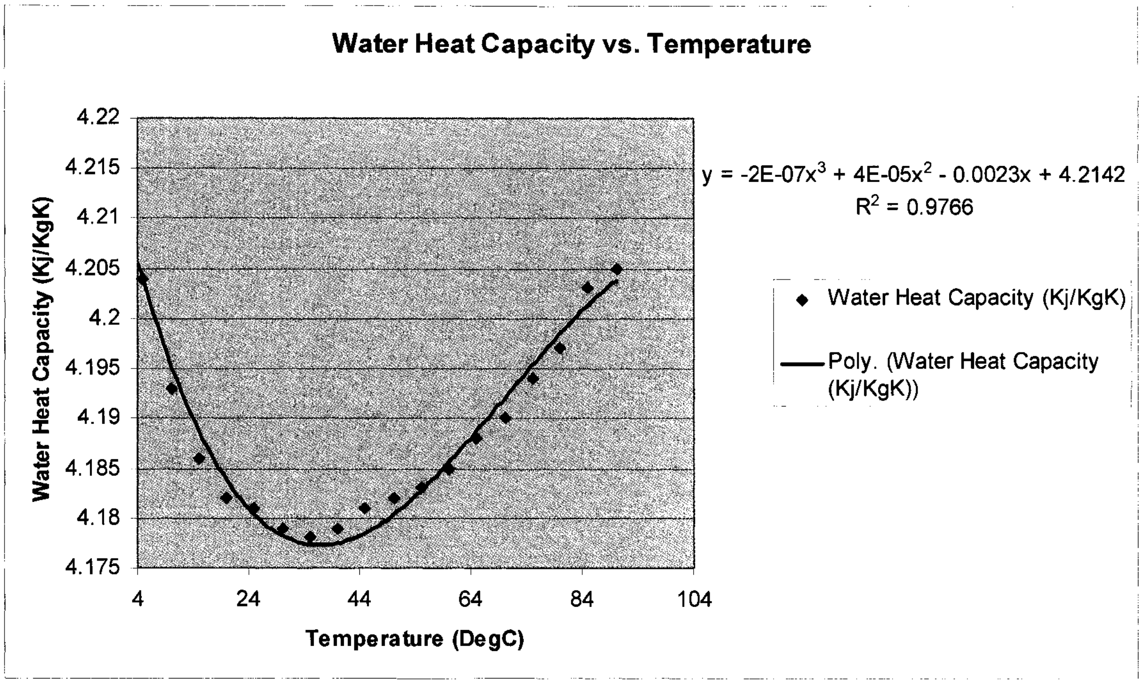

Fig. 6.8 **Specific Heat Capacity for Water vs. Temperature**

Observe that Water Heat capacity has a minimum around 35°C.

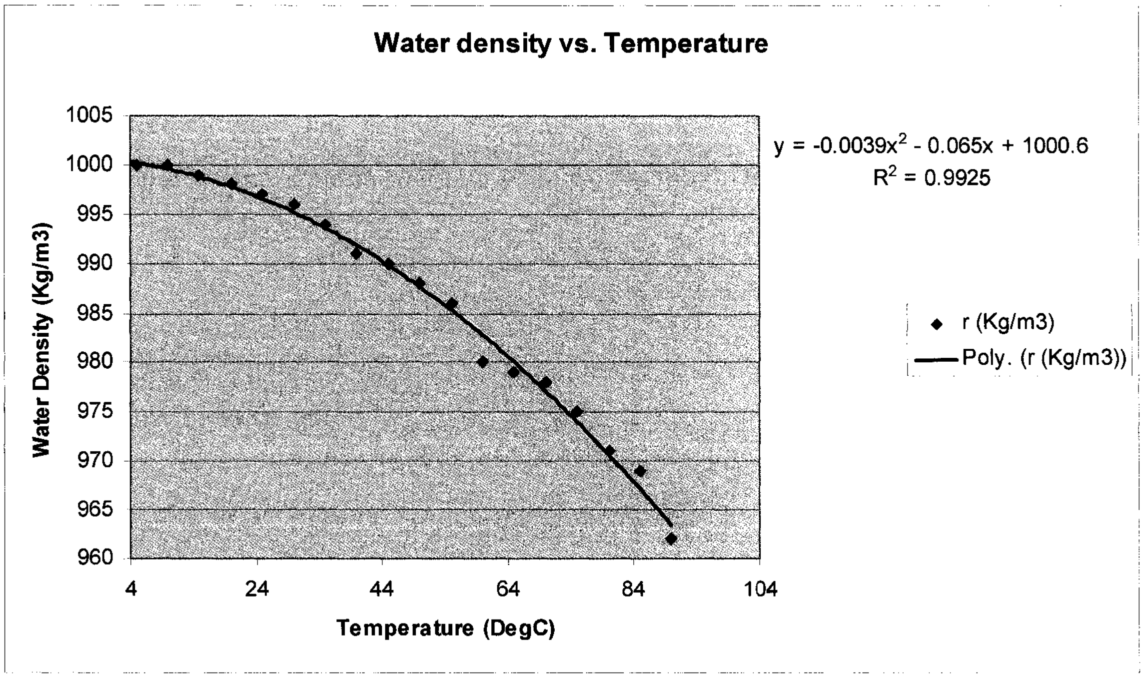

Fig. 6.9 **Specific Water Density vs. Temperature**

For temperatures above 25 °C we can model the water density as a linear function.

$$\rho = 1 - \frac{0.04}{200}(T - 4) \tag{6.28}$$

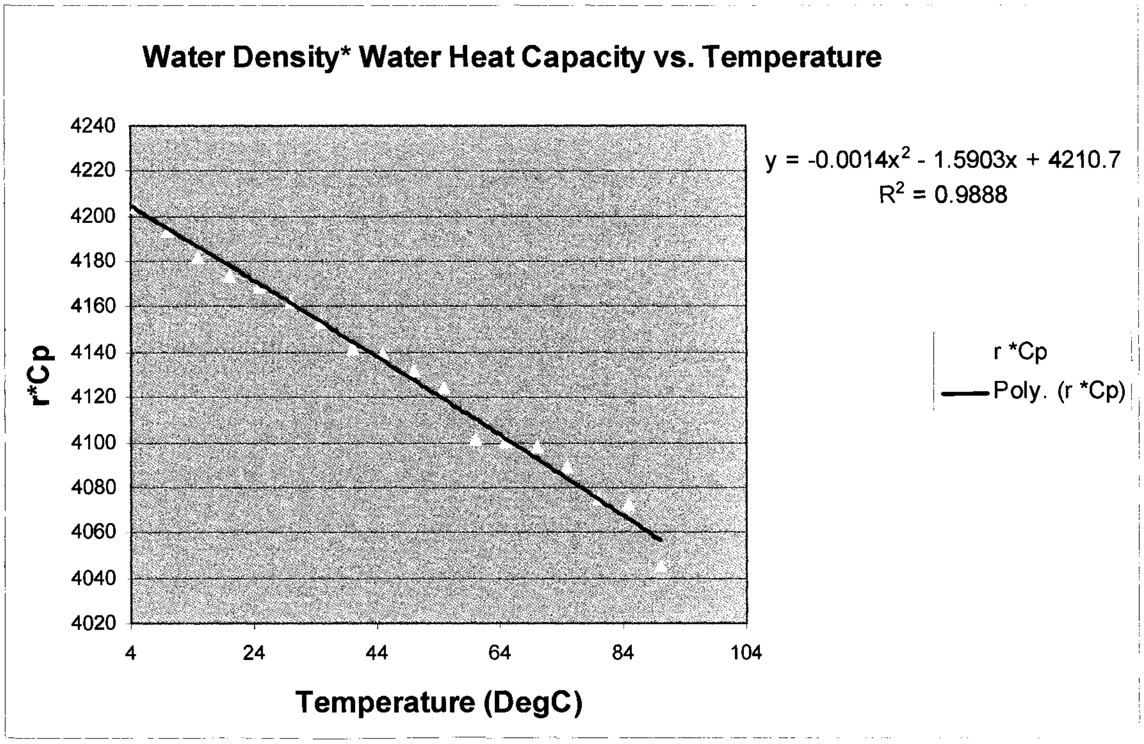

Fig. 6.10 The Product Water Heat Capacity*Water Density vs. Temperature

Therefore, as demonstrated above, the error introduced by the cooling agent (water) depends on the variation of the inlet temperature in the calorimeter. Cooling water temperature will affect the heat transfer. The RF test should be performed at the same inlet temperature as the DC test or the power should be corrected according to the variations presented in the above graph.

The calorimeter error due to inlet water changes in temperature is given by the following function:

$$P_{Errorwatertemp\,\mathrm{var}\,iation} = \frac{y(T+1) - y(T)}{y(T)} * 100(\%) \qquad (6.29)$$

y(T) function is the interpolation of the product Water Heat Capacity*Water Density vs. Temperature as illustrated in Fig 6.10.

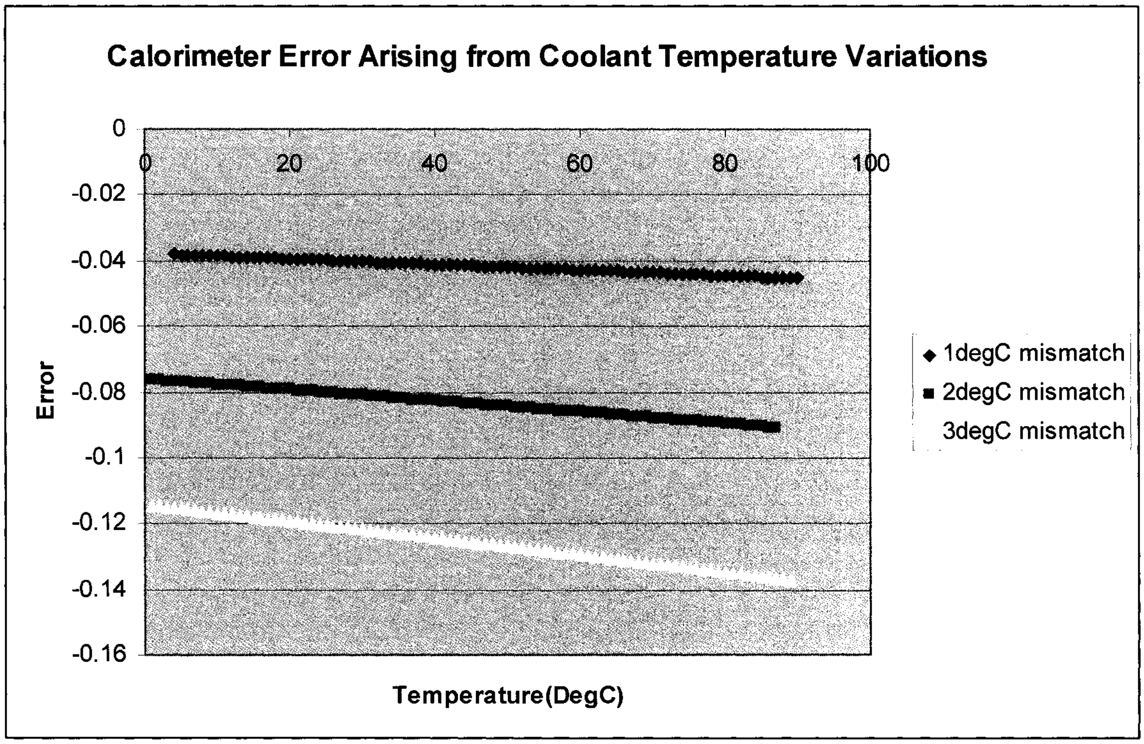

Fig. 6.10 Calorimeter Error due to Water Inlet Temperature Variation from DC to RF Cycle

An error calculation for the calorimeter power calibration gives an error of -0.04%/°C for the water inlet temperature variations from DC to RF cycle.

6.3.1.4 The RF/DC Switch Effect on the Calorimeter Accuracy

The switch used to connect either the DC supply or the RF generator to the load should be dimensioned according to the maximum power and highest frequency that will be calibrated. However, any switch will introduce a loss and associated measurement errors sources can be quantified.

It is recommended to measure the DC voltage exactly at the load. This will eliminate all the errors related to cable length (losses on cables) and switch contact resistance.

Usually DC meters have difficulty when RF signal is applied so the practical solution would be to disconnect the DC measurement system while applying the RF. Typically the switch will be an RF switch.

When the calorimeter it is used to calibrate RF transfer standards there are no additional errors introduced by the switch (the RF standard should be connected next to the RF load; there is no switch between the transfer standard and the load).

If the calorimeter is used to calibrate/check RF generators we must take into consideration the switch loss and it should be introduced as a RF Power correction error. Careful consideration should also be given to the degradation in time of the switch loss. To minimize the loss degradation (and extend the life of the switch) it is recommended to do a “cold switch”- no DC ON or RF ON during the switch time.

6.3.1.5 RF/DC Cables Losses Effect on the Calorimeter Accuracy

To minimize the errors introduced by the cables connections from the source to the load it is recommended to perform the DC voltage measurement right on the terminals of the load. DC current can be measured anywhere in the circuit.

RF cable losses can and will introduce a measurable loss if we are calibrating an RF source. One must introduce a proper RF power correction according to the cable loss. Every manufacturer provides a diagram containing the cable loss versus frequency.

No cable loss error is introduced if we calibrate an RF standard and if it is connected next to the load.

6.3.1.6 Temperature Measurement Error Effect on the Calorimeter Accuracy

Reliable temperature measurement is a major source of error involved in the accuracy of the calorimeter. We showed that:

$$P(W) = \Delta T * F(\frac{liter}{\min}) * 69.73 \tag{6.30}$$

For $\Delta T = 5°C$ measurement, an error of 0.1°C in this measurement is equivalent to a calorimeter RF power error of 2%.

Measuring the absolute temperature (even relative temperature) with 0.01% accuracy can be difficult. For this reason we employ an indirect solution to measure the temperature. Using Pt_{100} resistors or termistors, biased by a constant current supply, will convert the temperature measurement to a voltage measurement – that can be accurately done with better then 0,01% accuracy. More important is to match the temperature swing (relative change in temperature) during DC and RF cycles then to match the absolute water inlet temperature to the load. As it was demonstrated above, an inlet water temperature error of 1°C will generate 0.04% RF power error calibration while an error as small as only 0.1°C in the relative temperature swing will determine a 2% RF power error calibration.

If the inlet coolant temperature changes from the DC run to the RF run knowing the temperature difference is important in order to correct the power due to the change in heat transfer.

6.3.1.7 Effect of V_{DC} and I_{DC} Measurement Error in the Calorimeter Accuracy

The entire calorimeter indirect heat comparison philosophy (and traceability) of equal effects of power RF and DC heating on a load relies on the accuracy of the DC current and voltage measurements.

Off the shelf DC meters can easily measure DC voltage with better than 0.001% accuracy. The DC current can be measured by using an accurate shunt and a DC meter.

Fig. 6.11 4 Wire Current Measurement diagram

Evaluating the shunt value is critical and it should be done using a 4 wire method (2 wires for High power and 2 for instrumentation measurement). Self-heating of the shunt can change the readings. For RF power levels of calibration up to 3000W, as performed in my experiments, we require a current sensor of nominal 8A; however, due to self heating, a sensor of 50A would be more appropriate.

Since DC power is direct proportional to the current, an error of 1% in current reading would generate a 1% error in calorimeter power calibration.

6.3.1.8 RF Source Effect on Calorimeter Accuracy

An RF source is required if the calorimeter is used for calibrating transfer standards. One error source is the harmonic content in the output of the RF generator. Some RF standards are sensible to harmonics (a typical example is the diode detector topology); other RF standard topologies, for example containing a filter input or a heterodyne block, would further attenuate the effect of harmonics.

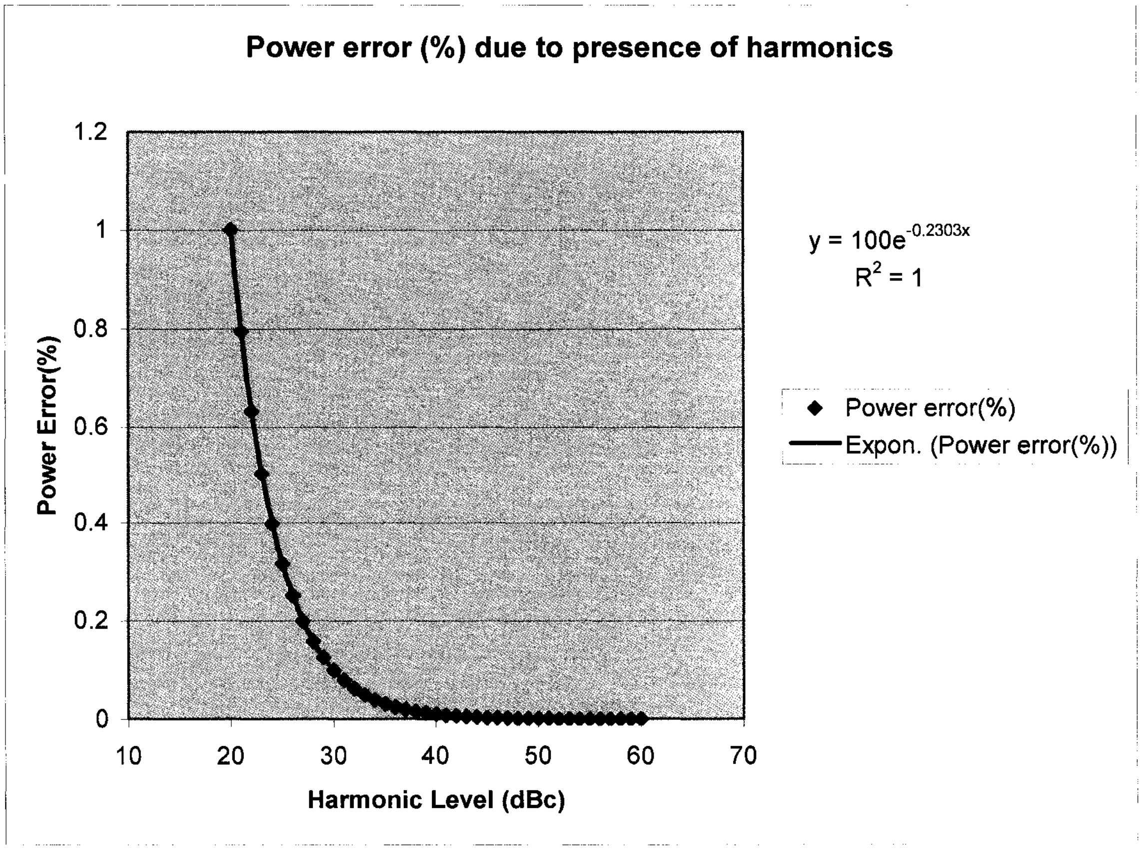

Fig. 6.12 Calorimeter Power Error vs. RF harmonics

For less than 0.01% calibration error a less than 40dB level of harmonic content is required for the RF generator.

6.3.1.9 DC Source Effect on Calorimeter Accuracy

The RF calorimeter requires a variable high power DC source with low ripple. A linear power supply is ideal, but the typical solution is a switching power supply, because they are cost and space effective. The downside to the use of a switching power supply is the output “noise”. Supplementary output filtering of the DC power supply is highly recommended.

In summary, table 6.1 contains a condensed list of errors for the wet calorimeter.

Table 6.1 Wet Calorimeter Error Sources

Reference	Error Source	Error Detail	Error Magnitude (%)	Note
6.3.1.1	Heating element / RF load	Reactive component of the RF load	0.1% for 6.5% load error	-
6.3.1.2	Water flow variations	Cooling pump RPM variations	Direct proportional 0.1% for 0.1%	Constant flow is critical to the calorimeter
6.3.1.3	Inlet water temperature variations	Inlet cooling mixer	0.04%/°C	-
6.3.1.4	RF/DC Switch loss	Switch insertion loss	0%	The error is topology dependent.
6.3.1.5	RF/DC cables	RF cable loss	0%	-
6.3.1.6	Temperature measurement	Instrument accuracy	Error of 0.1°C is equivalent to a calorimeter error of 2%.	The most important error source.
6.3.1.7	V_{DC} and I_{DC} measurement system	Instrument accuracy	0%	The current sensor must be properly characterized
6.3.1.8	RF Source	Harmonics	0.01% for 40dB harmonics level	The RF source should have less than 40dB harmonics content
6.3.1.9	DC Source	DC Output ripple	0%	A good output filter is required.

In my experience the most important error source is the temperature measurement system. Even if there are other elements that can change the accuracy, I consider this one to be the primordial error source. The second source of error is the current measurement block; a current sensor is difficult to characterize with 0.01% accuracy; in addition thermal effects, if any, are also difficult to quantify.

6.4 Mathematical Basis for the Complex Impedance RF Calibration

We can achieve a more accurate measurement calibration if we employ more than one reference to perform the calibration and if the absolute errors of these different references are randomly distributed (rather than using only one reference). Statistically speaking, the best achievable error would be affected by the distribution of the errors. If the error distribution of the references is random then (theoretically) a zero error can be achieved.

To follow this approach I used more than one reference to calibrate an RF measurement device and all the references had a random distribution of the absolute error. More accurate stochastically based calibration results were reported also by Rolain and team[40].

For a linear system the mathematical calibration process for error correction can be reduced to a calculation of a set of correction values A_k that will satisfy the equation:

$$Y_k = X * A_k \tag{6.31}$$

We assume that the system under calibration is stable and responds every time with a set of signals defined by the matrix X.

The calibration matrix A_k will transform the behavior of the device X to be near to reference Y_k (Fig. 6.13), with an error e_k. Y_k is a matrix characteristic of the reference identified by indices k.

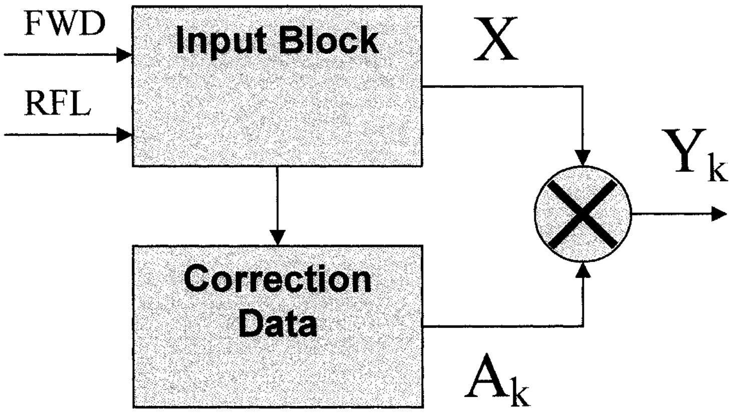

Fig. 6.13 Generic Signal Processing During Calibration

If we have n references and every reference is defined by a set of properties (vector Y_k) then we can define *Y* space as expression 6.33.

$$Y = \{Y_1, Y_2, Y_3 .....Y_n\} \tag{6.32}$$

By default every reference has an error e_k versus the standard Y (ideal value). It is common practice to use references Y_k that were traceable to a standard Y.

$$Y_k = \mathrm{Y} + e_k \tag{6.33}$$

The purpose of the calibration process is to determine the correction data (content of matrix A_k).

$$A_k = X^{-1}Y_k \tag{6.34}$$

We consider e_k a random variable with a normal distribution. Module of e_k has a maximum value ε. The assumption is generally true for electrical/mechanical references. By definition a reference tends to emulate a standard but it has a degree of uncertainty that is modeled here as an error e_k.

$$|e_k| \le \varepsilon \tag{6.35}$$

The calibration process will link the space or references *Y* to the space of calibration values *A*.

$$Y_k \xrightarrow{Calibration} A_k \tag{6.36}$$

$$A = \{A_1, A_2, A_3 .....A_n\} \tag{6.37}$$

Use of the average $\overline{Y}$ of multiple references will lead to the expression 6.38 for the calibration matrix A_i; A_i can be a member of the calibration values (space *A*).

$$A_i = YX^{-1} \tag{6.38}$$

6.38 is the expression of $\overline{Y}$ that takes into consideration the errors e_k.

$$\begin{aligned} \overline{Y} &= \frac{\sum_{k=1}^{n} Y_k}{n} = \frac{\sum_{k=1}^{n} (\mathrm{Y} + e_k)}{n} = \frac{n\mathrm{Y} + \sum_{k=1}^{n} e_k}{n} \\ \overline{Y} &= \mathrm{Y} + \frac{\sum_{k=1}^{n} e_k}{n} \end{aligned} \tag{6.39}$$

If the reference error is random, has a normal distribution and the number of references is infinite then the sum of errors will be zero.

$$\lim_{k \to \infty} \sum_{k=1}^{n} e_k = 0 \tag{6.40}$$

If the sum of errors is zero then the average of the references $\overline{Y}$ is equal to the standard Y.

$$\overline{Y} = \mathrm{Y} \tag{6.41}$$

Using the average of multiple references $\overline{Y}$ to calculate the calibration set A_i will determine our calibrated system to deliver characteristics similar to the standard Y.

$$\mathrm{Y} = X * A_i \tag{6.42}$$

The measurement system in Fig. 6.14 must be calibrated to report correct (with low error) for both power and impedance. We are using as reference an RF Match and a 50Ω line W-meter. The combination of references (RF Match and W-meter) will give us complete information about the level of power and impedance at the output of the RF generator. The RF Match is characterized by a random error therefore the entire system of reference is affected by a random error.

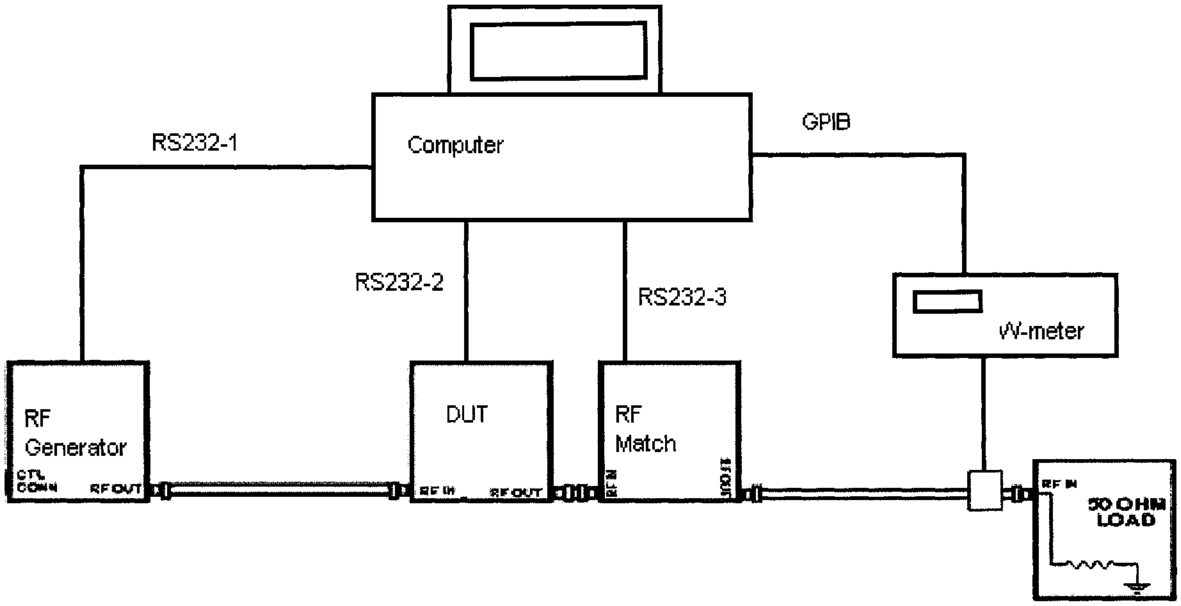

Fig. 6.14 Example of RF Power and Impedance Calibration Setup for Complex Impedance Lines

Assuming that the Device Under Test (DUT) reports four independent electrical signals, the X matrix has 4 elements and based on that we can calculate Forward, Reflected Power and impedance. Therefore the sufficient calibration matrix A_i would have 4x4 elements. Depending on the application (symmetry) the Calibration Matrix A_i can be reduced to less than x^2 elements.

To find the 16 elements of matrix A_i we need to produce a set of 16 equations. The equations can be generated by changing the state of the system (i.e. changing the settings of the RF match) and reading the reported values from the measurement system (what we want to calibrate) and from the reference (RF Match and W-meter). We change the settings (position) of the RF match 16 times and read the outputs X from the DUT and from the W-meter.

Because of inaccuracies of both the references and of the readings the equations would not have an exact solution (matrix X), but rather can be found only as a best approximation. To increase accuracy of the calibration, I recommend changing the state of the system in more than x^2 instances. This will produce a large set of equations with x^2 unknowns. The solution of the system with more then x^2 equations cannot be uniquely found. In this case solving the equations is reduced to the best fit solutions; a set of solutions that satisfies the set of equations with minimum errors.

6.5 Summary and Conclusions

I presented three calibration methods; two of them for real impedance lines and one for real and complex impedance. All calibration methods presented in this dissertation involve correction factors that must be determined or empirically calculated. My approach is the calibration against multiple references that have a random distribution of errors. Statistical average of random errors should give (theoretically) a minimum error reference.

Also, on this chapter, I presented, for the first time, a complete error analysis on a wet high power calorimeter. My analysis improves both the accuracy on actual wet calorimeters and reduces calibration time.

All RF Power instruments will require a calibration into 50Ω line. Further calibration (into complex loads) is required if the instrument claims accuracy into complex loads.

None of the existing or presented methods are trivial. All of them require a great amount of time to be perfected. The universally accepted calibration process is relatively short for a dry calorimeter (minutes/hour) and extremely long (hours) for a wet calorimeter. For practical purposes an absolute transfer standard is calibrated against the calorimeter and then it is used to calibrate production RF standards. Because of this methodology the errors are accumulating. Depending on the final required accuracy one must choose the calibration process accordingly.

6.6 References

[1] Fantom, A. E., Development of MK III calorimetric RF power meter. (triple feedback version), NPL Rep. DES 34, (July, 1976).
[2] Vollmer, E., Ruhaak, J., Janik, D., Peinelt, W., Butz, W., Stumper, U., Microcalorimetric measurement of the effective efficiency of microwave power sensors comprising thermocouples, Conference on Precision Electromagnetic Measurements, Digest, 147-148, (July, 1994).
[3] Inoue, T., Yamamura, K., A broadband power meter calibration system in the frequency range from 10 MHz to 40 GHz using a coaxial calorimeter, IEEE Transactions on Instrumentation and Measurement, Volume 45, Issue 1, 146 – 152, (February, 1996).
[4] Kinard, J.R., Zhen, Z., De-Xiang Hang, Rebuldela, G., Janik, D., de Vreede, J., Intercomparison of thermal converters at NIM, NIST, PTB, SIRI, and VSL from 10 to 100 MHz, IEEE Transactions on Instrumentation and Measurement, Volume 42, Issue 2, 618 – 621, (April, 1993).
[5] Juroshek, J. R., NIST 0.05-50 GHz direct comparison power calibration system, Conference on Precision Electromagnetic Measurements, Digest, 166-167, (May, 2000).
[6] Filipski, P.S., van Mullem, C.J., Janik, D., Klonz, M., Kinard, J.R., Lipe, T.E., Waltrip, B.C., Comparison of high-frequency AC-DC voltage transfer standards at NRC, VSL, PTB, and NIST, IEEE Transactions on Instrumentation and Measurement, Volume 50, Issue 2, 349 – 352, (April, 2001).
[7] Van Mullem, C., Janssen, W. J. G. D., De Vreede, J. P. M., Evaluation of the

calculable high frequency AC-DC standard, IEEE Transactions on Instrumentation and Measurement, Volume 46, Issue 2, 361 – 364, (April, 1997).

[8] Klonz, M., Bergeest, R., Caizergues, A., Fraisse, D., Winther, C. A. D., Pogliano, U., Cabiati, F., Bosco, G. C., Zago, G., Dessens, J. T., de Vreede, J. P. M., Rydler, K.-E., Nilsson, H., BCR intercomparison of AC-DC current transfer standards, Conference on Precision Electromagnetic Measurements, Digest, 421-422, (June, 1994).

[9] Larsen, N. T., A New Self-Balancing DC-Substitution RF Power Meter, IEEE Trans. on Instrum. and Measurement, Vol. IM-25 (4), 343-347, (December, 1976).

[10] Gierke, H., Grno, L., Janik, D., Munter, K., Automatic RF voltage calibration with a primary voltage standard up to 1 GHz, IEEE Transactions on Instrumentation and Measurement, Volume 42, Issue 2, 519 – 523, (April, 1993).

[11] Ascroft, J. T., Developments in coaxial power standards at NPL, IEEE Transactions on Instrumentation and Measurement, Volume 48, Issue 2, 647 – 649, (April, 1999).

[12] Jurkus, A .P., Stumper, U., National standards and standard measurement systems for impedance and reflection coefficient, Proceedings of the IEEE, Volume 74, Issue 1, 39 – 45, (January 1986).

[13] Stumper, U, New developments of RF and microwave power standards, Conference on Precision Electromagnetic Measurements, Digest, 296-297, (July, 1998).

[14] Larsen, N. T., A new self-balancing de-substitution rf power meter, IEEE Trans. Instrum. Meas. IM-25: 343-347, (December, 1976).

[15] MacPhearson, A. C., Kerns, D. M., A microwave microcalorimeter, Rev. Science Instrum. 26(1): 27-33, (January, 1955).

[16] Engen, G. F., A refined x-band microwave microcalorimeter, J. Res. Nat. Bur. Stand. (U.S.) 63C(1), 77-82, (July-September, 1959).

[17] Harvey, M. E., WR 15 microwave calorimeter and bolometer unit, Nat. Bur. Stand. (U.S.) Tech. Note 618, (May, 1972).

[18] Weidman, M. P., Hudson, P. A., WR 1- millimeter wave microcalorimeter, Nat. Bur. Stand. (U.S.) Tech. Note 1044, (June, 1981).

[19] Clark, R. F, The microcalorimeter as a national microwave power standard, Proceedings of the IEEE Volume 74, Issue 1, 102 – 104, (January, 1986).

[20] NPL Measurement Services, http://www.npl.co.uk/measurement_services/
Estin, A. J., Juroshek, J. R., Marks, R. B., Clague, F. R., and Allen, J. W., Basic
[21] RF and Microwave Measurements: A Review of Selected Programs, Metrologia 29, 135-151 (1992).

[22] Engen, G. F., Microwave Circuit Theory and foundations of microwave metrology, Peter Peregriunus Ltd. on behalf of IEE, London (1992).

[23] Juroshek, J. R., A direct calibration method for measuring equivalent source mismatch, Microwave J., 106-118, (October, 1997).

[24] Weidman, M. P., Direct comparison transfer of microwave power sensor calibrations, NIST Tech. Note 1379, (1996).

[25] Michael L. Gabitass, Robert K. Froelich, and Don E. Peck Automated three-port S-parameter measurements, Microwave Journal Horizon House Publications, Inc., v33, n9,133, (September 1, 1990).

[26] S-parameter test station for production testing of multi-state microwave devices, Microwave Journal Horizon House Publications, Inc. v33, n6, 222, (Jun 1, 1990).

[27] Agilent Technologies, Agilent AN154 S-Parameter Design Application Note.

[28] Verspecht, J., McKinley, M., Remley, K. A., Schreurs, D., Williams, D., Linearizing Large-Signal Scattering Functions, IEEE Microwave Theory Tech., (April 01, 2005).

[29] Hewlett-Packard App. Note PN-8510-8, (Oct. 1987).

[30] Cronson, M. Harry, A Six-Port Automatic Network Analyzer, IEEE Transactions on Microwave Theory and Techniques vol. MTT-25, No. 12, (Dec. 1977).

[31] Hewlett-Packard Product Note 85610-13, Measuring Noninsertable Devices HP 8510-13 Network Analyzer, (Aug. 1, 1988).

[32] Ferrero, A. and Pisani, U., Two-Port Network Analyzer Calibration Using an Unknown Thru, IEEE Microwave and Guided Wave Letters, vol. 2, No. 12, (Dec. 1992).

[33] Adamian, V., Stable Source Aids Automated Noise-Parameter Measurements, The Time and Measurement Measurement Notebook, (Feb., 1988).

[34] Rytting, D., Advances in Microwave Error Correction Techniques, Hewlett-Packard, (Jun. 1, 1987).

[35] Curran, J., TRL Calibration for Non-Coaxial Measurements, Hewlett-Packard, (Dec. 1983).

[36] Hewlett-Packard, Network Analyzers, Test & Measurement Catalog, Oct. 1991, USA. .

[37] Hewlett-Packard Product Note 8510-5A, Specifying Calibration Standards for the HP 8510 Network Analyzer, (Feb. 1, 1988).

[38] Louis C. Burmeister, Convective Heat Transfer, 2nd edition, Wiley-Interscience, (1993).

[39] http://www.engineeringtoolbox.com/water-thermal-properties-d_162.html.

[40] Rolain, Y.; Van Moer, W.; DeGroot, D., A first step towards a wave-based "stochastic" calibration for multi-port vectorial network analyzers, ARFTG Conference Digest Spring, 2004. 63rd,151 – 156, (June 11, 2004).

CHAPTER 7

SUMMARY AND FUTURE WORK

7.1 Summary

Historically, prior efforts towards more accurate RF measurement systems were focused mostly on either more accurate components or better RF sensors. While knowing that better building blocks help, my research proved that both accuracy and repeatability of RF measurement could be better achieved by using digital correction to known sources of error rather than by pursuing perfect RF components.

The thesis research presents three RF measurement techniques: two for real impedance lines and one for real and complex line. All of them are delivering three times improved accuracy than previous methods when digital correction is employed. Hence my thesis indicates that the future high accuracy RF power measurements is toward less analog components and more digital functions.

7.2 Perspective on RF calibration

The lack of national or international high power RF calibration standards makes it difficult to compare results taken with different RF instruments. It is up to the RF instrument manufacturers to ensure that secondary RF references (standards) are correct and free of errors. The RF calibration process involves several steps in a chain of calibration events, every step having an error. Absolute accuracy of the RF measurement is a sum of errors, starting with the error of the calorimeter.

The limitations of the RF calorimeter arise from comparing heat effects of RF versus DC over the same load, to alternate between the two power sources. Besides accuracy limitations there are also limitations for the maximum RF power that can be calibrated on the calorimeter. The RF switch can perform the job to insert DC or RF generator into the circuit, but it has power and mechanical limitations. A better calorimeter topology that will increase the maximum RF power calibrated is presented in Fig. 7.1.

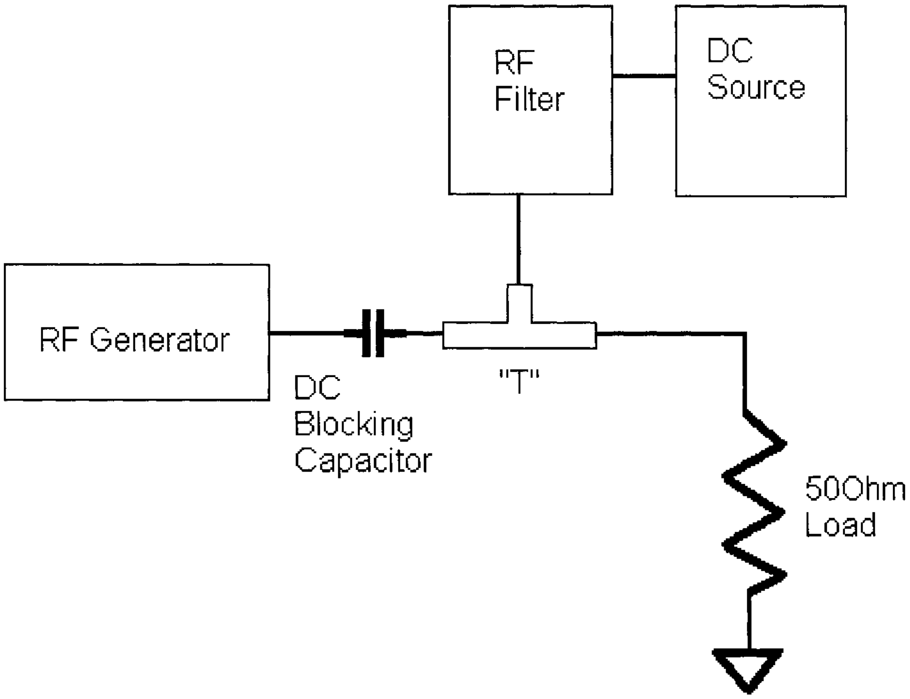

Fig. 7.1 Improved High Power RF Calorimeter Topology

There are still some impedance differences to be considered but the topology from Fig. 7.1 should not have any power limit, or the disadvantages of a mechanical switch.

A second direction to investigate, from this thesis, is the reduction in calibration time for a wet calorimeter. Better accuracy can be obtained if we can eliminate the transfer standards and calibrate the devices directly on the calorimeter. Instead of performing numerous comparison cycles between RF and DC thermal effects we can reach the calibration factors after only several cycles and estimate the errors based on the extrapolation of the thermodynamic basis of the calibration process.

7.2 Investigate Limitations on RF Power of the Proposed Techniques

Going to the extremes on high RF power or high RF frequency is challenging. There are always going to be measurement limitations due to components (lack of components or technology limitations) or laws of physics. It would be interesting to research the maximum dynamic range at RF that can be obtained while maintaining the accuracy below 1% from 3kW to 100kW and for frequencies above 100MHz.

ANNEX 1

Method of Determining the RF Power Losses in an RF Diport

To determine the match load efficiency, G, as the ratio of power output versus power input, one could use a calibrated Network Analyzer. The Network Analyzer has to be calibrated for measuring reflection coefficient at Port 1 and for measuring Transmission coefficient at Port 2. This technique requires measuring the S_{11} and S_{21} parameters.

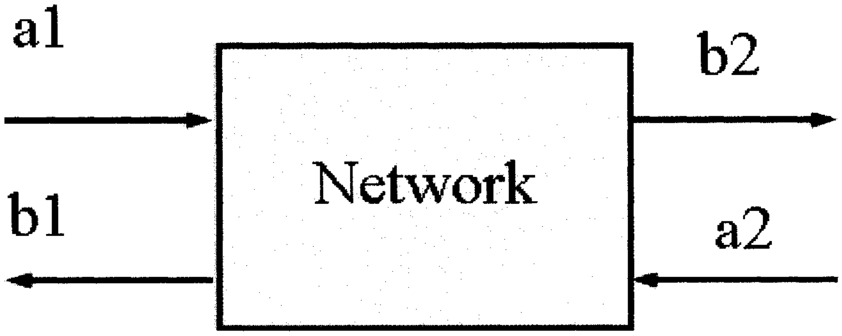

Fig. A.1 Generic Diport Network

Efficiency of a variable match is changing across the Smith Chart and should be mapped along with the impedance. Depending on the match design and the position on the Smith Chart the efficiency can vary significantly.

The easiest way to calculate the variable match would be to use the scatter parameters[A1] as follows:

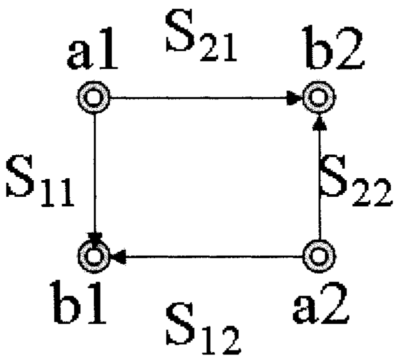

Fig. A.2 **Scatter Parameters for a Generic Diport**

By definition, S_{11} is the input reflection coefficient at port 1, calculated as the ratio between the output signal and input signal both at port 1 when the diport is terminated in the characteristic impedance at port 2:

$$S_{11}=\left.\frac{b_1}{a_1}\right|_{a_2=0} \tag{A.1}$$

By definition, S_{21} is the forward transmission calculated as the ratio between the output signal at port 2 and input signal at port 1 when the diport is terminated in the characteristic impedance at port 2:

$$S_{21}=\left.\frac{b_2}{a_1}\right|_{a_2=0} \tag{A.2}$$

By definition, S_{22} is the output reflection coefficient, at port 2 calculated as the ratio between the output signal and input signal both at port 2 when the diport is terminated in the characteristic impedance at port 1:

$$S_{22}=\frac{b_2}{a_2}\bigg|_{a1=0} \tag{A.3}$$

By definition, S_{12} is the reverse transmission, calculated as the ratio between the output signal at port 1 and input signal at port 2 when the diport is terminated in the characteristic impedance at port 1:

$$S_{12}=\frac{b_1}{a_2}\bigg|_{a1=0} \tag{A.4}$$

I define the efficiency of the match as the ratio between the Output Power, P_{out}, at port 2 and Input Power, P_{in}, at port 1:

$$G=\frac{P_{out}}{P_{in}} \tag{A.5}$$

$$G=\frac{|b_2|^2-|a_2|^2}{|a_1|^2-|b_1|^2}=\frac{\frac{|b_2|^2}{|a_1|^2}-\frac{|a_2|^2}{|a_1|^2}}{\frac{|a_1|^2}{|a_1|^2}-\frac{|b_1|^2}{|a_1|^2}}=\frac{|S_{21}|^2-\frac{|a_2|^2}{|a_1|^2}}{1-|S_{11}|^2} \tag{A.6}$$

$$G=\frac{|S_{21}|^2-\frac{|S_{11}|^2}{|S_{12}|^2}}{1-|S_{11}|^2} \tag{A.7}$$

$$G=\frac{|S_{21}|^2-\frac{|S_{21}|^2}{|S_{22}|^2}}{1-|S_{11}|^2} \tag{A.8}$$

If the load is adapted (50+j0 Ω) then $a_2=0$ (there is no reflected signal) and the formula A.8 becomes:

$$G=\frac{|S_{21}|^2}{1-|S_{11}|^2} \tag{A.9}$$

Typically the reflection and transmission coefficients are expressed in terms of dB (decibels). The conversion between dB and efficiency is expressed in A.10 formula.

$$G=\frac{10^{(S21indB/10)}}{1-10^{(S11indB/10)}} \tag{A.10}$$

A.1 References

[1] Agilent Technologies, Agilent AN154 S-Parameter Design Application Note.